Volcano-tectonic controls on magmatic evolution at Campi Flegrei, Italy: insights from thermodynamic modelling

Fay M. Amstutz[1*], Michael J. Stock[1], Victoria C. Smith[2], Roberto Isaia[3], Stefano Vitale[4], Elliot J. Carter[1,5], Jacopo Natale[6].

[1]Department of Geology, Trinity College Dublin, Dublin, D02 PN40, Ireland.

[2]School of Archaeology, University of Oxford, Oxford, OX1 3TG, UK.

[3]Istituto Nazionale di Geofisica e Vulcanologia, Osservatorio Vesuviano, 80124 Napoli, Italy.

[4]Dipartimento di Scienze della Terra, dell'Ambiente e delle Risorse (DiSTAR), Università di Napoli Federico II, 80126 Napoli, Italy.

[5]School of Geography, Geology and the Environment, Keele University, Staffordshire, ST5 5BG, UK.

[6]Dipartimento di Scienze della Terra e Geoambientali, Università degli Studi di Bari Aldo Moro, 70125 Bari, Italy.

*corresponding author, amstutzf@tcd.ie

ABSTRACT

Campi Flegrei caldera (Naples, southern Italy) is one of the most hazardous volcanoes on Earth, having produced >70 eruptions in the past 15 kyr, and currently showing significant signs of unrest within a densely populated part of Europe. Post-15 ka eruptions span a range of eruptive styles and compositions, which broadly correlate with the spatial and structural location of vents within the large caldera: eruptions from vents along northern and eastern caldera rim faults are typically small and extend to mafic compositions; eruptions from vents in the central and eastern side of the caldera extend to evolved compositions and have produced Plinian columns; and vents along regional faults (also activated by caldera collapse) in the western caldera have produced sub-Plinian eruptions which are often relatively Na_2O-rich and K_2O-depleted. These compositional and eruptive differences suggest an intrinsic link between their volcano-tectonic setting and structure and/or processes operating within the sub-volcanic magmatic system. To investigate this, we compare post-15 ka erupted glass major element compositions to liquid lines of descent produced using the Rhyolite-MELTS thermodynamic model. To constrain magma storage conditions at Campi Flegrei, we systematically vary the crystallisation conditions in 1800 models before employing a new statistical approach to assess the quality of fit between natural glass compositions and model outputs. In simple (uncontaminated) fractional crystallisation models, we find that glass compositions in each volcano-tectonic setting are best reproduced by similar storage conditions: pressure of 110–160 MPa, liquidus oxygen fugacity of 0–1 log unit above the quartz-fayalite-magnetite buffer, and a liquidus H_2O concentration of 2 wt% for northern, eastern and western caldera eruptions and 3 wt% for central caldera eruptions. However, the addition of an assimilant further improves the fit between predicted and observed major element compositions, with the amount and type of assimilant varying between volcano-tectonic settings. Best-fit models for vents along northern and eastern caldera rim faults include small (5–10%) amounts of Palaeozoic metamorphic

basement, whereas those for vents in the centre of the caldera or along the western regional faults include larger quantities (~30%) of assimilated syenitic restite. The Fondi di Baia eruption is compositionally anomalous, and its evolution may reflect minor limestone or hydrothermal calcite contamination. Our results demonstrate a novel link between the spatial and structural location of vents within the Campi Flegrei caldera and the physicochemical processes operating within its magmatic system, providing important information for the assessment of future hazard scenarios.

KEYWORDS

Assimilation; Campi Flegrei; fractional crystallisation; Rhyolite-MELTS modelling; volcano-tectonic control

INTRODUCTION

Caldera-forming volcanoes occur worldwide and are frequently associated with long-lived magmatic systems, which produce eruptions of varying size, style, and composition through time (Cole *et al.*, 2005). Following collapse, post-caldera eruptions typically occur in different spatial locations across the volcanic system, including along caldera ring faults and regional lineaments (Lipman, 1984); vent locations are often directly related to local volcano-tectonic structures, with magma ascent exploiting pre-existing planes of weakness (Robertson *et al.*, 2016; Németh *et al.*, 2017; Pérez-Orozco *et al.*, 2021). Compositional variations in erupted products are controlled by complex processes operating within the sub-volcanic crustal magma system, in addition to mantle heterogeneity (Pearce and Peate, 1995; Annen *et al.*, 2015), with the major element variations controlling magma rheology and chemical properties (e.g., viscosity and volatile solubility) which in turn impact the timing and style of eruptions (Cassidy *et al.*, 2018). However, the relationship between volcano-tectonic structures and sub-volcanic processes is poorly understood; it remains unclear whether structural controls can impact the

50 dynamics of magmatic systems and compositions of erupted melts. Addressing this has
51 important implications for hazard assessment and the interpretation of monitoring data where
52 unrest in different parts of a large active caldera system might reflect different crustal processes
53 and result in different volcanic eruption styles or compositions.

54 Campi Flegrei volcano (southern Italy) has produced >70 eruptions since the last major
55 caldera collapse at 15 ka (the Neapolitan Yellow Tuff [NYT] eruption; Smith et al., 2011). While
56 the primary mantle melts feeding these post-15 ka eruptions are thought to be relatively constant
57 with respect to the major element composition (Mazzeo *et al.,* 2014), the distribution of vents
58 is closely associated with regional structures (Peccerillo and Frezzotti, 2015; Peccerillo, 2017)
59 and subtle variations in erupted compositions have been identified across the caldera system
60 (D'Antonio *et al.*, 1999; Di Renzo *et al.*, 2011; Smith *et al.*, 2011). Hence, Campi Flegrei
61 presents an ideal location to explore whether the volcano-tectonic setting of an eruption impacts
62 processes operating within the sub-volcanic system. Additionally, the region around Campi
63 Flegrei is densely populated (~1.5 million people living within the caldera, and more than ~3.5
64 million likely to be immediately impacted by an eruption) and the system is currently showing
65 significant signs of unrest, making it one of the most hazardous volcanoes on Earth (Orsi *et al.*,
66 2004; Bevilacqua *et al.*, 2017). Constraining the magmatic processes which influence erupted
67 compositions in different parts of the caldera system has important implications for hazard
68 forecasting and the interpretation of volcano monitoring data.

69 Magma storage conditions can be determined in different volcanic environments using
70 a variety of petrological methods. These include: thermobarometry, using the pressure-
71 sensitivity of exchange reactions of chemical components between various mineral
72 assemblages (Putirka, 2008); comparisons between the chemistry of erupted products and those
73 from experiments conducted under controlled conditions (Blundy and Cashman, 2008); and
74 saturation depths calculated from the volatile contents of melt inclusions (Anderson *et al.*,

1989). The influence of assimilation on magmatic evolution can also be investigated, for example by comparison of the isotopic composition of the magma and potential crustal contaminants (James, 1981). Previous studies have attempted to link storage conditions to volcano-tectonic setting across a caldera system, for example Saxby et al. (2016) demonstrated a link between regional fault patterns and location of magma storage at Ilopango caldera (El Salvador) on the basis of gravity surveys, whereas Carracedo *et al.* (2007) noted compositional variation of eruptions in different locations across Tenerife (Canary Islands). However, these techniques generally only allow assessment of magma storage conditions over discrete ranges in the evolution of the sub-volcanic system (i.e. within the crystallisation interval of the phase used in barometry) and typically provide information on one intrinsic variable (such as pressure for barometry or extent of assimilation for isotope mixing models). In this study, we use thermodynamic modelling to assess the range of variables which control magma storage conditions through the entire liquid line of descent, finding combinations of variables which are consistent with erupted compositions.

The Rhyolite-MELTS thermodynamic modelling software calculates the stable phase assemblage in a magmatic system under given conditions, and can be applied to determine the evolving phase assemblage and phase compositions during fractional crystallisation (FC) or assimilation-fractional crystallisation (AFC, Gualda *et al.*, 2012; Ghiorso and Gualda, 2015). Through systematically varying model crystallisation conditions (i.e. pressure, oxygen fugacity, initial melt major or volatile element composition) and comparing with the abundance and composition of phases in natural erupted materials, previous studies have successfully used Rhyolite-MELTS (or its predecessor MELTS, which differs in the stability fields of quartz and sanidine, Ghiorso and Sack, 1995) outputs to constrain magma storage conditions in diverse volcanic systems (e.g. Peach Spring - Pamukcu *et al.*, 2015; Aluto - Gleeson *et al.*, 2017; individual Campi Flegrei eruptions - Fowler *et al.*, 2007; Fowler and Spera, 2010; Cannatelli,

100 2012). In general, these studies have identified the most probable set of magma storage
101 conditions by visually identifying the modelled liquid line of descent which best fits erupted
102 melt compositions. However, Gleeson *et al.* (2017) proposed a statistical method to quantify
103 the fit between natural and predicted compositions, more accurately identifying the best set of
104 model parameters where liquid lines of descent are similar or deviate from natural compositions
105 over a limited (~30°C) crystallisation interval.

106 Here, we use Rhyolite-MELTS to model isobaric FC and AFC of a near-primitive Campi
107 Flegrei liquid under different storage conditions, comparing the predicted phase assemblages
108 and liquid lines of descent with erupted products from vents in different volcano-tectonic
109 settings within the caldera. This extends previous work constraining magma storage for
110 individual Campi Flegrei eruptions using MELTS modelling (e.g. Campanian Ignimbrite -
111 Fowler *et al.*, 2007, Fowler and Spera, 2010; Minopoli 1 and Fondo Riccio - Cannatelli, 2012),
112 investigating eruptions in the last 15 kyr for which there is published glass major element
113 compositional data (n=48). By systematically varying the model pressure (P), liquidus fO_2
114 (L_{fO2}), liquidus H_2O content (L_{H2O}) and amount/type of assimilated material across the range of
115 potential parameter space, we are able to constrain the conditions and processes operating
116 during pre-eruptive magma storage, exploring the hypothesis that volcano-tectonic setting
117 impacts magmatic evolution. As different combinations of storage conditions can produce
118 model outputs which appear similar to a first order, we apply a novel statistical approach to
119 assess the correlation between modelled liquid lines of descent and measured glass major
120 element compositions. Our best-fit models (i.e. closest correlation between modelled liquid line
121 of descent and natural glasses) are for magma storage conditions which agree well with previous
122 estimates and show only minor variations between different volcano-tectonic settings.
123 However, we find that the addition of assimilants ubiquitously improves the model fit, but that
124 the type and amount of assimilant varies between eruptions from vents in different parts of the

Campi Flegrei caldera, indicating spatial variations in the nature of magma-country rock interaction.

GEOLOGICAL SETTING

Campi Flegrei is the largest centre in the Phlegraean Volcanic District, an area of volcanism in southern Italy (near Naples; Orsi *et al.*, 1996), formed as a result of back arc extension and the opening the Tyrrhenian Sea, related to rollback of the subducting Ionian plate (Faccenna *et al.*, 2007; Peccerillo and Frezzotti, 2015). Large-scale tectonic deformation in the Phlegraean area has given rise to two main regional fault systems, trending NE-SW and NW-SE (Acocella, 2010; Vitale and Isaia, 2014), which have influenced both the distribution of vents (Bevilacqua *et al.*, 2015) and orientation of Campi Flegrei caldera collapse scarps (Orsi *et al.*, 1996; Di Vito *et al.*, 1999; Vitale and Isaia, 2014; Natale *et al.*, 2022a).

The oldest volcanism at Campi Flegrei is dated to >300 ka (De Vivo *et al.*, 2001; Rolandi *et al.*, 2003; Di Vito *et al.*, 2008; Fernandez *et al.*, 2024), with the eruptive history punctuated by at least three major caldera collapse events: the ~40 ka Campanian Ignimbrite (CI, Giaccio *et al.*, 2017), the ~29 ka Masseira del Monte Tuff (Albert *et al.*, 2019) and the ~15 ka NYT (Deino *et al.*, 2004). These eruptions have produced a nested caldera structure (~13 km diameter), with collapse scarps juxtaposed against the regional tectonic lineaments (Vitale and Isaia, 2014; Natale *et al.*, 2022a). In the past 15 kyr, Campi Flegrei has produced >70 eruptions from vents located within the NYT caldera (Di Vito *et al.*, 1999; Smith *et al.*, 2011), coupled with ground deformation (Isaia *et al.*, 2019; Natale *et al.*, 2022b). These can be broadly divided into three epochs of intense activity (mean eruption frequency 50–70 yrs), separated by periods of quiescence (~1-3.6 ka; Di Vito *et al.*, 1999): Epoch 1 produced ~30 magmatic and phreatomagmatic eruptions between ~15 and 10.6 ka; Epoch 2 produced 8 low magnitude eruptions between ~9.6 and 9.1 ka; and Epoch 3 produced 28 eruptions between ~5.5 to 3.5 ka. These eruptions display a range in eruptive style and magnitude from effusive lava domes,

150 through small explosive events to the Plinian Agnano-Monte Spina eruption (Di Vito *et al.*,
151 1999; Smith *et al.*, 2011; de Vita *et al.*, 1999). The most recent Campi Flegrei eruption was at
152 Monte Nuovo in 1538 CE, which is post-Epoch 3 and considered separate due to the long repose
153 period between this event and the last eruption of Epoch 3 (>3 kyr, Piochi *et al.*, 2005; Smith
154 *et al.*, 2011).

155 Vent locations for post-15 ka eruptions span the NYT caldera (Fig.1) and can be broadly
156 divided into three distinct volcano-tectonic settings: 1) those along caldera rim faults in the
157 northern and eastern sectors of the caldera, which were either formed or reactivated during the
158 NYT collapse and strike obliquely to the regional lineaments ("northern/eastern caldera
159 eruptions"); 2) those in the west of the caldera aligned with caldera rim faults and regional
160 tectonic fault systems characterised by a different orientation pattern of faults and fractures
161 compared to those in the eastern sector ("western caldera eruptions"; Vitale and Isaia, 2014);
162 and 3) those within the central caldera which are not located along major pre-existing planes of
163 crustal weakness ("central caldera eruptions"; Fig.1: Di Vito *et al.*, 1999; Isaia *et al.*, 2009;
164 Bevilacqua *et al.*, 2015; Natale *et al.*, 2022b). Differences in the frequency and composition of
165 eruptions as well as structural differences in fault patterns between the east and west of the
166 caldera has led other authors to make similar divisions (Vilardo *et al.*, 2010; Vitale and Isaia,
167 2014; Bevilacqua *et al.*, 2016, 2017). In general, earlier eruptions were fed by magmas which
168 exploited the caldera rim faults (including regional fault systems reactivated during caldera
169 collapse), with later eruptions migrating towards the caldera interior (particularly in the
170 northeastern sector; Di Vito *et al.*, 1999; Isaia *et al.*, 2009) or regional tectonic faults in the
171 western caldera (Di Vito *et al.*, 1999; Vilardo *et al.*, 2010; Vitale and Isaia, 2014).

172 Throughout its history, Campi Flegrei has consistently produced alkali magmas
173 (Vineberg *et al.*, 2023), with melts of the post-15 ka eruptions ranging from shoshonite to
174 phonolite in composition (Smith *et al.*, 2011). Magmas do not form a continual compositional

trend between eruptive periods, but the most mafic shoshonitic products are from Epoch 1 with later eruptions extending to more evolved phonolite to trachyte compositions (Smith *et al.*, 2011). Several previous studies have noted a correlation between the volcano-tectonic setting of eruption vents and the composition of erupted products (D'Antonio *et al.*, 1999; Di Renzo *et al.*, 2011; Smith *et al.*, 2011). In general, northern/eastern caldera eruptions are the most primitive, occurring from NYT caldera rim faults (Civetta *et al.*, 1991) with more evolved Epoch 2 and Epoch 3 eruptions from the north-eastern caldera floor, and their products are indistinguishable on the basis of major element chemistry (Smith *et al.*, 2011). Eruptions from vents in the west of the caldera have been noted as the most compositionally diverse; for example, the Baia-Fondi di Baia deposits are highly evolved with distinct trace element concentrations relative to other post-15 ka eruptions (Smith *et al.*, 2011; Voloschina *et al.*, 2018).

Previous studies generally agree on the architecture of the Campi Flegrei sub-volcanic system being characterised by a main magma storage zone at ~7–8 km depth, with shallow (possibly ephemeral) sills at around 3–4 km depth (e.g. Stock et al., 2018; Petrelli *et al.*, 2023). Seismic tomography and magnetotelluric investigations have imaged a main region of magma storage at ~7.5 km (Zollo *et al.*, 2008; Bianco *et al.*, 2022; Isaia *et al.,* 2025) and small shallow reservoirs between 2–4 km (De Siena *et al.*, 2010; Calò and Tramelli, 2018; Giacomuzzi *et al.*, 2024). This agrees with pressures obtained from the volatile contents of melt inclusions, which give saturation depths of ~2 to ~9 km for multiple eruptions in the last 15 kyr (Mangiacapra *et al.*, 2008; Arienzo *et al.*, 2010, 2016; Vetere *et al.*, 2011; Fourmentraux *et al.*, 2012; Voloschina *et al.*, 2018). Thermobarometry estimates of crystallisation depth suggest a main region of magma storage around 8 km (Astbury *et al.*, 2018; Giordano and Caricchi, 2022), with slightly shallower estimates of ~3–6 km from chlorine geobarometry (Balcone-Boissard *et al.*, 2024). Previous phase equilibria investigations at Campi Flegrei found observed compositions best

reproduced by crystallisation depths of 6–12 km for the CI and two post-15 ka eruptions (Minopoli 1 and Fondo Riccio; Bohrson *et al.*, 2006; Fowler *et al.*, 2007; Cannatelli, 2012). Measurements in melt inclusions from various eruptions agree on H_2O contents of 0.8–6% (Webster *et al.*, 2003; Cannatelli *et al.*, 2007; Mangiacapra *et al.*, 2008; Arienzo *et al.*, 2010, 2016; Fourmentraux *et al.*, 2012; Stock *et al.*, 2018), in agreement with estimates from K-feldspar-liquid hygrometry (Forni *et al.,* 2018) and phase equilibria investigations (Fowler *et al.*, 2007; Cannatelli, 2012). Forni *et al.* (2018) used oxygen barometry to constrain the oxygen fugacity (fO_2) for CI magmas to one log unit above the QFM buffer (QFM+1), similar to results of phase equilibria studies of the CI (Bohrson *et al.*, 2006; Fowler *et al.*, 2007), and Minopoli and Fondo Riccio eruptions (Cannatelli, 2012), where fO_2 between QFM and QFM+1 best reproduces the composition and phase assemblage of natural samples.

Lithology of the crust underlying Campi Flegrei

Modelling AFC processes requires understanding potential lithologies magmas might encounter during crustal ascent beneath Campi Flegrei. Geophysical and heat flow constraints on the structure of the Campanian crust generally suggest a Moho depth of <25km (Ferrucci *et al.*, 1989; Pontevivo and Panza, 2006; Nunziata, 2010). At ≲4 km depth, borehole data indicate that the shallow crust is composed of buried pyroclastic sequences, intercalated with Upper Miocene sedimentary sequences (Rosi and Sbrana, 1987; D'Antonio, 2011; Piochi *et al.*, 2014). At ≳4 km basement rocks are identified through their homogenous density in tomographic and gravity data (Battaglia *et al.*, 2008; Berrino *et al.*, 2008). However, due to similarities in their physical properties, the nature of the basement rocks beneath Campi Flegrei remains debated, with studies variously attributing it as Meso-Cenozoic carbonates (Judenherc and Zollo, 2004; Battaglia *et al.*, 2008; Zollo *et al.*, 2008), Palaeozoic metamorphic basement (previously termed Hercynian basement, e.g. Pappalardo *et al.*, 2002), or syenitic cumulate residue from past eruptions (Fowler *et al.*, 2007; D'Antonio, 2011). Insights into the basement lithology are

provided by erupted xenoliths, particularly the lithic-rich Breccia Museo unit of the CI (Fedele *et al.*, 2008) which contains plutonic syenite clasts (Fedele *et al.*, 2006; Gebauer *et al.*, 2014) in addition to hydrothermally altered lithic fragments from shallow lavas beneath the caldera (Di Vito *et al.*, 1999). Additionally, Pappalardo *et al.* (2002) identified two different xenolith types within deposits from the Minopoli 1 eruption; although the small clast size hampered detailed characterisation, these are suggested as deriving from Upper Miocene arenaceous sediments and the Palaeozoic metamorphic basement. Studies of isotopic variation in Campi Flegrei erupted products also provide information on potential crustal contamination sources: radiogenic and stable isotopic variation in magmas erupted in the last 60 kyr is attributed to interaction of the magmas with small amounts of both metamorphic Palaeozoic basement (~1-12% assimilation) and arenaceous sediments (<10% assimilation) Pappalardo *et al.*, 2002; D'Antonio *et al.*, 2007; Arienzo *et al.*, 2011; Di Renzo *et al.*, 2011, Iovine *et al.,* 2018). Despite the suggestion that assimilation plays a role in controlling the compositional evolution of Campi Flegrei magmas, this is yet to be empirically verified and the composition of the assimilant and extent of contamination are poorly defined.

ANALYTICAL METHODS

Sampling and sample preparation

To define the starting composition for our Rhyolite-MELTS models, we analysed melt inclusions in samples of tephras from the three most mafic post-15 ka Campi Flegrei eruptions: Minopoli 1, Minopoli 2 and Fondo Riccio (Smith *et al.*, 2011). Samples CF9 (Minopoli 2) and CF13 (Minopoli 1) were sampled by Smith *et al.* (2011) and sample CF410 (Fondo Riccio) was collected during fieldwork for this project in March 2022 (UTM 423047E, 4523062N). Samples were crushed and sieved, with clinopyroxene phenocrysts handpicked from the 250–500 μm size fraction.

Potential basement lithologies which might have contaminated Campi Flegrei magmas were sampled during fieldwork in May 2023. Sampling locations are given in Figure 1b and the Supplementary Material Table S1. These include: an upper Jurassic–lower Cretaceous limestone (sample 23-FMR-001, unit Gcb of Vitale and Ciarcia, 2018, no.2 on Fig. 1b); Upper Miocene syn-orogenic wedge-top deposits (previously termed flysch, e.g. Fowler *et al.,* 2007; sample 23-FMR-003, unit CVTg of Vitale and Ciarcia, 2018, no.1 on Fig. 1b); Palaeozoic gneiss (sample 23-FMR-017, Sila unit of Graessner and Schenk, 2001; Filice *et al.*, 2015, no.4 on Fig. 1b); and a syenitic xenolith from the Breccia Museo (sample 23-FMR-014, no.3 on Fig. 1b). These whole rocks were crushed in a tungsten carbide jaw crusher before being ground in an agate TEMA mill.

Electron probe microanalysis (EPMA)

Clinopyroxene phenocrysts from mafic Campi Flegrei eruptions were picked from tephra samples, mounted in epoxy, ground and polished for analysis. Crystals and melt inclusions were analysed using a JEOL JXA 8200 wavelength-dispersive electron microprobe in the Research Laboratory for Archaeology and the History of Art, University of Oxford, UK. All analyses were conducted with a 15 kV accelerating voltage and a 6 nA beam current and 10 µm beam diameter were used to analyse the melt inclusions, while a 25 nA current and 3 µm beam were used to analyse the host crystals. Appropriate natural and synthetic standards were used for calibration, and the MPI-DING reference glasses (Jochum *et al.*, 2006) were analysed as secondary standards to check the accuracy and reproducibility of results, compared to the preferred values. Accuracy was typically better than 2% with precision typically <±0.5% RSD for Si and ~±3% for most other major elements except for Na (~±11%) and low abundance elements Ti (±6%) and Mn (±16%). All Fe is assumed to occur as FeO (FeO(t)). All EPMA analyses are included in the Table S2.

X-Ray Fluorescence (XRF) analysis

Samples were prepared as fused glass beads and pressed powder pellets for whole-rock major (>1 wt%) and trace (<1 wt%) element analysis, respectively. Analyses were performed using the Zetium Wavelength Dispersive (WD) XRF in the Earth Surface Research Lab, Trinity College Dublin, following the methods described in Carter *et al.* (2024). From measurements of secondary standards analysed alongside the samples, accuracy is <2% for major and 5-10% for trace elements, and precision (in terms of relative standard deviation, standard deviation/mean) is generally <1% for major elements and <2% for trace elements. Data are included in Table S1.

LITERATURE DATA

Matrix glass data from post-15 ka Campi Flegrei eruptions were compiled from the literature for comparison with Rhyolite-MELTS outputs (Table S3). While bulk-rock and melt inclusion analyses might record liquid compositions, these can be affected by crystal accumulation/fractionation (e.g. Passmore *et al.*, 2012; Higgins and Stock, 2024) and post-entrapment processes (Lowenstern, 1995; Cannatelli *et al.*, 2016) and we exclude them from our analyses, instead preferring to limit the risk of misinterpretation by like-for-like directly comparing the last liquid remaining in the magmatic system before eruption. We investigate the processes affecting major element variability between eruptions, which does not preclude other processes, such as volatile fluxing and magma mixing, that have been reported for post-15 ka erupted products (e.g. Di Renzo *et al.,* 2011; Arienzo *et al.,* 2016). The compositions of natural glasses erupted from Campi Flegrei in the past 15 kyr were compiled from the GEOROC database (Sarbas, 2008); this yielded glass analyses from 48 eruptions and ~1900 analyses in total (Di Girolamo *et al.*, 1984; de Vita *et al.*, 1999; Brocchini *et al.*, 2001; Romano *et al.*, 2003; Piochi *et al.*, 2008; Smith *et al.*, 2011; Fourmentraux *et al.*, 2012; Tomlinson *et al.*, 2012; Arienzo *et al.*, 2016; Stock *et al.*, 2018). Of these, 1036 matrix glass analyses are from 6 western caldera eruptions, 620 are from 20 northern/eastern caldera eruptions and 255 are from 22

central caldera eruptions. No glass data is currently available for other post-15 ka eruptions (~20 eruptions in total; Smith *et al.,* 2011). There was no systematic difference in glass compositions between studies. Due to the number of glass compositions in our dataset, the uncertainty of the EPMA measurements collapse in, assuming a normal distribution. Therefore, any misfit between models and the data is probably not an artefact of EPMA uncertainty.

RHYOLITE-MELTS THERMODYNAMIC MODELLING

We modelled the major element compositional evolution of liquid and mineral phases in Campi Flegrei during FC and AFC using the Rhyolite-MELTS thermodynamic modelling software, which calculates the stable phase assemblage in a system under a given set of conditions based on minimisation of free energy, with the thermodynamic properties of each phase calibrated from experiments (Gualda *et al.*, 2012). We used Rhyolite-MELTS v.1.2. which has a coupled H_2O-CO_2 fluid saturation model and the most comprehensive calibration dataset to date (Ghiorso and Gualda, 2015). The models were run using the alphaMELTS2 front-end (Smith and Asimow, 2005), with a Python-based script designed to batch run simulations over a range of potential storage conditions (see Gainsforth *et al.,* 2015; Antoshechkina and Ghiorso, 2018; Gleeson *et al.,* 2023). We model fractional crystallisation as opposed to equilibrium crystallisation, following previous thermodynamic modelling (Fowler *et al.,* 2007, Cannatelli, 2012) and empirical major element geochemical studies (Civetta *et al.,* 1991) which suggest that this process best describes the relationship between the compositions of Campi Flegrei erupted products.

Despite previous studies identifying isotopic heterogeneity in Campi Flegrei erupted compositions (e.g. D'Antonio *et al.,* 2007; Arienzo *et al.,* 2010; Di Renzo *et al.,* 2011) and suggesting separate end-member magma batches, these are not reflected in variations in major element chemistry, where eruptions can be related by crystallisation to a single parental magma (Civetta *et al.,* 1991; Smith *et al.,* 2011). We therefore model crystallisation of a single parental

magma, using the most primitive melt inclusion that we measured in mafic post-15 ka eruptions as the starting composition in our models (CF410_cpx12_MI18; Table S2). This clinopyroxene-hosted inclusion from Fondo Riccio has the highest MgO (6.23 wt%) and CaO (11.62 wt%) concentrations in our dataset and low incompatible element concentrations (Na_2O+K_2O 6.84 wt%), and is in equilibrium with its host crystal based on their $K_D(Fe\text{-}Mg)^{cpx\text{-}liq}$ of 0.31 ± 0.07 (i.e. within the equilibrium range of 0.28 ± 0.08 from Putirka, 2008). Masotta *et al.* (2013) identified that melt alkali content can affect these calculations, but their revised model converges with the $K_D(Fe\text{-}Mg)^{cpx\text{-}liq}$ range given in Putirka (2008) for $K_D > 0.2$, so we prefer to use this as it does not require prior knowledge of crystallisation temperature, although the narrow range likely reflects the majority of published experiments involving mafic systems with the actual equilibrium range potentially being larger (Di Fiore *et al.,* 2021). The selected melt inclusion is glassy, implying post-entrapment crystallisation (PEC) has not been extensive (Fig. S1) and a correction for PEC did not significantly alter our model outputs (Fig. S2). Although previous authors have reported more mafic melt inclusions (Webster *et al.*, 2003; Cannatelli *et al.*, 2007), they require extensive correction for post-entrapment crystallisation which can compromise their major element composition (Danyushevsky *et al.*, 2002; Kress and Ghiorso, 2004) so we prefer to use our own direct measurements.

Fractional crystallisation models

We initiated our FC models at the calculated liquidus and ended at a melt fraction of ~0.05 (5%; models fail closer to the solidus, likely due to extreme incompatible element enrichment in the melt phase), with a temperature step of 1°C. The proportions and compositions of all stable phases are recorded at each temperature step, with crystals removed from the bulk composition between steps. No constraints were placed on the phases Rhyolite-MELTS could stabilise; predicted phases were compared to those observed in natural samples. Model parameters (L_{fO2}, P, L_{H2O}) are defined for each model and, to constrain the conditions of Campi Flegrei magma

storage, we varied these parameters across the range of possible conditions previously identified in the literature (Table 1). We varied L_{fO2} by fixing it above the liquidus and then allowing fO_2 to vary unbuffered below the liquidus. In our FC models, we tested a matrix of parameter space so that each intensive variable was tested against the full range of the remaining two, totalling 1720 individual simulations. To reduce the modelled parameter space, we follow previous studies in only considering isobaric crystallisation (Fowler *et al.*, 2007; Cannatelli, 2012; Rooney *et al.*, 2012; Stock *et al.,* 2016; Gleeson *et al.*, 2017). While previous authors have suggested that the Campi Flegrei sub-volcanic system could have magmas stored at multiple depths (e.g. Astbury *et al.,* 2018; Giordano and Caricchi, 2022), we find the liquid lines of descent produced in our Rhyolite-MELTS models are not sensitive to polybaric crystallisation in the mid- to upper-crust within a reasonable pressure range (Fig. S3) and so consider only a simple isobaric scenario.

Assimilation models

Following Fowler *et al.* (2007), we model AFC taking the best-fit intensive parameters for each volcano-tectonic setting based on the results obtained from FC simulations (see *Statistical determination of best-fit storage conditions,* below) before adding a contaminant to Rhyolite-MELTS models at a fixed temperature, using the bulk compositions measured from samples of the basement lithology (Table S1; sample 23-FMR-001 = limestone; sample 23-FMR-003 = wedge-top deposits; sample 23-FMR-14A = syenite; sample 23-FMR-017 = Palaeozoic metamorphic basement). In each AFC model, we systematically varied the type and amount of assimilation, holding all other model parameters constant and producing 80 additional models. While we acknowledge that this is a simplification, simultaneously changing the type of assimilant, temperature interval over which contamination occurs, conditions of magma storage (P, L_{fO2}, L_{H2O}) and adding mixtures of different assimilants creates an unmanageably large parameter space. Instead, our approach assumes that the intrinsic conditions of magma storage

exert a first-order control on the liquid line of descent and that small amounts of assimilation of a dominant assimilant composition have a second-order impact. Rhyolite-MELTS can simulate assimilation under either isenthalpic or isothermal conditions (Ghiorso and Kelemen, 1987) which can constrain different aspects of assimilation. To investigate the effect different assimilant compositions on the liquid line of descent in a long-lived magmatic system, we follow Fowler *et al.* (2007) in running AFC models isothermally, whereby the initial temperature of the assimilant is the same as the melt. Each model was run as a closed system FC simulation from the liquidus to 1100°C before the assimilant was added and chemically equilibrated with the new system. The melt then evolved once again down to low melt fractions, reducing temperature by 1°C and extracting crystals at each step, as in FC models. The amount of assimilant was varied between M_a/M_m = 0.01–0.3 in 0.05 increments, where M_a/M_m is the ratio of assimilant to melt (equivalent to 1–30% contamination).

Statistical determination of best-fit storage conditions

Most previous studies which have determined magmatic processes/storage conditions by correlating the compositions of natural erupted materials with Rhyolite-MELTS outputs have qualitatively identified the best-fit model run conditions "by eye" (e.g. Fowler *et al.*, 2007; Fowler and Spera, 2010; Cannatelli, 2012). This approach was advanced by Gleeson *et al.* (2017), who employed a statistical method based on least-squares analysis to quantitively determine the best-fit model conditions, comparing the residuals between compositional evolution of the modelled melt phase and whole-rock samples from Aluto volcano (Ethiopia). We build on this work, implementing an improved statistical assessment to determine the correlation between each of our 1800 (1720 FC and 80 AFC) Rhyolite-MELTS models and natural matrix glasses from Campi Flegrei. Rather than comparing models against our full literature dataset, we separate post-15 ka Campi Flegrei glasses into three groups, based on the volcano-tectonic setting of their eruption vents (i.e. western caldera eruptions, northern/eastern

caldera eruptions, central caldera eruptions) to identify changes in magma storage conditions and/or processes across the caldera.

Our statistical procedure for identifying best-fit models is as follows: for each oxide output by Rhyolite-MELTS (except P_2O_5 which is in too low concentration), we calculated the root mean square error (RMSE) between the modelled liquid line of descent and natural Campi Flegrei matrix glasses following Willmott (1981):

$$\mathrm{RMSE}_A = \sqrt{\frac{\sum_i^n (y_{i,A} - \hat{y}_{i,A})^2}{n}} \qquad \text{(eq. 1)}$$

where RMSE_A is the root mean square error for oxide A, n is the number of natural samples whose composition we are comparing against Rhyolite-MELTS outputs; $y_{i,A}$ is the concentration of major oxide A in natural sample i at a given MgO concentration; and $\hat{y}_{i,A}$ is the concentration major oxide A predicted by Rhyolite-MELTS for the same MgO concentration. In this approach, MgO is an index of fractionation, decreasing along the liquid line of descent as it is incorporated into phases such as olivine, clinopyroxene and spinel group minerals.

The RMSE is in units of the variable y (in our case, wt%) and, as the concentration of major oxides varies considerably in natural volcanic glasses (e.g. ~1 wt% TiO_2 to >50% SiO_2 in our samples), the magnitude of RMSE varies accordingly. As a result, we normalised each RMSE value to the average concentration of the major oxide in our natural Campi Flegrei matrix glasses:

$$\mathrm{RMSE}_{\mathrm{norm},A} = \frac{RMSE_A}{\bar{X}_A} \qquad \text{(eq. 2)}$$

where $\mathrm{RMSE}_{\mathrm{norm},A}$ is the normalised root mean square error for oxide A and $\bar{X}_A$ is mean concentration of oxide A in all of our natural Campi Flegrei glasses.

The $RMSE_{norm}$ values for each major oxide were then summed to give a single, total RMSE ($RMSE_{total}$) for each model:

$$RMSE_{total} = \sum RMSE_{norm} \quad \text{(eq.3)}$$

By identifying our Rhyolite-MELTS model which produces the lowest $RMSE_{total}$, we constrained the input conditions which best reproduce the liquid line of descent recorded by natural Campi Flegrei erupted products and thus mirror the most likely conditions of sub-volcanic magma storage. We have provided a sample Python code to calculate the RMSE of Rhyolite-MELTS models at doi:10.5281/zenodo.14900107. Our approach builds on the work of Gleeson *et al.* (2017) by comparing Rhyolite-MELTS outputs to natural data throughout the entire crystallisation sequence from the most mafic to evolved samples, assessing which combination of intensive parameters best reproduces the observed liquid line of descent.

Our statistical measure of the best-fit conditions was supplemented by comparison of the phase assemblages predicted by Rhyolite-MELTS and those observed in natural samples (see *Fractional crystallisation models,* below).

Potential limitations of Rhyolite-MELTS

Previous studies using MELTS to constrain magma storage conditions, including those for the petrogenesis of the CI, note a displacement of up to ~3 wt% between predicted melt K_2O and CaO concentrations and those measured in natural samples (Fowler *et al.*, 2007; Fowler and Spera, 2010). The CaO discrepancy is likely due to under-stabilisation of clinopyroxene (Fowler and Spera, 2010), whereas the K_2O discrepancy may be the result of MELTS over stabilising sanidine due to a paucity of experimental data available for calibrating the alkali feldspar–liquid equilibria (Gualda *et al.*, 2012). The calibration of Rhyolite-MELTS used in this study (v.1.2.) remedies this issue by adjusting the stability of quartz and the potassium end-member of alkali feldspar and hence is more suitable for the alkali Campi Flegrei magmas

(Gualda *et al.*, 2012). Rooney *et al.* (2012) note that Rhyolite-MELTS also overpredicts melt P_2O_5 concentrations, which they attribute to inaccuracies in the apatite solubility model. However, due to the low P_2O_5 concentrations in all our natural Campi Flegrei samples (generally approaching the lower limit of detection), this element is not considered in our subsequent estimates of best-fit storage conditions.

Rhyolite-MELTS is inherently limited by a lack of hydrous phase-bearing experiments and thermodynamic models for hydrous mafic silicates, making it largely inappropriate for systems where hydrous minerals are major phases controlling the liquid line of descent (e.g. amphibole-rich rhyolites; Gualda *et al.*, 2012). However, in Campi Flegrei hydrous minerals (e.g. biotite, apatite) are ubiquitously minor phases (Isaia *et al.*, 2004; Smith *et al.*, 2011; Stock *et al.*, 2018), hence we expect inaccuracies in reproducing hydrous mineral stabilities will have minimal impact on our model outputs. Sanidine compositions calculated by Rhyolite-MELTS are also more sodic than observed in natural samples, with sanidine appearing on the liquidus at higher temperatures (~40°C) compared to thermometry and experiments on natural systems (Gualda *et al.*, 2012; Gardner *et al.*, 2014; Gleeson *et al.*, 2017). However, as sanidine generally appears at low melt fractions (Fowler *et al.*, 2007; Cannatelli, 2012), it is also unlikely to significantly impact our model results for the questions posed in this study.

Rhyolite-MELTS remains an extremely valuable tool for evaluating how reasonable different scenarios are (FC and AFC), despite model inaccuracies largely related to the availability of experimental data. It has been successfully applied to model phase equilibria across a range of volcanic systems (e.g. recently Knafelc *et al.*, 2020; Boschetty *et al.*, 2022; Fred *et al.*, 2022). By comparing the fit of models run over a wide range of starting conditions to the natural data from Campi Flegrei, we can place new constraints on processes operating in the sub-volcanic system.

RESULTS

Compositional variation in post-15 ka Campi Flegrei glasses

Post-15 ka Campi Flegrei eruptions derived from vents in the three volcano-tectonic groups have distinct matrix glass compositions (although some overlap between compositions exists, Fig. 2, Fig. S4, D'Antonio *et al.*, 1999; Di Renzo *et al.*, 2011; Smith *et al.*, 2011). The northern and eastern caldera eruptions are the most mafic (typically shoshonite–tephriphonolite) with the highest MgO, FeO and CaO concentrations and the lowest SiO_2 content. The Minopoli 2 eruption forms a distinct high MgO group separate from other eruptions (Fig.2). Western caldera eruptions extend to the most evolved compositions (trachyte–phonolite), with low MgO, high SiO_2 and elevated Na_2O concentrations, forming a distinct low-K_2O, high-SiO_2 group (Fig. 2c). At very low MgO concentrations, western caldera eruptions also tend towards elevated TiO_2 and Na_2O and depleted K_2O. Central caldera eruptions are typically intermediate between the other two groups in terms of their extent of evolution, ranging from tephriphonolites to phonolites/trachytes. They have the highest K_2O concentrations and variable Al_2O_3.

Fractional crystallisation models

All our FC models show comparable geochemical trends with phases coming onto the liquidus in a similar order (Fig. 3). Depending on the intensive parameters, olivine or clinopyroxene are the liquidus phases (1100-1180˚C) for all models, with clinopyroxene being the second phase to precipitate if not on the liquidus (Fig. S5). Spinel group minerals (predominantly magnetite; typically 1050-1120 ˚C) and plagioclase (typically 975-1050˚C) precipitate next but their saturation temperatures depend strongly on the model pressure, L_{H2O} and L_{fo2} (see below). Small amounts of biotite (890-945˚C), K-feldspar (sanidine; 805-890˚C) and, in some models, leucite (800-950˚C) come onto the liquidus at low temperatures. In a small number of models, olivine (~850˚C), nepheline (720-735˚C), garnet (705˚C) or muscovite (~730˚C) precipitate close to

493 the solidus. Aside from these occasional near-solidus phases, the modelled phase assemblage
494 mirrors that observed in post-15 ka Campi Flegrei eruptions (Stock et al., 2018).

495 Regarding the liquid line of descent, clinopyroxene-only crystallisation drives a
496 decrease in MgO and CaO (from ~6 to 4.5 wt% and 11 to 9.5 wt% at *spinel-in* respectively),
497 with other oxides (Al_2O_3, K_2O, Na_2O, FeO, TiO_2) increasing in the residual liquid at high melt
498 fractions, with FeO and TiO_2 beginning to decrease when spinel group minerals come onto the
499 liquidus and the liquid evolves from shoshonite to latite. The onset of plagioclase crystallisation
500 causes an inflection in Al_2O_3 with decreasing MgO as crystallisation continues, where Al_2O_3
501 becomes compatible in the crystallising assemblage and the liquid evolves from latite to
502 tephriphonolite; plagioclase is initially Ca-rich, further driving the decrease in the liquid CaO
503 concentration, but becomes increasingly sodic at lower temperatures, reducing the rate of Na_2O
504 enrichment in the liquid. K-feldspar comes onto the liquidus when MgO has decreased to ~0.2
505 wt%; at this point K_2O becomes compatible in the crystallising assemblage and is depleted in
506 the residual liquid, with the liquid evolving towards phonolite. This is accompanied by a sharp
507 Na_2O enrichment in the liquid as the fraction of crystallising plagioclase decreases. Sharp
508 compositional changes at very low MgO contents in both FC and AFC models (e.g. Fig. 4e) are
509 likely a result of limitations modelling minor minerals which accommodate incompatible
510 elements at low melt fractions (Gualda *et al.,* 2012). Although these trends hold generally for
511 each of our simulations, the exact nature of the liquid line of descent depends on the liquidus
512 temperature of each mineral phase and the proportions of crystallising solid, which vary as a
513 function of the model intensive parameters.

514 *Varying the initial H_2O content*

515 Although varying L_{H2O} does not have a significant effect on the type or order of minerals
516 crystalising in our Rhyolite-MELTS models (Fig. S6), small differences in their solidus
517 temperatures, modal proportions and compositions have significant effects on the liquid line of

descent (Fig. 4). This is particularly the case for plagioclase, where crystal anorthite contents are highly sensitive to the H_2O content of their equilibrium melt (Lange *et al.*, 2009). At low L_{H2O} (~0.5– 3 wt%), feldspar minerals stop crystallising at relatively high temperatures (~775-850˚C), leading K_2O to behave incompatibly in the crystallising assemblage at low temperatures (below 800˚C) and MgO contents. Conversely, at high L_{H2O} (~4–6 wt%), feldspar continues to crystallise until the solidus and CaO behaves incompatibly in the melt at low temperatures (below ~810 ˚C). Reducing L_{H2O} to <4% significantly reduces sanidine stability, resulting in very high melt Al_2O_3 contents (20-22 wt%; Fig. 4a). Prediction of sanidine compositions is a known limitation of Rhyolite-MELTS (Gualda *et al.,* 2012; Gardner *et al.,* 2014) which might explain these differences. Higher L_{H2O} leads to a greater proportion of feldspar crystallising overall (~0.47 for 6 wt% L_{H2O} compared to ~0.38 for 1 wt%, largely due to differences in the amount of sanidine predicted to crystallise). Initial melt H_2O content also has an impact on the predicted clinopyroxene composition which affects the melt TiO_2 content. At high L_{H2O} (>3%), clinopyroxene has higher TiO_2 contents, especially at high temperatures, so crystallisation strongly drives down the melt TiO_2 content, whereas at lower L_{H2O} (<2%), clinopyroxene TiO_2 content is much lower until low temperatures, so the TiO_2 content remains elevated (Fig. 4c). Increasing L_{H2O} reduces the TiO_2 content of spinel group minerals, but the small quantities (~0.05) of spinel group minerals crystallised means the effect on melt TiO_2 content is minimal compared to clinopyroxene.

Varying oxygen fugacity

Increasing L_{fO2} in our Rhyolite-MELTS models increases the stability of spinel group minerals which primarily impacts the SiO_2 and FeO concentrations of the residual melt during fractional crystallisation: under more oxidising conditions, where spinel group minerals stabilise at higher temperatures, melt SiO_2 concentrations begin to increase at higher temperatures and FeO contents are lower for any given MgO content (Fig. 4e). The earlier precipitation of spinel group

minerals under more oxidising conditions is consistent with experimental studies (Toplis and Carroll, 1995; Feig *et al.*, 2010). Varying L_{fO2} also effects the liquid line of descent for TiO_2 with generally lower melt TiO_2 concentrations in the more oxidised models, again because of the earlier spinel group minerals fractionation but also differences in the predicted clinopyroxene composition which initially contains more TiO_2 (Fig. 4f). However, at QFM+3, spinel minerals contain less TiO_2 than at QFM, so at lower L_{fO2} there is a steeper reduction of TiO_2 in the melt after *spinel-in*.

Varying pressure

Changing pressure in our Rhyolite-MELTS models has minor impacts on the predicted phase assemblage. The major mineral phases observed in Campi Flegrei erupted products – clinopyroxene, plagioclase feldspar, alkali feldspar – are predicted to crystallise across all pressures (Fig. 3, Fig. S5). However, at high pressures (>200 MPa), Rhyolite-MELTS predicts minor muscovite and garnet crystallisation close to the solidus (Fig. 3c). Likewise, at low pressures (<70 MPa), leucite is predicted to crystallise in significant quantities (~7%, Fig. 3a). The liquid line of descent is not very sensitive to pressure; for all major oxides there is generally <1 wt% difference in the predicted concentration of the oxide at equivalent MgO/temperature steps across the entire range of pressures (Fig. 4g-i). Small differences between models run at opposing ends of our pressure range observed at low temperature likely reflect the crystallisation of near-solidus muscovite, garnet and leucite.

Modelling assimilation – fractional crystallisation

The major and trace element compositions of basement rocks which represent potential Campi Flegrei assimilants are listed in Table S1. The addition of an assimilant to our Rhyolite-MELTS models produces similar geochemical trends for all volcano-tectonic groups, although these trends differ for each assimilant composition.

567 *Assimilation of Palaeozoic metamorphic basement*

568 The addition of Palaeozoic metamorphic basement assimilant to our Rhyolite-MELTS models
569 significantly increases the predicted melt SiO_2 content and reduces the predicted Al_2O_3 content,
570 relative to FC models run with the same set of intensive variables (Fig. S9, S13, S17); these
571 effects increase with increasing quantities of the contaminant. Small quantities of Palaeozoic
572 metamorphic contamination cause melt K_2O and Na_2O contents to increase at low temperatures
573 and melt fractions, due to changes in the predicted phase assemblage: in models with M_a/M_m =
574 0.1 feldspar stops crystallising ~80˚ C higher temperature than for M_a/M_m = 0.3. For models
575 with M_a/M_m >0.2, Rhyolite-MELTS predicts crystallisation of quartz at low temperatures.

576 *Assimilation of syn-orogenic wedge-top deposits*

577 Addition of wedge-top deposits increases the predicted SiO_2 content of the melt in our Rhyolite-
578 MELTS models compared to FC under equivalent storage conditions, especially at low
579 temperatures and melt fractions (Fig. S8, S12, S16); at M_a/M_m = 0.3, the SiO_2 content of the
580 residual melt is predicted to reach ~72 wt% at low temperatures. Addition of wedge-top deposits
581 also slightly increases the predicted melt CaO concentration and decreases the melt FeO, K_2O,
582 Na_2O and Al_2O_3 at equivalent MgO content compared to FC models with the same intensive
583 parameters, with the magnitude of these changes increasing with the amount of assimilant. For
584 small amounts of wedge-top deposit assimilation, sanidine stops crystallising at higher
585 temperatures, leading to K_2O incompatibility at low temperatures, whereas larger amounts of
586 wedge-top deposit assimilation causes more Na-rich plagioclase to crystallise, lowering the
587 Na_2O contents of the residual melt.

588 *Assimilation of limestone*

589 Addition of limestone in our Rhyolite-MELTS models has the most significant impact on the
590 predicted CaO concentration (Fig. S7, S11, S15), causing it to increase relative to FC models

591 run with the same intensive parameters. Conversely, the predicted liquid SiO_2 content is much
592 lower relative to equivalent FC models at a given MgO concentration. These effects increase
593 with greater amounts of limestone contamination, especially at M_a/M_m >0.01 (Fig. S7, S11,
594 S15). To a lesser extent, at equivalent melt MgO content, limestone assimilation causes slightly
595 lower FeO and Al_2O_3 contents and slightly higher TiO_2 relative to equivalent FC models and
596 with limestone addition at M_a/M_m >0.05 Rhyolite-MELTS predicts minor garnet crystallisation
597 at best-fitting intensive parameters for uncontaminated FC.

598 *Assimilation of syenite*

599 Where a syenite assimilant is added to our Rhyolite-MELTS models, melt SiO_2 contents are
600 higher and Al_2O_3 contents are lower than in FC models run under equivalent conditions at the
601 same melt MgO content, due to greater proportions of crystallising feldspar. For the other major
602 oxides, adding syenite does not significantly change the liquid line of descent compared to
603 equivalent FC models, saving a small reduction in K_2O content and increase in Na_2O, CaO and
604 TiO_2 concentrations. In all cases, the predicted liquid lines of descent are similar irrespective
605 of the quantity of contaminant (Fig. S10, S14, S18).

606 **DISCUSSION**

607 **Constraints on magma storage conditions**

608 Contrasting major element compositions of matrix glasses erupted from vents in different
609 volcano-tectonic settings allude to variations in the structure and/or processes operating within
610 the sub-volcanic plumbing system in different parts of the Campi Flegrei caldera. Changing
611 L_{H2O}, L_{fO2} and P in our models affects the predicted liquid line of descent (Fig. 4), which in turn
612 controls how well the models match measured natural glass compositions from Campi Flegrei
613 (Fig. 5). Our RMSE statistical test constrains the combination of intensive parameters which

produce the best-fit between the liquid line of descent predicted by Rhyolite-MELTS FC models and that recorded by natural glass compositions (Table 2; Tables S4–S6).

Liquidus H_2O concentration

Varying L_{H2O} between 1–6 wt% markedly changes the stability of feldspar, with *feldspar-in* occurring at higher temperatures for lower H_2O contents, as observed in previous experimental (Eggler, 1972; Gaetani *et al.*, 1993; Sisson and Grove, 1993; Lange *et al.*, 2009), MELTS based studies (Fowler *et al.,* 2007; Cannatelli 2012) and observations of erupted plagioclase textures and compositions (e.g. at Stromboli - Landi *et al.,* 2004) . At the lower end of our L_{H2O} range (0.5-2 wt%), our models predict an enrichment in the melt K_2O at low temperatures (i.e. incompatible behaviour) and consistently high melt TiO_2 contents, which are not observed in natural Campi Flegrei samples (Fig. S4). Similarly, at the top of our L_{H2O} range (5-6 wt%), Rhyolite-MELTS predicts that the melt becomes enriched in CaO at low temperatures, with consistently low TiO_2 and high Al_2O_3 concentrations, which are also not observed. These constraints lead to higher RMSE for models with L_{H2O} outside 2-3 wt% (Fig. 5a,d,g). For northern/eastern and western caldera eruptions, the natural glass compositions are best reproduced by crystallisation with 2 wt% L_{H2O}, whereas the central caldera eruptions are best reproduced with a higher L_{H2O} of 3 wt%.

The best-fit L_{H2O} for each volcano-tectonic setting (2–3 wt%) are consistent with previous measurements of mafic melt inclusion H_2O concentrations (Webster *et al.*, 2003; Cannatelli *et al.*, 2007; Mangiacapra *et al.*, 2008; Stock *et al.*, 2018), those determined experimentally (Perinelli *et al.*, 2019) and L_{H2O} values used in previous thermodynamic modelling of Campi Flegrei eruptions (Bohrson *et al.*, 2006; Fowler *et al.*, 2007; Cannatelli, 2012; Stock *et al.*, 2016). Forni *et al.* (2018) assessed the H_2O contents of melts in equilibrium with late-crystallising K-feldspar were higher than those of near liquidus melts (i.e. prior significant crystallisation of anhydrous minerals), and also suggested that the H_2O content of

Campi Flegrei magmas increased over the past 15 ka, from 0.5–3.5 wt% in the Epoch 1 Minopoli 1 and 2 eruptions to 3–6 wt% in the Epoch 3 Astroni and Monte Nuovo eruptions. However, their study only included a small number (12) of eruptions from the past 15-kyr and did not consider the possibility for a spatial, rather than temporal, correlation. As earlier eruptions generally occurred along the caldera rim and migrated towards the centre of the caldera over time (Smith *et al.*, 2011), their results are equally compatible with differences in L_{H2O} between volcano-tectonic groups. Eruptions from vents on the caldera rim (e.g. Minopoli 1 and 2, Soccavo 4) were identified by Forni *et al.* (2018) as having lower H_2O contents than eruptions in the central caldera (e.g. Astroni, Agnano-Monte Spina). The eruption of Monte Nuovo, in the western caldera but with the highest H_2O content in the last 15 kyr, is the exception, which may be related to extensive fractionation at low temperatures.

The differences in best-fit L_{H2O} between our volcano-tectonic groups could reflect changes in the H_2O content of near-primitive mantle melts feeding Campi Flegrei eruptions in different parts of the caldera system. However, despite their different structural setting, post-15 kyr Campi Flegrei eruptions are relatively closely spaced (e.g. ~1 km between some central and caldera rim vents) relative to a whole arc or ocean island scale, and L_{H2O} variations would need to occur on significantly shorter length scales than any previously reported mantle heterogeneity (e.g. Kelemen *et al.*, 2003; Gibson *et al.*, 2012; Sims *et al.*, 2013). Consequently, we discount mantle heterogeneity as the potential source for variable L_{H2O} across the caldera. Instead, we suggest that variations in L_{H2O} between magmas in different volcano-tectonic settings result from interaction with hydrothermal water; such magma-fluid interaction has been suggested previously for Campi Flegrei eruptions on the basis of trace element and isotopic variation (Villemant, 1988; Civetta *et al.,* 1991). Although our approach cannot determine whether hydrothermal interaction and magma hydration genuinely occurred above the liquidus (i.e. as opposed to after some crystallisation), addition of water to the melt must have occurred

at high enough temperatures and melt fractions to impact the crystallising phase assemblage. Campi Flegrei currently has a highly active hydrothermal system focused around Solfatara, in the central caldera (Troiano *et al.,* 2022) with geological evidence that this has persisted over the past 15 kyr (Isaia *et al.,* 2009). While the main hydrothermal aquifer beneath Campi Flegrei is currently within the shallow crust (2–3 km; Troiano *et al.,* 2022) above the main zone of magma storage (see below), the eruption of hydrothermally altered syenitic lithics (Fedele *et al.,* 2006; Gebauer *et al.,* 2014) suggests that fluids may be present at significantly greater depths; this is supported by recent magnetotelluric imaging which shows a volatile-rich zone extending to ~8 km (Isaia *et al.*, 2025).

Oxygen fugacity

Varying L_{fO2} between QFM-2 and QFM+3 has a significant effect on the predicted liquid line of descent, particularly for FeO and SiO_2 which are most impacted by changes in spinel stability (Fig. 4e). Under more oxidising conditions, spinel group minerals stabilise at higher temperatures resulting in lower FeO and higher SiO_2 concentrations in the residual melt, as observed in experimental studies (Hill and Roeder, 1974; Fisk and Bence, 1980). For L_{fO2} >QFM+1, the predicted liquid line of descent for FeO significantly deviates from that measured in natural Campi Flegrei glasses, leading to higher RMSE for these models (Fig. 5b,e,h). For central and western caldera eruptions, the natural glass compositions are best reproduced by crystallisation with L_{fO2} at the QFM buffer; northern/eastern caldera eruptions are best reproduced with L_{fO2} QFM+1.

Our best-fit L_{fO2} of QFM to QFM+1 suggests that the liquidus oxidation state of the magma is broadly similar across the caldera. Although we do not fix fO_2 to a buffering reaction below the liquidus in our models (as these reactions very rarely occur in nature; Anenburg and O'Neill, 2018), our best-fit L_{fO2} range agrees well with previous thermodynamic modelling (Bohrson *et al.*, 2006; Fowler *et al.*, 2007; Cannatelli, 2012) and experimental studies

689 (Fabbrizio and Carroll, 2008) which have consistently reproduced the phase assemblage of
690 Campi Flegrei erupted products with fO_2 buffered between QFM and QFM+1.8 (close to Ni-
691 NiO+1 at magmatic conditions, Frost, 1991). Our results are also consistent with fO_2 estimates
692 for the Campanian Ignimbrite calculated by spinel-melt oxybarometry (QFM+1; Forni *et al.*,
693 2016).

694 *Pressure*

695 Varying pressure in the range 50–500 MPa has minimal effect on the liquid line of descent of
696 all the major oxides (Fig. 4g-i), with the predicted concentrations of major oxides varying by
697 <1% at any given MgO concentration or temperature across the entire range of pressures (where
698 other intrinsic variables are constant). Therefore, our RMSE statistical method is not an accurate
699 discriminator of best-fit pressure. Eggler (1972) experimentally demonstrated that plagioclase
700 stability is strongly sensitive to the equilibrium melt H_2O content but relatively insensitive to
701 pressure, with melt-H_2O sensitivity also observed in erupted products at Stromboli by Landi *et*
702 *al.* (2004). As plagioclase is a major crystallising phase in Campi Flegrei magmas (Isaia *et al.,*
703 2004; Piochi *et al.,* 2005; Stock *et al.,* 2018), this may partly explain the models' relative
704 insensitivity to pressure variations. However, while the overall liquid line of descent predicted
705 by Rhyolite-MELTS is relatively pressure insensitive, the mineral phase assemblage does vary
706 close to the solidus and allows for some constraint on the most probable storage conditions.
707 Our models predict that relatively late-stage muscovite and garnet will crystallise in Campi
708 Flegrei magmas at pressures >200 MPa and that ~7% of leucite will precipitate at pressures <70
709 MPa (Fig. 3, Fig. S5). Muscovite and garnet have never been reported in any Campi Flegrei
710 eruption products and leucite has only been observed rarely in low concentration (Isaia *et al.*,
711 2004; Smith *et al.*, 2011; Stock *et al.*, 2018); hence, these pressures likely represent unrealistic
712 magma storage conditions. Despite our models run at intermediate pressures having the highest
713 RMSE when comparing predicted liquid lines of descent to natural glasses (i.e. RMSEs

decrease at both low and high pressures; Fig. 5c,f,i), this mineralogical disparity constrains storage pressures to the range 70–200 MPa. Within this range, the best-fit pressure for each volcano-tectonic group can be determined approximately by the lowest RMSE for SiO_2, which is the most sensitive to pressure variations. For northern/eastern caldera eruptions, the natural glass compositions are best reproduced by crystallisation at 110 MPa, for central caldera eruptions the best-fit pressure increases to 140 MPa and is highest for western caldera eruptions, at 160 MPa.

Given an average Campanian crustal density of 2.3 g cm^{-3} after Rosi and Sbrana (1987), our approximated crystallisation pressures correspond to magma storage depths in the range ~5–7 km. This broadly agrees with previous phase equilibria investigations at Campi Flegrei, which visually identified that the compositions of natural samples were best reproduced by models run at pressures equivalent to 6–12 km (150-300 MPa; Bohrson *et al.*, 2006; Fowler *et al.*, 2007; Cannatelli, 2012). Despite the inherent insensitivity of our method, our crystallisation depth estimate also agrees reasonably with independent petrological and geophysical constraints on the structure of the Campi Flegrei magmatic system, which predict the main magma storage region to be located at ~7–8 km (e.g. Zollo *et al.,* 2008; Stock et al., 2018; Petrelli *et al.*, 2023; Isaia *et al.,* 2025). Critically, our depth estimates are not consistent with shallower crystallisation at 3–4 km, which corresponds with the depth of the current deformation source (Woo and Kilburn, 2010; Amoruso *et al.*, 2014; D'Auria *et al.*, 2015) and most recent seismicity (Scotto di Uccio *et al.*, 2024). This shallow unrest has previously been linked to fluid migration in the active hydrothermal system beneath Campi Flegrei (Troiano *et al.*, 2011; Chiodini *et al.*, 2012, 2015b) and may occur at the same depth as small/ephemeral sill intrusions (Stock et al. 2018). Rather, our data support the majority of magma storage and crystallisation occurring in the mid-lower crust.

Volcano-tectonic controls on assimilation

739 Rhyolite-MELTS FC models can produce best-fit liquid lines of descent which correlate
740 reasonably with natural glass compositions for some major oxides (e.g CaO, FeO; Fig. S19-
741 S21) and there is good agreement between the modelled phase assemblages and those observed
742 in Campi Flegrei erupted products. However, models fail to reproduce natural glass
743 compositions for other major oxides under any set of intensive parameters. For example,
744 modelled Al_2O_3 concentrations are consistently higher than in natural glasses, whereas SiO_2
745 concentrations are consistently lower (Fig. 6). While models are able to reproduce the K_2O
746 composition of erupted glasses from northern/eastern and central caldera volcano-tectonic
747 groups, the lower K_2O concentration of western caldera eruptions is not reproduced by any of
748 our FC models (Fig. S21). These discrepancies suggest that assimilation may play a role in
749 controlling the Campi Flegrei liquid line of descent, where addition of a contaminant could
750 improve the fit between our model outputs and natural glass compositions.

751 Despite evidence for extensive limestone contamination at Vesuvius (~25 km east of
752 Campi Flegrei; Del Moro *et al.*, 2001; Iacono Marziano *et al.*, 2008) and previous authors
753 interpreting this as a potential contaminant of Campi Flegrei magmas (Iacono Marziano *et al.*,
754 2008; Pappalardo and Mastrolorenzo, 2012) addition of limestone does not significantly
755 improve the fit between predicted and observed liquid lines of descent in post-15 ka volcano-
756 tectonic groups relative to FC alone. This is reflected in limestone contamination producing
757 only a very minor decreases in the RMSE between modelled and observed glass compositions;
758 increasing quantities of a limestone assimilant lowers the melt SiO_2 concentration and increases
759 CaO, forcing the predicted liquid line of descent for these elements away from the observed
760 compositions of all volcano-tectonic groups (Fig. S7, S11, S15). At M_a/M_m >0.05, limestone-
761 contaminated models predict the crystallisation of garnet, which has never been observed in
762 natural Campi Flegrei samples. Hence, in contrast with Vesuvius, our models clearly show that

763 limestone is not a contaminant in Campi Flegrei (with the possible exception of the Fondi di
764 Baia eruption, see below).

765 Syn-orogenic wedge-top deposits have previously been identified as a potential
766 contaminant of Campi Flegrei magmas, based on their occurrence in the shallow crust within
767 the Neapolitan area (D'Erasmo, 1931; Bernasconi *et al.*, 1981; Sollevanti, 1983). Where large
768 amounts of wedge-top deposits (M_a/M_m = 0.2-0.3) are added to Rhyolite-MELTS AFC models,
769 predicted liquid lines of descent have significantly higher SiO_2 and lower Na_2O, FeO and TiO_2
770 contents than are observed in natural Campi Flegrei glasses, increasing the RMSE relative to
771 simple FC models (Fig. S8, S12, S16). Addition of small amounts of wedge-top deposits leads
772 to K_2O enrichment in the melt at low temperatures as sanidine crystallisation is suppressed.
773 While this mineralogical change is inconsistent with observations of natural samples (which all
774 contain sanidine; Smith *et al.*, 2011) and negates this assimilation source, minor wedge-top
775 deposits contamination lowers the predicted melt Al_2O_3 content compared to FC models which
776 improves the overall fit between the observed and modelled liquid line of descent and reduces
777 the RMSE in all volcano-tectonic groups, especially for very small amounts of contamination
778 (M_a/M_m = 0.05; Fig. 7-9).

779 Long-lived volcanic systems are often thought to be underlain by large volumes of
780 crystalline residue (mush), which fractionated during magmatic evolution but remained in the
781 crust as their accompanying liquids were evacuated during eruptions; in silicic systems, this
782 crystalline restite has a syenitic or granitic composition (Bachmann and Huber, 2016; Cashman
783 *et al.*, 2017; Edmonds *et al.*, 2019; Horn *et al.*, 2022). Campi Flegrei has been active for >300
784 kyr (De Vivo *et al.*, 2001; Rolandi *et al.*, 2003; Di Vito *et al.*, 2008) and the presence of a sub-
785 volcanic crystalline residue is attested by the presence of syenitic lithics, with previous
786 thermodynamic studies suggesting that syenite assimilation impacted the composition of melts
787 erupted during the Campanian Ignimbrite (Fowler *et al.*, 2007). In our models, assimilation of

large proportions of syenite ($M_a/M_m = 0.3$) increases the SiO_2 content of the liquid and reduces the Al_2O_3 concentration (due to greater proportions of feldspar crystallising), improving the correlation between the modelled liquid line of descent and natural glass compositions. The RMSE, averaged across all major elements, is also reduced relative to simple FC models in all volcano-tectonic environments (Fig. S10, S14, S18). However, while predicted liquid lines of descent for syenite-contaminated magmas closely match the compositions of erupted glasses for central caldera and western caldera eruptions, modelled Na_2O concentrations markedly deviate from the observed concentrations at low temperatures for northern/eastern caldera eruptions, predicting much higher Na_2O concentrations than are observed.

Much of central Italy is underlain by Palaeozoic metamorphic basement, predominantly comprising low-grade to granulite-facies metamorphic rocks which formed during the Variscan orogeny (Caggianelli and Prosser, 2001). While the basement depth directly beneath Campi Flegrei remains poorly constrained geophysically and these Palaeozoic rocks have not been intersected in borehole records (AGIP, 1987), seismic datasets reveal relatively shallow basement (≥4 km; Battaglia *et al.*, 2008; Berrino *et al.*, 2008) beneath Campi Flegrei and these have been suggested as potential source of isotopic contamination in Campi Flegrei magmas (Pappalardo *et al.*, 2002). Our models predict quartz saturation at relatively low temperatures with large amounts ($M_a/M_m > 0.2$) of Palaeozoic metapelitic contamination and the absence of quartz in natural Campi Flegrei eruption products (Isaia *et al.*, 2004; Smith *et al.*, 2011) makes this an unlikely assimilation scenario. However, our models do not predict quartz saturation with smaller amounts of Palaeozoic metamorphic contamination ($M_a/M_m < 0.2$) but do produce higher melt SiO_2 contents and lower Al_2O_3 contents than simple fractional crystallisation, improving calculated RMSEs for all volcano-tectonic environments (Fig. S9,13,17). While syenite contamination returns lower RMSEs for central and western caldera eruptions (of 0.11 and 0.21, representing 50% and 45% improvements respectively in the RMSE compared to FC

alone), Palaeozoic metamorphic assimilation generates a lower RMSE overall for northern/eastern caldera eruptions (of 0.12, representing a 17% improvement on FC alone). These more mafic eruptions, from vents along the caldera rim faults, were generally earlier in the last 15 kyr, following the NYT eruption. This suggests earlier eruptions ascended from depth where they encountered the metamorphic basement before erupting along the caldera ring faults, whereas the later eruptions, in the central caldera, stalled in the crust and interacted with residual syenite before eruption.

A summary of best-fit AFC model outputs for each volcano-tectonic group (i.e. lowest RMSE) is shown in Fig. 7-9 and Tables S7-S9. In all volcano-tectonic settings, AFC models can produce liquid lines of descent which are closer to natural glass compositions than simple FC models. However, the nature of the assimilant source and extent of contamination in the best fitting model varies between each group. For northern/eastern caldera eruptions, the best-fit assimilation scenario is the addition of 0.05–0.1 M_a/M_o Palaeozoic metamorphic basement, which improves the fit of the model by ~17% compared to simple FC (Fig 7; Fig. S7–S10). This is consistent with AFC models of isotopic and trace element variations in selected post-15 ka eruptions, which suggest ~1-12% crustal assimilation of Palaeozoic metamorphic basement would explain the observed compositional variations (e.g. Pappalardo *et al.,* 2002; D'Antonio *et al.,* 2007; Iovine *et al.,* 2018). For central caldera eruptions, the best-fit assimilation scenario is addition 0.2-0.3 M_a/M_o syenitic material, which improves the model RMSE by ~49 % relative to FC models (Fig 8; Fig. S11–S14). This is the same for western caldera eruptions; the best-fit assimilation scenario is 0.25-0.3 M_a/M_o of syenite which produces a ~45% improvement compared to simple FC models (Fig 9, Fig. S15–S18). Hence, our results suggest that post-15 kyr eruptions in different volcano-tectonic environments within the Campi Flegrei caldera not only underwent crystallisation under different intensive conditions but also interacted with different types of country rock material, consistent with the magnetotelluric imaging of Isaia *et*

838 *al.* (2025) which suggests a transcrustal magmatic system in contact with basement rock at its
839 margins. Eruptions along the caldera rim faults at the northern and eastern margins of the system
840 were able to "see" and interact with Palaeozoic metamorphic basement at depth, prior to ascent
841 and eruption, whereas eruptions from the centre of the caldera and along regional faults in the
842 west of the caldera were stored within crystalline igneous material, left in the crust as a restitic
843 residue during past eruptions.

844 *Assimilation at Fondi di Baia*

845 The eruption of Baia-Fondi di Baia at the beginning of Epoch 2 (~9.6 ka) was one of the most
846 compositionally distinct events in the last 15 kyr, producing evolved melts from a vent located
847 on a regional fault system on the west side of the caldera (Smith *et al.*, 2011; Pistolesi *et al.*,
848 2017; Vitale and Natale, 2023). While we have categorised it as a western caldera eruption
849 based on its volcano-tectonic setting, the trace element compositions of Baia-Fondi di Baia
850 glasses are distinct from all other post-15 ka Campi Flegrei eruptions, with low Ba and Sr
851 concentrations and high Y, Nb, Nd and Th (Smith *et al.*, 2011). Previous studies have attributed
852 this compositional deviation to mixing between distinct magma batches which had separate
853 AFC evolutionary histories; while Sr-isotopes suggest some amount of limestone
854 contamination, this was ruled out based on the absence of significantly elevated CaO
855 concentrations, with authors instead invoking assimilation of residual magma from the CI
856 (Voloschina *et al.*, 2018). However, our models suggest that, in contrast to other eruptions in
857 the west of the caldera which are best reproduced by assimilation of crystalline restite, the
858 addition of small amounts (0.01 M_a/M_o) of limestone to our best-fit FC model for western
859 caldera eruptions accurately reproduces the major element compositions of Baia-Fondi di Baia
860 glasses, with the fit between the modelled liquid line of descent and natural glass compositions
861 significantly improved for CaO, FeO and TiO_2 (other major oxides do not significantly change;
862 Fig. 10, Fig. S22).

Although carbonate xenoliths have not previously been identified in Campi Flegrei eruption deposits (in contrast with Vesuvius; Fulignati *et al.*, 2000; Del Moro *et al.*, 2001; Gilg *et al.*, 2001), Meso-Cenozoic carbonates have been suggested as a possible lithology underlying the volcano at shallow levels (e.g. Brocchini *et al.*, 2001; Judenherc and Zollo, 2004; Battaglia *et al.*, 2008; Zollo *et al.*, 2008). Since Campi Flegrei caldera has been active for at least 300 kyr (De Vivo *et al.*, 2001), any carbonate would have been progressively removed during the previous eruptions, whereas the younger Vesuvius magmatic system has only been active for the last 39 kyr (Scandone *et al.*, 1991; Brocchini *et al.*, 2001) and is at an earlier stage in its development where an extensive shallow carbonate basement remains. It is possible that the tectonic setting of Baia-Fondi di Baia, on the west of the caldera and situated on regional faults, may have enabled interaction between the magma feeding the eruption and more peripheral carbonate country rocks. Alternatively, hydrothermal calcite has been documented in both Campi Flegrei borehole samples (Chiodini *et al.*, 2015a) and lithic fragments, including tuffaceous lithics recovered from Baia deposits (Buono *et al.*, 2024). While we used an upper Jurassic–lower Cretaceous limestone as the assimilant in our models, sedimentary limestone and hydrothermal calcite would have comparable major element compositions, similarly impacting our modelled AFC liquid lines of descent; hence, we cannot discount this as an alternative Baia-Fondi di Baia assimilant source.

Volcano-tectonic controls on eruptive processes

Alongside compositional information, Rhyolite-MELTS outputs predicted physical properties for evolving magmas (e.g. density, viscosity) as well as information on the behaviour of magmatic volatiles; these properties vary between our best-fit models for each of our three volcano-tectonic groups (Fig. 11). H_2O behaves incompatibly, consistently increasing in concentration within the melt phase as the magma cools, but with a greater enrichment per unit temperature below the invariant point (temperature at which melt fraction drops and physical

properties change over a short interval), likely due to enhanced crystallisation of anhydrous minerals (Fig. 11a). The volume fraction of exsolved H_2O coexisting with the magma increases dramatically around the invariant point for all tectonic settings, from ~10 vol% below to ~60 vol% above this temperature (Fig. 11b). This is consistent with other studies at Campi Flegrei (Fowler *et al.*, 2007; Cannatelli, 2012; Stock *et al.*, 2016) and elsewhere (e.g. Mount St. Helens, USA – Kent *et al.,* 2007; Calbuco, Chile – Arzilli *et al.,* 2019) which suggest that the dramatic increase in volatile content at low temperatures could trigger explosive eruptions. Stock *et al.* (2016) used the volatile content of apatite crystals and melt inclusions in Astroni 1 deposits to demonstrate the magma reservoir beneath Campi Flegrei remained volatile undersaturated until low temperatures, with volatile saturation likely triggering eruption on very short pre-eruptive timescales, perhaps days to months. Forni *et al.* (2018) suggest Monte Nuovo may also have been triggered by volatile saturation which occurred in the decades before the eruption.

H_2O saturation controls the viscosity and density evolution in our best-fit models (Fig. 11c, d). The large increase in melt H_2O content below the invariant point leads to a rapid drop in both viscosity and density across all tectonic settings, consistent with the results of Fowler *et al*. (2007) and Cannatelli (2012). The inflection in viscosity from an initial increase as magma cools and becomes more SiO_2 rich to a rapid decrease as dissolved melt H_2O concentration increases occurs at slightly higher temperatures and higher maximum viscosities for northern/eastern caldera eruptions (830°C) than western caldera or central caldera eruptions (815-820°C; Fig. 11a), reflecting small temperature differences in the invariant point. Our models show that, despite small differences in the temperatures at which viscosity and density change dramatically, the increase in volume fraction of exsolved H_2O occurs late in magmatic evolution, at similar temperatures for all tectonic groups. While it remains possible that some eruptions were triggered externally (e.g. by recharge), our models validate the potential for

912 eruption triggering by low temperature volatile saturation in all volcano-tectonic groups,
913 despite differences in their pre-eruptive history (e.g. assimilation processes).

914 **CONCLUSIONS**

915 We have shown that Rhyolite-MELTS modelling can be used to evaluate a wide range of
916 potential magma storage conditions, determining which (if any) can produce observed phase
917 compositions by fractional crystallisation. Building on the statistical test proposed by Gleeson
918 *et al.*, (2017) to quantitatively evaluate which model best reproduces natural samples, we show
919 that magma storage before eruptions of Campi Flegrei in the last 15 kyr was most likely at
920 pressures of 110 to 160 MPa (corresponding to depths of ~5-7 km), with a parental magma with
921 L_{H2O} of 2 – 3 wt% and an L_{fO2} near the QFM buffer (QFM to QFM+1). Eruptions from vents in
922 the centre of the caldera likely had higher melt H_2O contents (3 wt%) compared to those erupted
923 at vents along caldera rim faults or regional faults in the west of the caldera (2 wt%), possibly
924 due to interaction with crustal fluids.

925 We find that isobaric fractional crystallisation of a parental magma cannot fully
926 reproduce the liquid line of descent recorded by natural samples under any realistic conditions.
927 Instead, addition of a small amount of assimilant improves the fit of the models compared to
928 observed compositions. For eruptions from vents along caldera ring faults in the east of the
929 Campi Flegrei system, addition of 5–10 % of metamorphic Palaeozoic basement leads to the
930 biggest improvement in model fit compared to FC alone. For vents in the centre of the caldera
931 and along regional faults in the west, addition of 30% syenite is the best-fit assimilation
932 scenario. Our results indicate that the magmatic evolution of an eruption, in terms of storage
933 and assimilation, correlates with the volcano-tectonic setting of its eruption vent. Central
934 caldera eruptions were likely evolved within the crystalline syenitic remnants of previous
935 eruptions, whereas those on the periphery of the caldera system ascended from depth along
936 faults in contact with the surrounding metamorphic basement. As assimilation influences the

compositional evolution of the magmas, which in turn impacts the magma's physical properties and the eruptive style, the vent location (in terms of the volcano-tectonic setting) needs to be considered in hazard forecasting.

ACKNOWLEDGMENTS

This research forms part of a PhD project of F.M.A funded by a Trinity College Dublin Provost's Award. Funding from a Trinity Trust Travel Grant awarded to F.M.A is acknowledged for fieldwork. F.M.A., M.J.S., V.C.S., R.I., S.V. and J.N. acknowledge funding from the INGV INSIDE OUT project and XRF data collection was supported by the Geological Survey Ireland-funded Earth Surface Research Laboratory in Trinity College Dublin. We thank Silvio Mollo, Samantha Tramontano and an anonymous reviewer for providing constructive feedback on the manuscript.

DATA AVAILABILITY STATEMENT

New geochemical data presented in this study have been deposited in EarthChem Library (doi:10.60520/IEDA/113525) and in the online supplementary material. Rhyolite-MELTS data underlying the study are available in the online supplementary material. A Python code to calculate RMSE between Rhyolite-MELTS outputs and natural glass data is available on GitHub at doi:10.5281/zenodo.14900107.

REFERENCES

Acocella, V. (2010). Evaluating fracture patterns within a resurgent caldera: Campi Flegrei, Italy. *Bulletin of Volcanology* **72**, 623–638.

Agip (1987). Geologia e geofisica del sistema geotermico dei Campi Flegrei. *Technical report Settore Esplor* 1–23.

959 Albert, P. *et al.* (2019). Evidence for a large-magnitude eruption from Campi Flegrei caldera
960 (Italy) at 29 ka. *Geology* **47**, 595–599.

961 Amoruso, A., Crescentini, L., Sabbetta, I., De Martino, P., Obrizzo, F. & Tammaro, U. (2014).
962 Clues to the cause of the 2011–2013 Campi Flegrei caldera unrest, Italy, from
963 continuous GPS data. *Geophysical Research Letters* **41**, 3081–3088.

964 Anderson, A. T., Newman, S., Williams, S. N., Druitt, T. H., Skirius, C. & Stolper, E. (1989).
965 H2O, C02, CI, and gas in Plinian and ash-flow Bishop rhyolite. *Geology* **17**, 221–225.

966 Anenburg, M. & O'Neill, H. St C. (2019). Redox in Magmas: Comment on a Recent
967 Treatment of the Kaiserstuhl Volcanics (Braunger et al., Journal of Petrology, 59,
968 1731–1762, 2018) and Some Other Misconceptions. *Journal of Petrology* **60,** 1825-
969 1832

970 Annen, C., Blundy, J. D., Leuthold, J. & Sparks, R. S. J. (2015). Construction and evolution
971 of igneous bodies: Towards an integrated perspective of crustal magmatism. *Lithos*
972 **230**, 206–221

973 Antoshechkina, P. M. & Ghiorso, M. S. (2018). MELTS for MATLAB: A new educational
974 and research tool for computational thermodynamics. *AGU Fall Meeting Abstracts*,
975 ED44B-23.

976 Arienzo, I., Heumann, A., Wörner, G., Civetta, L. & Orsi, G. (2011). Processes and timescales
977 of magma evolution prior to the Campanian Ignimbrite eruption (Campi Flegrei,
978 Italy). *Earth and Planetary Science Letters* **306**, 217–228.

979 Arienzo, I., Mazzeo, F. C., Moretti, R., Cavallo, A. & D'Antonio, M. (2016). Open-system
980 magma evolution and fluid transfer at Campi Flegrei caldera (Southern Italy) during

981 the past 5ka as revealed by geochemical and isotopic data: The example of the Nisida
982 eruption. *Chemical Geology* **427**, 109–124.

983 Arienzo, I., Moretti, R., Civetta, L., Orsi, G. & Papale, P. (2010). The feeding system of
984 Agnano–Monte Spina eruption (Campi Flegrei, Italy): Dragging the past into present
985 activity and future scenarios. *Chemical Geology* **270**, 135–147.

986 Arzilli, F. *et al.* (2019). The unexpected explosive sub-Plinian eruption of Calbuco volcano
987 (22–23 April 2015; southern Chile): Triggering mechanism implications. *Journal of*
988 *Volcanology and Geothermal Research*. Elsevier **378**, 35–50.

989 Astbury, R. L., Petrelli, M., Ubide, T., Stock, M. J., Arienzo, I., D'Antonio, M. & Perugini, D.
990 (2018). Tracking plumbing system dynamics at the Campi Flegrei caldera, Italy: High-
991 resolution trace element mapping of the Astroni crystal cargo. *Lithos* **318**, 464–477.

992 Bachmann, O. & Huber, C. (2016). Silicic magma reservoirs in the Earth's crust. *American*
993 *Mineralogist*. Mineralogical Society of America **101**, 2377–2404.

994 Balcone-Boissard, H., Boudon, G., Zdanowicz, G., Orsi, G., Webster, J. D., Civetta, L.,
995 D'Antonio, M. & Arienzo, I. (2024). The space-time architecture variation of the
996 shallow magmatic plumbing systems feeding the Campi Flegrei and Ischia volcanoes
997 (Southern Italy) from halogen constraints. *American Mineralogist* **109**, 977–991.

998 Battaglia, J., Zollo, A., Virieux, J. & Iacono, D. D. (2008). Merging active and passive data
999 sets in traveltime tomography: the case study of Campi Flegrei caldera (Southern
1000 Italy). *Geophysical Prospecting* **56**, 555–573.

1001 Bernasconi, A., Bruni, P., Gorla, L., Principe, C. & Sbrana, A. (1981). Risultati preliminari
1002 dell'esplorazione geotermica profonda nell'area vulcanica del Somma-Vesuvio.
1003 *Rendiconti Della Societa Geologica Italiana* **4**, 237–240.

1004 Berrino, G., Corrado, G. & Riccardi, U. (2008). Sea gravity data in the Gulf of Naples. A
1005 contribution to delineating the structural pattern of the Phlegraean Volcanic District.
1006 *Journal of Volcanology and Geothermal Research* **175**, 241–252.

1007 Bevilacqua, A. *et al.* (2015). Quantifying volcanic hazard at Campi Flegrei caldera (Italy)
1008 with uncertainty assessment: 1. Vent opening maps. *Journal of Geophysical Research:*
1009 *Solid Earth*. Wiley Online Library **120**, 2309–2329.

1010 Bevilacqua, A., Flandoli, F., Neri, A., Isaia, R. & Vitale, S. (2016). Temporal models for the
1011 episodic volcanism of Campi Flegrei caldera (Italy) with uncertainty quantification.
1012 *Journal of Geophysical Research: Solid Earth* **121**, 7821–7845.

1013 Bevilacqua, A., Neri, A., Bisson, M., Esposti Ongaro, T., Flandoli, F., Isaia, R., Rosi, M. &
1014 Vitale, S. (2017). The Effects of Vent Location, Event Scale, and Time Forecasts on
1015 Pyroclastic Density Current Hazard Maps at Campi Flegrei Caldera (Italy). *Frontiers*
1016 *in Earth Science* **5**.

1017 Bianco, F., Capuano, P., Del Pezzo, E., De Siena, L., Maercklin, N., Russo, G., Vassallo, M.,
1018 Virieux, J. & Zollo, A. (2022). Seismic and Gravity Structure of the Campi Flegrei
1019 Caldera, Italy. In: Orsi, G., D'Antonio, M. & Civetta, L. (eds) *Campi Flegrei: A*
1020 *Restless Caldera in a Densely Populated Area*. Berlin, Heidelberg: Springer, 55–94.

1021 Blundy, J. & Cashman, K. (2008). Petrologic reconstruction of magmatic system variables
1022 and processes. *Reviews in Mineralogy and Geochemistry* **69**, 179–239.

1023 Bohrson, W. A., Spera, F. J., Fowler, S. J., Belkin, H. E., De Vivo, B. & Rolandi, G. (2006).
1024 Petrogenesis of the Campanian Ignimbrite: Implications for crystal-melt separation
1025 and open-system processes from major and trace elements and Th isotopic data.
1026 *Developments in Volcanology*. Elsevier, 249–288.

1027 Boschetty, F. O., Ferguson, D. J., Cortés, J. A., Morgado, E., Ebmeier, S. K., Morgan, D. J.,
1028 Romero, J. E. & Silva Parejas, C. (2022). Insights Into Magma Storage Beneath a
1029 Frequently Erupting Arc Volcano (Villarrica, Chile) From Unsupervised Machine
1030 Learning Analysis of Mineral Compositions. *Geochemistry, Geophysics, Geosystems*
1031 **23**, e2022GC010333.

1032 Brocchini, D., Principe, C., Castradori, D., Laurenzi, M. A. & Gorla, L. (2001). Quaternary
1033 evolution of the southern sector of the Campanian Plain and early Somma-Vesuvius
1034 activity: insights from the Trecase 1 well. *Mineralogy and Petrology* **73**, 67–91.

1035 Buono, G., Caliro, S., Pappalardo, L. & Chiodini, G. (2024). Hydrothermal calcite formation
1036 in Campi Flegrei caldera, Italy: unraveling carbon sink processes in alkaline volcanic
1037 systems. *Scientific Reports*. Nature Publishing Group **14**, 16839.

1038 Caggianelli, A. & Prosser, A. (2001). An exposed cross-section of late Hercynian upper and
1039 intermediate continental crust in the Sila nappe (Calabria, southern Italy). *Periodico di*
1040 *Mineralogia* **70**, 277–301.

1041 Calò, M. & Tramelli, A. (2018). Anatomy of the Campi Flegrei caldera using enhanced
1042 seismic tomography models. *Scientific reports* **8**, 1–12.

1043 Cannatelli, C. (2012). Understanding magma evolution at Campi Flegrei (Campania, Italy)
1044 volcanic complex using melt inclusions and phase equilibria. *Mineralogy and*
1045 *Petrology* **104**, 29–42.

1046 Cannatelli, C., Doherty, A. L., Esposito, R., Lima, A. & De Vivo, B. (2016). Understanding a
1047 volcano through a droplet: A melt inclusion approach. *Journal of Geochemical*
1048 *Exploration* **171**, 4–19.

1049 Cannatelli, C., Lima, A., Bodnar, R., De Vivo, B., Webster, J. & Fedele, L. (2007).
1050 Geochemistry of melt inclusions from the Fondo Riccio and Minopoli 1 eruptions at
1051 Campi Flegrei (Italy). *Chemical Geology* **237**, 418–432.

1052 Carracedo, J. C., Badiola, E. R., Guillou, H., Paterne, M., Scaillet, S., Torrado, F. J. P., Paris,
1053 R., Fra-Paleo, U. & Hansen, A. (2007). Eruptive and structural history of Teide
1054 Volcano and rift zones of Tenerife, Canary Islands. *Geological Society of America*
1055 *Bulletin* **119**, 1027–1051.

1056 Carter, E. J., Stock, M. J., Beresford-Browne, A., Cooper, M. R., Raine, R. & Fereyrolles, A.
1057 (2024). Volcanic tempo driven by rapid fluctuations in mantle temperature during
1058 large igneous province emplacement. *Earth and Planetary Science Letters* **644**,
1059 118903.

1060 Cashman, K. V., Sparks, R. S. J. & Blundy, J. D. (2017). Vertically extensive and unstable
1061 magmatic systems: a unified view of igneous processes. *Science* **355**.

1062 Cassidy, M., Manga, M., Cashman, K. & Bachmann, O. (2018). Controls on explosive-
1063 effusive volcanic eruption styles. *Nature Communications*. Nature Publishing Group **9**,
1064 2839.

1065 Chiodini, G., Caliro, S., De Martino, P., Avino, R. & Gherardi, F. (2012). Early signals of new
1066 volcanic unrest at Campi Flegrei caldera? Insights from geochemical data and physical
1067 simulations. *Geology* **40**, 943–946.

1068 Chiodini, G., Pappalardo, L., Aiuppa, A. & Caliro, S. (2015a). The geological CO2 degassing
1069 history of a long-lived caldera. *Geology* **43**, 767–770.

1070 Chiodini, G., Vandemeulebrouck, J., Caliro, S., D'Auria, L., De Martino, P., Mangiacapra, A.
1071 & Petrillo, Z. (2015b). Evidence of thermal-driven processes triggering the 2005–2014
1072 unrest at Campi Flegrei caldera. *Earth and Planetary Science Letters* **414**, 58–67.

1073 Ciarcia, S. & Vitale, S. (2025). Orogenic evolution of the northern Calabria–southern
1074 Apennines system in the framework of the Alpine chains in the central-western
1075 Mediterranean area. *Geological Society of America Bulletin* **137**, 1143–1176.

1076
1077 Civetta, L., Carluccio, E., Innocenti, F., Sbrana, A. & Taddeucci, G. (1991). Magma chamber
1078 evolution under the Phlegraean Fields during the last 10 ka: trace element and isotope
1079 data. *European Journal of Mineralogy* 415–428.

1080 Cole, J., Milner, D. & Spinks, K. (2005). Calderas and caldera structures: a review. *Earth-*
1081 *Science Reviews* **69**, 1–26.

1082 D'Antonio, M. (2011). Lithology of the basement underlying the Campi Flegrei caldera:
1083 Volcanological and petrological constraints. *Journal of Volcanology and Geothermal*
1084 *Research* **200**, 91–98.

1085 D'Antonio, M., Civetta, L., Orsi, G., Pappalardo, L., Piochi, M., Carandente, A., De Vita, S.,
1086 Di Vito, M. & Isaia, R. (1999). The present state of the magmatic system of the Campi
1087 Flegrei caldera based on a reconstruction of its behavior in the past 12 ka. *Journal of*
1088 *Volcanology and Geothermal Research* **91**, 247–268.

1089 D'Antonio, M., Tonarini, S., Arienzo, I., Civetta, L. & Di Renzo, V. (2007). Components and
1090 processes in the magma genesis of the Phlegrean Volcanic District, southern Italy.
1091 *Special Papers-Geological Society of America* **418**, 203.

1092 Danyushevsky, L. V., McNeill, A. W. & Sobolev, A. V. (2002). Experimental and petrological
1093 studies of melt inclusions in phenocrysts from mantle-derived magmas: an overview
1094 of techniques, advantages and complications. *Chemical Geology* **183**, 5–24.

1095 D'Auria, L. *et al.* (2015). Magma injection beneath the urban area of Naples: a new
1096 mechanism for the 2012–2013 volcanic unrest at Campi Flegrei caldera. *Scientific*
1097 *Reports*. Nature Publishing Group **5**, 13100.

1098 De Siena, L., Del Pezzo, E. & Bianco, F. (2010). Seismic attenuation imaging of Campi
1099 Flegrei: Evidence of gas reservoirs, hydrothermal basins, and feeding systems.
1100 *Journal of Geophysical Research: Solid Earth* **115**.

1101 de Vita, S. *et al.* (1999). The Agnano–Monte Spina eruption (4100 years BP) in the restless
1102 Campi Flegrei caldera (Italy). *Journal of Volcanology and Geothermal Research* **91**,
1103 269–301.

1104 De Vivo, B., Rolandi, G., Gans, P., Calvert, A., Bohrson, W. A., Spera, F. & Belkin, H. (2001).
1105 New constraints on the pyroclastic eruptive history of the Campanian volcanic Plain
1106 (Italy). *Mineralogy and Petrology* **73**, 47–65.

1107 Deino, A. L., Orsi, G., de Vita, S. & Piochi, M. (2004). The age of the Neapolitan Yellow Tuff
1108 caldera-forming eruption (Campi Flegrei caldera–Italy) assessed by 40Ar/39Ar dating
1109 method. *Journal of Volcanology and Geothermal Research* **133**, 157–170.

1110 Del Moro, A., Fulignati, P., Marianelli, P. & Sbrana, A. (2001). Magma contamination by
1111 direct wall rock interaction: constraints from xenoliths from the walls of a carbonate-
1112 hosted magma chamber (Vesuvius 1944 eruption). *Journal of Volcanology and*
1113 *Geothermal Research* **112**, 15–24.

1114 D'Erasmo, G. (1931). *Studio geologico dei pozzi profondi della Campania*. Jovene.

1115 Di Fiore, F., Mollo, S., Vona, A., MacDonald, A., Ubide, T., Nazzari, M., Romano, C. &
1116 Scarlato, P. (2021). Kinetic partitioning of major and trace cations between
1117 clinopyroxene and phonotephritic melt under convective stirring conditions: New
1118 insights into clinopyroxene sector zoning and concentric zoning. *Chemical Geology*
1119 **584**, 120531.

1120 Di Girolamo, P., Ghiara, M. R., Lirer, Munno, R., Rolandi, G. & Stanzione, D. (1984).
1121 Vulcanologia e petrologia dei Campi Flegreei. *Italian Journal of Geosciences* **103**,
1122 349–413.

1123 Di Renzo, V., Arienzo, I., Civetta, L., D'Antonio, M., Tonarini, S., Di Vito, M. & Orsi, G.
1124 (2011). The magmatic feeding system of the Campi Flegrei caldera: architecture and
1125 temporal evolution. *Chemical Geology* **281**, 227–241.

1126 Di Vito, M., Isaia, R., Orsi, G., Southon, J. d, De Vita, S., d'Antonio, M., Pappalardo, L. &
1127 Piochi, M. (1999). Volcanism and deformation since 12,000 years at the Campi Flegrei
1128 caldera (Italy). *Journal of Volcanology and Geothermal Research* **91**, 221–246.

1129 Di Vito, M., Sulpizio, R., Zanchetta, G. & D'Orazio, M. (2008). The late Pleistocene
1130 pyroclastic deposits of the Campanian Plain: new insights into the explosive activity
1131 of Neapolitan volcanoes. *Journal of Volcanology and Geothermal Research* **177**, 19–
1132 48.

1133 Edmonds, M., Cashman, K. V., Holness, M. & Jackson, M. (2019). Architecture and dynamics
1134 of magma reservoirs. The Royal Society Publishing **377**, 20180298.

1135 Eggler, D. H. (1972). Water-saturated and undersaturated melting relations in a Paricutin
1136 andesite and an estimate of water content in the natural magma. *Contributions to*
1137 *Mineralogy and Petrology* **34**, 261–271.

1138 Faccenna, C., Funiciello, F., Civetta, L., D'Antonio, M., Moroni, M. & Piromallo, C. (2007).
1139 Slab disruption, mantle circulation, and the opening of the Tyrrhenian basins. In:
1140 Beccaluva, L., Bianchini, G. & Wilson, M. (eds) *Cenozoic Volcanism in the*
1141 *Mediterranean Area*. Geological Society of America, 153–169.

1142 Fedele, L., Scarpati, C., Lanphere, M., Melluso, L., Morra, V., Perrotta, A. & Ricci, G. (2008).
1143 The Breccia Museo formation, Campi Flegrei, southern Italy: geochronology,
1144 chemostratigraphy and relationship with the Campanian Ignimbrite eruption. *Bulletin*
1145 *of Volcanology* **70**, 1189–1219.

1146 Fedele, L., Tarzia, M., Belkin, H. E., De Vivo, B., Lima, A. & Lowenstern, J. B. (2006).
1147 Magmatic-hydrothermal fluid interaction and mineralization in alkali-syenite nodules
1148 from the Breccia Museo pyroclastic deposit, Naples, Italy. *Developments in*
1149 *Volcanology*. Elsevier, 125–161.

1150 Feig, S. T., Koepke, J. & Snow, J. E. (2010). Effect of oxygen fugacity and water on phase
1151 equilibria of a hydrous tholeiitic basalt. *Contributions to Mineralogy and Petrology*
1152 **160**, 551–568.

1153 Fernandez, G. *et al.* (2024). New constraints on the Middle-Late Pleistocene Campi Flegrei
1154 explosive activity and Mediterranean tephrostratigraphy (~160 ka and 110–90 ka).
1155 *Quaternary Science Reviews* **331**, 108623.

1156 Ferrucci, F., Gaudiosi, G., Pino, N. A., Luongo, G., Hirn, A. & Mirabile, L. (1989). Seismic
1157 detection of a major moho upheaval beneath the Campania volcanic area (Naples,
1158 southern Italy). *Geophysical Research Letters* **16**, 1317–1320.

1159 Filice, F., Liberi, F., Cirillo, D., Pandolfi, L., Marroni, M. & Piluso, E. (2015). Geology map
1160 of the central area of Catena Costiera: insights into the tectono-metamorphic evolution
1161 of the Alpine belt in Northern Calabria. *Journal of Maps*. Taylor & Francis **11**, 114–
1162 125.

1163 Fisk, M. R. & Bence, A. E. (1980). Experimental crystallization of chrome spinel in
1164 FAMOUS basalt 527-1-1. *Earth and Planetary Science Letters* **48**, 111–123.

1165 Forni, F., Bachmann, O., Mollo, S., De Astis, G., Gelman, S. E. & Ellis, B. S. (2016). The
1166 origin of a zoned ignimbrite: Insights into the Campanian Ignimbrite magma chamber
1167 (Campi Flegrei, Italy). *Earth and Planetary Science Letters* **449**, 259–271.

1168 Forni, F., Degruyter, W., Bachmann, O., De Astis, G. & Mollo, S. (2018). Long-term
1169 magmatic evolution reveals the beginning of a new caldera cycle at Campi Flegrei.
1170 *Science Advances* **4**, eaat9401.

1171 Fourmentraux, C., Métrich, N., Bertagnini, A. & Rosi, M. (2012). Crystal fractionation,
1172 magma step ascent, and syn-eruptive mingling: the Averno 2 eruption (Phlegraean
1173 Fields, Italy). *Contributions to Mineralogy and Petrology* **163**, 1121–1137.

1174 Fowler, S. J. & Spera, F. J. (2010). A metamodel for crustal magmatism: phase equilibria of
1175 giant ignimbrites. *Journal of Petrology* **51**, 1783–1830.

1176 Fowler, S. J., Spera, F. J., Bohrson, W. A., Belkin, H. E. & De Vivo, B. (2007). Phase
1177 equilibria constraints on the chemical and physical evolution of the Campanian
1178 Ignimbrite. *Journal of Petrology* **48**, 459–493.

1179 Fred, R., Heinonen, J. S., Heinonen, A. & Bohrson, W. A. (2022). Thermodynamic constraints
1180 on the petrogenesis of massif-type anorthosites and their parental magmas. *Lithos*
1181 **422–423**, 106751.

1182 Frost, B. R. (1991). Introduction to oxygen fugacity and its petrologic importance. *Reviews in*
1183 *Mineralogy and Geochemistry*. Mineralogical Society of America **25**, 1–9.

1184 Fulignati, P., Marianelli, P., Santacroce, R. & Sbrana, A. (2000). The skarn shell of the 1944
1185 Vesuvius magma chamber. Genesis and P-T-X conditions from melt and fluid
1186 inclusion data. *European Journal of Mineralogy* **12**, 1025–1039.

1187 Gaetani, G. A., Grove, T. L. & Bryan, W. B. (1993). The influence of water on the
1188 petrogenesis of subductionrelated igneous rocks. *Nature* **365**, 332–334.

1189 Gainsforth, Z. et al. (2015). Constraints on the formation environment of two chondrule-like
1190 igneous particles from comet 81P/Wild 2. *Meteoritics & Planetary Science* **50**, 976–
1191 1004.

1192 Gardner, J. E., Befus, K. S., Gualda, G. A. & Ghiorso, M. S. (2014). Experimental constraints
1193 on rhyolite-MELTS and the Late Bishop Tuff magma body. *Contributions to*
1194 *Mineralogy and Petrology* **168**, 1–14.

1195 Gebauer, S. K., Schmitt, A. K., Pappalardo, L., Stockli, D. F. & Lovera, O. M. (2014).
1196 Crystallization and eruption ages of Breccia Museo (Campi Flegrei caldera, Italy)
1197 plutonic clasts and their relation to the Campanian ignimbrite. *Contributions to*
1198 *Mineralogy and Petrology*. Springer **167**, 1–18.

1199 Ghiorso, M. S. & Gualda, G. A. (2015). An H 2 O–CO 2 mixed fluid saturation model
1200 compatible with rhyolite-MELTS. *Contributions to Mineralogy and Petrology* **169**, 1–
1201 30.

1202 Ghiorso, M. S. & Kelemen, P. B. (1987). Evaluating reaction stoichiometry in magmatic
1203 systems evolving under generalized thermodynamic constraints: examples comparing
1204 isothermal and isenthalpic assimilation. *Magmatic Processes: Physicochemical*
1205 *Principles*. Geochem. Soc. State College, Pa. **1**, 319–336.

1206 Ghiorso, M. S. & Sack, R.O. (1995). Chemical mass transfer in magmatic processes IV. A
1207 revised and internally consistent thermodynamic model for the interpolation and
1208 extrapolation of liquid-solid equilibria in magmatic systems at elevated temperatures
1209 and pressures. *Contributions to Mineralogy and Petrology* **199,** 197-212.

1210
1211 Giaccio, B., Hajdas, I., Isaia, R., Deino, A. & Nomade, S. (2017). High-precision 14 C and 40
1212 Ar/39 Ar dating of the Campanian Ignimbrite (Y-5) reconciles the time-scales of
1213 climatic-cultural processes at 40 ka. *Scientific Reports* **7**, 1–10.

1214 Giacomuzzi, G., Chiarabba, C., Bianco, F., De Gori, P. & Agostinetti, N. P. (2024). Tracking
1215 transient changes in the plumbing system at Campi Flegrei Caldera. *Earth and*
1216 *Planetary Science Letters* **637**, 118744.

1217 Gibson, S. A., Geist, D. G., Day, J. A. & Dale, C. W. (2012). Short wavelength heterogeneity
1218 in the Galápagos plume: Evidence from compositionally diverse basalts on Isla
1219 Santiago. *Geochemistry, Geophysics, Geosystems* **13**.

1220 Gilg, H. A., Lima, A., Somma, R., Belkin, H. E. & Ayuso, R. A. (2001). Isotope geochemistry
1221 and fluid inclusion study of skarns from Vesuvius. *Mineralogy and Petrology* **73**, 145–
1222 176.

Giordano, G. & Caricchi, L. (2022). Determining the State of Activity of Transcrustal Magmatic Systems and Their Volcanoes. *Annual Review of Earth and Planetary Sciences* **50**, 231–259.

Gleeson, M.L., Antoshechkina, P.M., Wieser, P.E. (2023). pyMELTScalc - a Python3 package for fast, easy, and flexible MELTS calculations. *AGU Fall Meeting Abstracts,* V53A-05.

Gleeson, M. L., Stock, M. J., Pyle, D. M., Mather, T. A., Hutchison, W., Yirgu, G. & Wade, J. (2017). Constraining magma storage conditions at a restless volcano in the Main Ethiopian Rift using phase equilibria models. *Journal of Volcanology and Geothermal Research* **337**, 44–61.

Graessner, T. & Schenk, V. (2001). An Exposed Hercynian Deep Crustal Section in the Sila Massif of Northern Calabria: Mineral Chemistry, Petrology and a P-T Path of Granulite-facies Metapelitic Migmatites and Metabasites. *Journal of Petrology* **42**, 931–961.

Gualda, G. A. R., Ghiorso, M. S., Lemons, R. V. & Carley, T. L. (2012). Rhyolite-MELTS: a Modified Calibration of MELTS Optimized for Silica-rich, Fluid-bearing Magmatic Systems. *Journal of Petrology* **53**, 875–890.

Higgins, O. & Stock, M. J. (2024). A New Calibration of the OPAM Thermobarometer for Anhydrous and Hydrous Mafic Systems. *Journal of Petrology* **65**, egae043.

Hill, R. & Roeder, P. (1974). The Crystallization of Spinel from Basaltic Liquid as a Function of Oxygen Fugacity. *The Journal of Geology* **82**, 709–729.

Horn, E. L., Taylor, R. N., Gernon, T. M., Stock, M. J. & Farley, E. M. R. (2022). Composition and Petrology of a Mush-Bearing Magma Reservoir beneath Tenerife. *Journal of Petrology* **63**, egac095.

Iacono Marziano, G., Gaillard, F. & Pichavant, M. (2008). Limestone assimilation by basaltic magmas: an experimental re-assessment and application to Italian volcanoes. *Contributions to Mineralogy and Petrology* **155**, 719–738.

Isaia, R., D'Antonio, M., Dell'Erba, F., Di Vito, M. & Orsi, G. (2004). The Astroni volcano: the only example of closely spaced eruptions in the same vent area during the recent history of the Campi Flegrei caldera (Italy). *Journal of Volcanology and Geothermal Research* **133**, 171–192.

Isaia, R., Marianelli, P. & Sbrana, A. (2009). Caldera unrest prior to intense volcanism in Campi Flegrei (Italy) at 4.0 ka BP: Implications for caldera dynamics and future eruptive scenarios. *Geophysical Research Letters* **36**.

Isaia, R., Troiano, A., Di Giuseppe, M. G., De Paola, C., Gottsmann, J., Pagliara, F., Smith, V. C. & Stock, M. J. (2025). 3D magnetotelluric imaging of a transcrustal magma system beneath the Campi Flegrei caldera, southern Italy. *Communications Earth & Environment*. Nature Publishing Group **6**, 1–16.

Isaia, R., Vitale, S., Marturano, A., Aiello, G., Barra, D., Ciarcia, S., Iannuzzi, E. & Tramparulo, F. D. (2019). High-resolution geological investigations to reconstruct the long-term ground movements in the last 15 kyr at Campi Flegrei caldera (southern Italy). *Journal of Volcanology and Geothermal Research* **385**, 143–158.

James, D. E. (1981). The combined use of oxygen and radiogenic isotopes as indicators of crustal contamination. *Annual Review of Earth and Planetary Sciences* **9**, 311–344.

1268 Jochum, K. P. *et al.* (2006). MPI-DING reference glasses for in situ microanalysis: New
1269 reference values for element concentrations and isotope ratios. *Geochemistry,*
1270 *Geophysics, Geosystems* **7**.

1271 Judenherc, S. & Zollo, A. (2004). The Bay of Naples (southern Italy): Constraints on the
1272 volcanic structures inferred from a dense seismic survey. *Journal of Geophysical*
1273 *Research: Solid Earth* **109**.

1274 Kelemen, P., Yogodzinski, G. & Scholl, D. W. (2003). Along-strike variation in lavas of the
1275 Aleutian island arc: Implications for the genesis of high-Mg# andesite and the
1276 continental crust. *American Geophysical Union. Geophysical Monograph* **138**, 223–
1277 274.

1278 Kent, A. J., Blundy, J., Cashman, K. V., Cooper, K. M., Donnelly, C., Pallister, J. S., Reagan,
1279 M., Rowe, M. C. & Thornber, C. R. (2007). Vapor transfer prior to the October 2004
1280 eruption of Mount St. Helens, Washington. *Geology*. Geological Society of America
1281 **35**, 231–234.

1282 Knafelc, J., Bryan, S. E., Gust, D. & Cathey, H. E. (2020). Defining Pre-eruptive Conditions
1283 of the Havre 2012 Submarine Rhyolite Eruption Using Crystal Archives. *Frontiers in*
1284 *Earth Science*. Frontiers **8**.

1285 Kress, V. C. & Ghiorso, M. S. (2004). Thermodynamic modeling of post-entrapment
1286 crystallization in igneous phases. *Journal of Volcanology and Geothermal Research*
1287 **137**, 247–260.

1288 Landi, P., Métrich, N., Bertagnini, A., Rosi, M. (2004). Landi, Patrizia, et al. "Dynamics of
1289 magma mixing and degassing recorded in plagioclase at Stromboli (Aeolian
1290 Archipelago, Italy). *Contributions to Mineralogy and Petrology* **147**, 213-227.

1291 Lange, R. A., Frey, H. M. & Hector, J. (2009). A thermodynamic model for the plagioclase-
1292 liquid hygrometer/thermometer. *American Mineralogist* **94**, 494–506.

1293 Lipman, P. W. (1984). The roots of ash flow calderas in western North America: windows into
1294 the tops of granitic batholiths. *Journal of Geophysical Research: Solid Earth* **89,** 8801-
1295 8841

1296 Lowenstern, J. (1995). Applications of silicate melt inclusions to the study of magmatic
1297 volatiles. *Chem. Geol.* **183**, 5–24.

1298 Mangiacapra, A., Moretti, R., Rutherford, M., Civetta, L., Orsi, G. & Papale, P. (2008). The
1299 deep magmatic system of the Campi Flegrei caldera (Italy). *Geophysical Research*
1300 *Letters* **35**.

1301 Masotta, M., Mollo, S., Freda, C., Gaeta, M. & Moore, G. (2013). Clinopyroxene–liquid
1302 thermometers and barometers specific to alkaline differentiated magmas.
1303 *Contributions to Mineralogy and Petrology* **166**, 1545–1561.

1304 Mazzeo, F. C., D'Antonio, M., Arienzo, I., Aulinas, M., Di Renzo, V. & Gimeno, D. (2014).
1305 Subduction-related enrichment of the Neapolitan volcanoes (Southern Italy) mantle
1306 source: New constraints on the characteristics of the slab-derived components.
1307 *Chemical Geology* **386**, 165–183.

1308 Natale, J., Camanni, G., Ferranti, L., Isaia, R., Sacchi, M., Spiess, V., Steinmann, L. & Vitale,
1309 S. (2022a). Fault systems in the offshore sector of the Campi Flegrei caldera (southern
1310 Italy): Implications for nested caldera structure, resurgent dome, and volcano-tectonic
1311 evolution. *Journal of Structural Geology* **163**, 104723.

1312 Natale, J., Ferranti, L., Isaia, R., Marino, C., Sacchi, M., Spiess, V., Steinmann, L. & Vitale, S.
1313 (2022b). Integrated on-land-offshore stratigraphy of the Campi Flegrei caldera: New

1314 insights into the volcano-tectonic evolution in the last 15 kyr. *Basin Research* **34**, 855–
1315 882.

1316 Natale, J., Vitale, S. & Isaia, R. (2024a). Simultaneous normal and reverse faulting in
1317 reactivating caldera faults: A detailed field structural analysis from Campi Flegrei
1318 (southern Italy). *Journal of Structural Geology* **181**, 105109.

1319 Natale, J., Vitale, S., Repola, L., Monti, L. & Isaia, R. (2024b). Geomorphic analysis of digital
1320 elevation model generated from vintage aerial photographs: A glance at the pre-
1321 urbanization morphology of the active Campi Flegrei caldera. *Geomorphology* **460**,
1322 109267.

1323 Németh, K., Carrasco-Núñez, G., Aranda-Gómez, J. J. & Smith, I. E. M. (2017). *Monogenetic*
1324 *Volcanism*. Geological Society of London.

1325 Nunziata, C. (2010). Low shear-velocity zone in the Neapolitan-area crust between the Campi
1326 Flegrei and Vesuvio volcanic areas. *Terra Nova* **22**, 208–217.

1327 Orsi, G., De Vita, S. & Di Vito, M. (1996). The restless, resurgent Campi Flegrei nested
1328 caldera (Italy): constraints on its evolution and configuration. *Journal of Volcanology*
1329 *and Geothermal Research* **74**, 179–214.

1330 Orsi, G., Di Vito, M. A. & Isaia, R. (2004). Volcanic hazard assessment at the restless Campi
1331 Flegrei caldera. *Bulletin of Volcanology* **66**, 514–530.

1332 Pamukcu, A. S., Gualda, G. A. R., Ghiorso, M. S., Miller, C. F. & McCracken, R. G. (2015).
1333 Phase-equilibrium geobarometers for silicic rocks based on rhyolite-MELTS—Part 3:
1334 Application to the Peach Spring Tuff (Arizona–California–Nevada, USA).
1335 *Contributions to Mineralogy and Petrology* **169**, 33.

1336 Pappalardo, L. & Mastrolorenzo, G. (2012). Rapid differentiation in a sill-like magma
1337 reservoir: a case study from the campi flegrei caldera. *Scientific Reports* **2**, 712.

1338 Pappalardo, L., Piochi, M., d'Antonio, M., Civetta, L. & Petrini, R. (2002). Evidence for
1339 multi-stage magmatic evolution during the past 60 kyr at Campi Flegrei (Italy)
1340 deduced from Sr, Nd and Pb isotope data. *Journal of Petrology* **43**, 1415–1434.

1341 Passmore, E., Maclennan, J., Fitton, G. & Thordarson, T. (2012). Mush Disaggregation in
1342 Basaltic Magma Chambers: Evidence from the ad 1783 Laki Eruption. *Journal of*
1343 *Petrology* **53**, 2593–2623.

1344 Pearce, J. A. & Peate, D. W. (1995). Tectonic implications of the composition of volcanic arc
1345 magmas. *Annual review of Earth and planetary sciences* **23**, 251–285.

1346 Peccerillo, A. (2017). The Campania Province. In: Peccerillo, A. (ed.) *Cenozoic Volcanism in*
1347 *the Tyrrhenian Sea Region*. Cham: Springer International Publishing, 159–201.

1348 Peccerillo, A. & Frezzotti, M. (2015). Magmatism, mantle evolution and geodynamics at the
1349 converging plate margins of Italy. *Journal of the Geological Society* **172**, 407–427.

1350 Pérez-Orozco, J. D., Sosa-Ceballos, G. & Macías, J. L. (2021). Tectonic and magmatic
1351 controls on the evolution of post-collapse volcanism. Insights from the Acoculco
1352 Caldera Complex, Puebla, México. *Lithos* **380–381**, 105878.

1353 Perinelli, C., Gaeta Mario, Bonechi Barbara, F. Granati Serena, Carmela, F., Massimo, D.,
1354 Vincenzo, S., Stefania, S. & Claudia, R. (2019). Effect of water on the phase relations
1355 of primitive K-basalts: Implications for high-pressure differentiation in the Phlegraean
1356 Volcanic District magmatic system. *Lithos* **342–343**, 530–541.

1357 Petrelli, M., Ágreda López, M., Pisello, A. & Perugini, D. (2023). Pre-eruptive dynamics at
1358 the Campi Flegrei Caldera: from evidence of magma mixing to timescales estimates.
1359 *Earth, Planets and Space* **75**, 19.

1360 Piochi, M., Kilburn, C. R. J., Di Vito, M. A., Mormone, A., Tramelli, A., Troise, C. & De
1361 Natale, G. (2014). The volcanic and geothermally active Campi Flegrei caldera: an
1362 integrated multidisciplinary image of its buried structure. *International Journal of*
1363 *Earth Sciences* **103**, 401–421.

1364 Piochi, M., Mastrolorenzo, G. & Pappalardo, L. (2005). Magma ascent and eruptive processes
1365 from textural and compositional features of Monte Nuovo pyroclastic products, Campi
1366 Flegrei, Italy. *Bulletin of Volcanology* **67**, 663–678.

1367 Piochi, M., Polacci, M., De Astis, G., Zanetti, A., Mangiacapra, A., Vannucci, R. & Giordano,
1368 D. (2008). Texture and composition of pumices and scoriae from the Campi Flegrei
1369 caldera (Italy): Implications on the dynamics of explosive eruptions. *Geochemistry,*
1370 *Geophysics, Geosystems* **9**.

1371 Pistolesi, M., Bertagnini, A., Di Roberto, A., Isaia, R., Vona, A., Cioni, R. & Giordano, G.
1372 (2017). The Baia–Fondi di Baia eruption at Campi Flegrei: stratigraphy and dynamics
1373 of a multi-stage caldera reactivation event. *Bulletin of Volcanology* **79**, 67.

1374 Pontevivo, A. & Panza, G. F. (2006). The Lithosphere-Asthenosphere System in the Calabrian
1375 Arc and Surrounding Seas – Southern Italy. *Pure and Applied Geophysics* **163**, 1617–
1376 1659.

1377 Putirka, K. D. (2008). Thermometers and Barometers for Volcanic Systems. *Reviews in*
1378 *Mineralogy and Geochemistry* **69**, 61–120.

1379 Robertson, E. A. M., Biggs, J., Cashman, K. V., Floyd, M. A. & Vye-Brown, C. (2016).
1380 Influence of regional tectonics and pre-existing structures on the formation of
1381 elliptical calderas in the Kenyan Rift. *Geological Society, London, Special*
1382 *Publications* **420**, 43–67.

1383 Rolandi, G., Bellucci, F., Heizler, M. T., Belkin, H. E. & De Vivo, B. (2003). Tectonic
1384 controls on the genesis of ignimbrites from the Campanian Volcanic Zone, southern
1385 Italy. *Mineralogy and Petrology* **79**, 3–31.

1386 Romano, C., Giordano, D., Papale, P., Mincione, V., Dingwell, D. B. & Rosi, M. (2003). The
1387 dry and hydrous viscosities of alkaline melts from Vesuvius and Phlegrean Fields.
1388 *Chemical Geology* **202**, 23–38.

1389 Rooney, T. O., Hart, W. K., Hall, C. M., Ayalew, D., Ghiorso, M. S., Hidalgo, P. & Yirgu, G.
1390 (2012). Peralkaline magma evolution and the tephra record in the Ethiopian Rift.
1391 *Contributions to Mineralogy and Petrology* **164**, 407–426.

1392 Rosi, M. & Sbrana, A. (1987). Phlegrean fields. *Quaderni de la ricerca scientifica* **9**.

1393 Sarbas, B. (2008). The GEOROC database as part of a growing geoinformatics network.
1394 paper presented at the Geoinformatics 2008—Data to Knowledge. USGS, 42–43.

1395 Saxby, J., Gottsmann, J., Cashman, K. & Gutiérrez, E. (2016). Magma storage in a strike-slip
1396 caldera. *Nature Communications* **7**, 12295.

1397 Scandone, R., Bellucci, F., Lirer, L. & Rolandi, G. (1991). The structure of the Campanian
1398 Plain and the activity of the Neapolitan volcanoes (Italy). *Journal of Volcanology and*
1399 *Geothermal Research* **48**, 1–31.

Scotto di Uccio, F. *et al.* (2024). Delineation and Fine-Scale Structure of Fault Zones Activated During the 2014–2024 Unrest at the Campi Flegrei Caldera (Southern Italy) From High-Precision Earthquake Locations. *Geophysical Research Letters* **51**, e2023GL107680.

Sims, K. W. W., Maclennan, J., Blichert-Toft, J., Mervine, E. M., Blusztajn, J. & Grönvold, K. (2013). Short length scale mantle heterogeneity beneath Iceland probed by glacial modulation of melting. *Earth and Planetary Science Letters* **379**, 146–157.

Sisson, T. W. & Grove, T. L. (1993). Experimental investigations of the role of H20 in calc-alkaline differentiation and subduction zone magmatism. *Contributions to Mineralogy and Petrology* **113**, 143–166.

Smith, P. M. & Asimow, P. D. (2005). Adiabat_1ph: A new public front-end to the MELTS, pMELTS, and pHMELTS models. *Geochemistry, Geophysics, Geosystems* **6**.

Smith, V., Isaia, R. & Pearce, N. (2011). Tephrostratigraphy and glass compositions of post-15 kyr Campi Flegrei eruptions: implications for eruption history and chronostratigraphic markers. *Quaternary Science Reviews* **30**, 3638–3660.

Sollevanti, F. (1983). Geologic, volcanologic, and tectonic setting of the Vico-Cimino area, Italy. *Journal of Volcanology and Geothermal Research* **17**, 203–217.

Stock, M. J., Humphreys, M. C., Smith, V. C., Isaia, R., Brooker, R. A. & Pyle, D. M. (2018). Tracking volatile behaviour in sub-volcanic plumbing systems using apatite and glass: insights into pre-eruptive processes at Campi Flegrei, Italy. *Journal of Petrology* **59**, 2463–2492.

1421 Stock, M. J., Humphreys, M. C., Smith, V. C., Isaia, R. & Pyle, D. M. (2016). Late-stage
1422 volatile saturation as a potential trigger for explosive volcanic eruptions. *Nature*
1423 *Geoscience* **9**, 249–254.

1424 Tomlinson, E. L. *et al.* (2012). Geochemistry of the Phlegraean Fields (Italy) proximal
1425 sources for major Mediterranean tephras: Implications for the dispersal of Plinian and
1426 co-ignimbritic components of explosive eruptions. *Geochimica et Cosmochimica Acta*
1427 **93**, 102–128.

1428 Toplis, M. J. & Carroll, M. R. (1995). An Experimental Study of the Influence of Oxygen
1429 Fugacity on Fe-Ti Oxide Stability, Phase Relations, and Mineral—Melt Equilibria in
1430 Ferro-Basaltic Systems. *Journal of Petrology* **36**, 1137–1170.

1431 Troiano, A., Di Giuseppe, M. G. & Isaia, R. (2022). 3D structure of the Campi Flegrei caldera
1432 central sector reconstructed through short-period magnetotelluric imaging. *Scientific*
1433 *Reports* **12**, 20802.

1434 Troiano, A., Di Giuseppe, M. G., Petrillo, Z., Troise, C. & De Natale, G. (2011). Ground
1435 deformation at calderas driven by fluid injection: modelling unrest episodes at Campi
1436 Flegrei (Italy). *Geophysical Journal International* **187**, 833–847.

1437 Vetere, F., Botcharnikov, R. E., Holtz, F., Behrens, H. & De Rosa, R. (2011). Solubility of
1438 H2O and CO2 in shoshonitic melts at 1250 C and pressures from 50 to 400 MPa:
1439 implications for Campi Flegrei magmatic systems. *Journal of Volcanology and*
1440 *Geothermal Research* **202**, 251–261.

1441 Vilardo, G., Isaia, R., Ventura, G., De Martino, P. & Terranova, C. (2010). InSAR Permanent
1442 Scatterer analysis reveals fault re-activation during inflation and deflation episodes at
1443 Campi Flegrei caldera. *Remote Sensing of Environment* **114**, 2373–2383.

1444 Villemant, B. (1988). Trace element evolution in the Phlegrean Fields (Central Italy):
1445 fractional crystallization and selective enrichment. *Contributions to Mineralogy and*
1446 *Petrology* **98,** 169-183.
1447 Vineberg, S. O., Isaia, R., Albert, P. G., Brown, R. J. & Smith, V. C. (2023). Insights into the
1448 explosive eruption history of the Campanian volcanoes prior to the Campanian
1449 Ignimbrite eruption. *Journal of Volcanology and Geothermal Research* **443**, 107915.

1450 Vitale, S. & Ciarcia, S. (2018). Tectono-stratigraphic setting of the Campania region (southern
1451 Italy). *Journal of Maps*. Taylor & Francis **14**, 9–21.

1452 Vitale, S. & Isaia, R. (2014). Fractures and faults in volcanic rocks (Campi Flegrei, southern
1453 Italy): insight into volcano-tectonic processes. *International Journal of Earth Sciences*
1454 **103**, 801–819.

1455 Vitale, S. & Natale, J. (2023). Combined volcano-tectonic processes for the drowning of the
1456 Roman western coastal settlements at Campi Flegrei (southern Italy). *Earth, Planets*
1457 *and Space* **75**, 38.

1458 Voloschina, M. *et al.* (2018). Magmatic reactivation of the Campi Flegrei volcanic system:
1459 insights from the Baia–Fondi di Baia eruption. *Bulletin of Volcanology* **80**, 75.

1460 Webster, J., Raia, F., Tappen, C. & De Vivo, B. (2003). Pre-eruptive geochemistry of the
1461 ignimbrite-forming magmas of the Campanian Volcanic Zone, Southern Italy,
1462 determined from silicate melt inclusions. *Mineralogy and Petrology* **79**, 99–125.

1463 Willmott, C. J. (1981). On the Validation of Models. *Physical Geography*. Taylor & Francis **2**,
1464 184–194.

Woo, J. Y. L. & Kilburn, C. R. J. (2010). Intrusion and deformation at Campi Flegrei, southern Italy: Sills, dikes, and regional extension. *Journal of Geophysical Research: Solid Earth* **115**.

Zollo, A., Maercklin, N., Vassallo, M., Dello Iacono, D., Virieux, J. & Gasparini, P. (2008). Seismic reflections reveal a massive melt layer feeding Campi Flegrei caldera. *Geophysical Research Letters* **35**.

FIGURE CAPTIONS

Figure 1: Maps showing Campi Flegrei and vent locations of eruptions in the last 15 kyr. (a) Map of Italy showing the location of Campi Flegrei, square indicates area enlarged in (b) to show sampling locations of the basement rocks (b) Simplified geological map of southern Apennines showing distribution of tectonic units (Ciarcia and Vitale, 2025) and the locations the basement rocks were sampled: 1. Syn-orogenic wedge-top flysch, sample 23-FMR-003; 2. Limestone, sample 23-FMR-001; 3. Syenite, sample 23-FMR-014; 4. Palaeozoic gneiss, sample 23-FMR-017. (c) Simplified geological map of Campi Flegrei showing locations of the vents in the last 15 kyr, from Smith et al. (2011). Colours refer to the tectonic setting of the vents: orange are eruptions that occurred along the northern/eastern caldera rim faults; purple are eruptions with vents along regional and rim faults on the western side of the caldera; and in green are the eruptions from vents in the central eastern side of the caldera. Map also shows the distribution of pyroclastic deposits (Natale *et al.*, 2024b, 2024a) and caldera and crater rims (Vitale and Isaia, 2014; Natale *et al.*, 2022a). Vent ages refer to epochs defined in Smith et al. (2011).

Figure 2: Major element variation diagrams of literature glass data for Campi Flegrei eruptions in the last 15 kyr. Points are coloured by tectonic group as illustrated in Figure 1. Error bars show representative 2 s.d. error from EPMA analysis from Smith et al. (2011). Glass data was compiled from GEOROC, see *Literature data* for references. Glass data from Minopoli 2 eruption, which forms a distinct high-MgO group, are shown with diamond markers and data from the Fondi di Baia eruption, which is discussed in the *Assimilation at Fondi di Baia* section, are shown with square markers.

Figure 3: Phase proportions as a function of magma temperature for fractional crystallisation MELTS models at different pressures. Models are run at L_{fO2}= QFM+1 and L_{H2O} = 2 wt%. Phases highlighted in red are not observed in natural Campi Flegrei samples in the major crystallising assemblage. Phases not in key: nph, nepheline; rhm-ox, rhombohedral oxide

Figure 4: The effect of varying each intensive parameter on the resulting liquid line of descent predicted by Rhyolite-MELTS. The colour of the line represents the value of the intensive parameter being varied (where blue to red indicates the intensive parameter increasing from the lowest to highest value tested) : L_{H2O} from 1 – 6 wt% in (a), (b), (c); L_{fO2} from -2 to +3 log units below/above the QFM buffer in (d), (e), (f); pressure from 50 to 500 MPa in (g), (h), (i). For (a)-(f), pressure was held constant at 160 MPa. For (d)-(i), L_{H2O} was 2 wt%. For (a)-(c) and (g)-(i), L_{fO2} was QFM+1. The grey points are all literature glass data for eruptions in the last 15 kyr. This figure represents a selection of all Rhyolite-MELTS models run; each intensive parameter was evaluated against the full range of the remaining two.

Figure 5: The effect of varying each intensive parameter on the RMSE of the resulting Rhyolite-MELTS model. For (a), (d) and (g), pressure and oxygen fugacity are held constant at the best-fit conditions for the tectonic group and the initial H_2O content is varied. For (b), (e) and (h) H_2O content and pressure are held constant and oxygen fugacity is varied. For (c), (f) and (i) H_2O content and oxygen fugacity are both held constant and pressure is varied. The grey shaded regions in (c),(f),(i) indicate pressures at which Rhyolite-MELTS predicts the crystallisation of phases which are not observed in natural Campi Flegrei rocks (muscovite, garnet, leucite).

Figure 6: Results of all Rhyolite-MELTS models of fractional crystallisation. Grey points represent all literature glass data for eruptions in the last 15 kyr, black points are literature glass data for the tectonic group indicated. Each line represents the liquid line of descent predicted by Rhyolite-MELTS for a parental magma cooling and crystallising under a given pressure, initial H_2O content and oxygen fugacity. Each model is coloured according to the RMSE value indicating the goodness-of-fit between the model and natural data; red indicates a better fit, blue/purple indicates a worse fit. See *Statistical determination of best-fit storage conditions* for description of RMSE calculation, RMSE is an average of all major oxides. Plots of the other major oxides that are not shown in this figure are included in the Supplementary Material (SM) Fig. S19– S21.

Figure 7: Results of Rhyolite-MELTS models of assimilation-fractional crystallisation for northern/eastern caldera group eruptions. Line styles indicate different assimilant compositions, the solid black line shows the best-fit FC model for northern/eastern caldera

eruptions. For each assimilant composition, the amount of assimilant which led to the largest improvement in model fit compared to the FC-only model is plotted. The line colour refers to the percentage improvement of RMSE relative to the best-fit FC only model, pale red indicates less improvement to darker red which indicates the most improvement. Fit was calculated using normalised RMSE, as for FC models. Pale grey circles represent all literature glass data for eruptions in the last 15 kyr, dark grey circles represent literature glass data from northern/eastern caldera group eruptions. Assimilant was added en masse at 1100°C. Full results of AFC modelling for eastern caldera group eruptions are included in Fig. S7-S10

Figure 8: Results of Rhyolite-MELTS models of assimilation-fractional crystallisation for central caldera group eruptions. The colouring and line style of each Rhyolite-MELTS model is as described for Figure 7. Pale grey circles represent all literature glass data for eruptions in the last 15 kyr, dark grey circles represent literature glass data from central caldera group eruptions. Full results of AFC modelling for central caldera group eruptions are included in Fig. S11-S14

Figure 9: Results of Rhyolite-MELTS models of assimilation-fractional crystallisation for western caldera group eruptions. The colouring and line style of each Rhyolite-MELTS model is as described for Figure 7. Pale grey circles represent all literature glass data for eruptions in the last 15 kyr, dark grey circles represent literature glass data from western caldera group eruptions. Full results of AFC modelling for western caldera group eruptions are included in Fig. S15-S18

Figure 10: Rhyolite-MELTS model of limestone assimilation compared to Fondi di Baia glass data (purple circles; literature data). Solid black line is the result of the best-fit fractional crystallisation Rhyolite-MELTS model for the western caldera eruptions group. Dashed black line is the result of a Rhyolite-MELTS model run at the same pressure (160 MPa), L_{H2O} (2 wt%) and L_{fO2} conditions (at QFM buffer) with addition of 1% limestone.

Figure 11: Variation of melt physical properties along the liquid line of descent as predicted by the best-fit Rhyolite-MELTS model for each tectonic group. Models were run at 110 MPa (northern/eastern caldera), 140 MPa (central caldera) and 160 MPa (western caldera), models run at the same pressures showed no significant differences in physical properties displayed here (a) T vs dissolved H_2O content, (b) T vs density of melt, (c) T vs volume fraction of exsolved H_2O, (d) T vs melt viscosity. The vertical grey bar in each plot indicates the temperature range over which melt fraction drops and physical properties change over a short temperature interval (invariant temperature range).

Figure 1

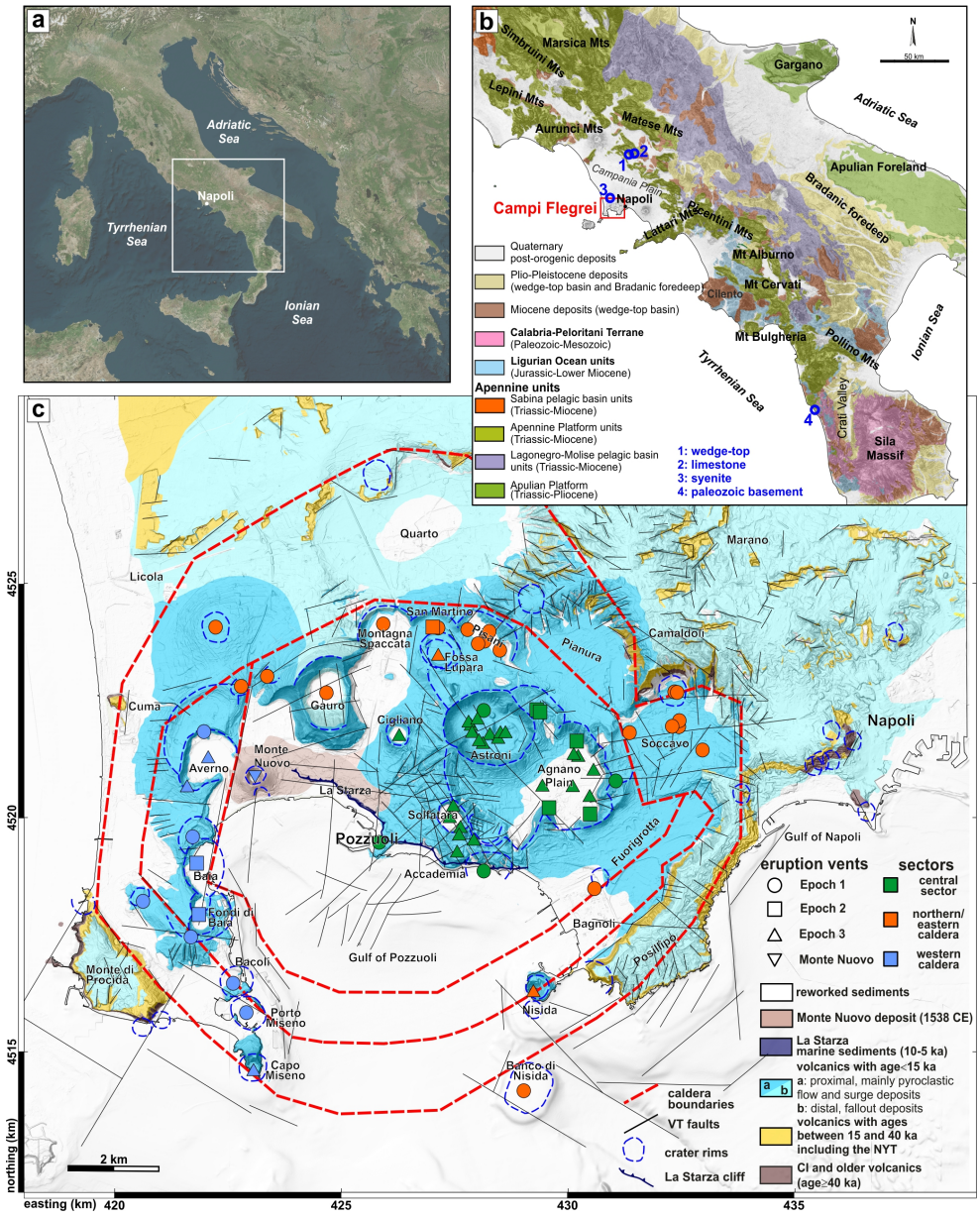
a
Adriatic Sea
Napoli
Tyrrhenian Sea
Ionian Sea
b
Simbruini Mts
Marsica Mts
Gargano
Adriatic Sea
Leprini Mts
Aurunci Mts
Matese Mts
Campania Plain
Apulian Foreland
Bradanic foredeep
Campi Flegrei
Napoli
Lattari Mts
Picentini Mts
Mt Alburno
Mt Cervati
Cilento
Mt Bulgheria
Pollino Mts
Ionian Sea
Tyrrhenian Sea
Crati Valley
Sila Massif
N
50 km
Quaternary post-orogenic deposits
Plio-Pleistocene deposits (wedge-top basin and Bradanic foredeep)
Miocene deposits (wedge-top basin)
Calabria-Peloritani Terrane (Paleozoic-Mesozoic)
Ligurian Ocean units (Jurassic-Lower Miocene)
Apennine units
Sabina pelagic basin units (Triassic-Miocene)
Apennine Platform units (Triassic-Miocene)
Lagonegro-Molise pelagic basin units (Triassic-Miocene)
Apulian Platform (Triassic-Pliocene)
1: wedge-top
2: limestone
3: syenite
4: paleozoic basement
c
Quarto
Marano
Licola
San Martino
Montagna Spaccata
Fossa Lupara
Pianura
Camaldoli
Cuma
Gauro
Cigliano
Astroni
Soccavo
Napoli
Averno
Monte Nuovo
Agnano Plain
La Starza
Solfatara
Pozzuoli
Gulf of Napoli
Baia
Accademia
Fuorigrotta
Fondi di Baia
Bagnoli
Gulf of Pozzuoli
Posillipo
Bacoli
Monte di Procida
Nisida
Porto Miseno
Capo Miseno
Banco di Nisida
eruption vents
Epoch 1
Epoch 2
Epoch 3
Monte Nuovo
sectors
central sector
northern/ eastern caldera
western caldera
reworked sediments
Monte Nuovo deposit (1538 CE)
La Starza marine sediments (10-5 ka)
volcanics with age<15 ka
a: proximal, mainly pyroclastic flow and surge deposits
b: distal, fallout deposits
volcanics with ages between 15 and 40 ka including the NYT
CI and older volcanics (age≥40 ka)
caldera boundaries
VT faults
crater rims
La Starza cliff
2 km
northing (km)
4525
4520
4515
easting (km)
420
425
430
435

Figure 2

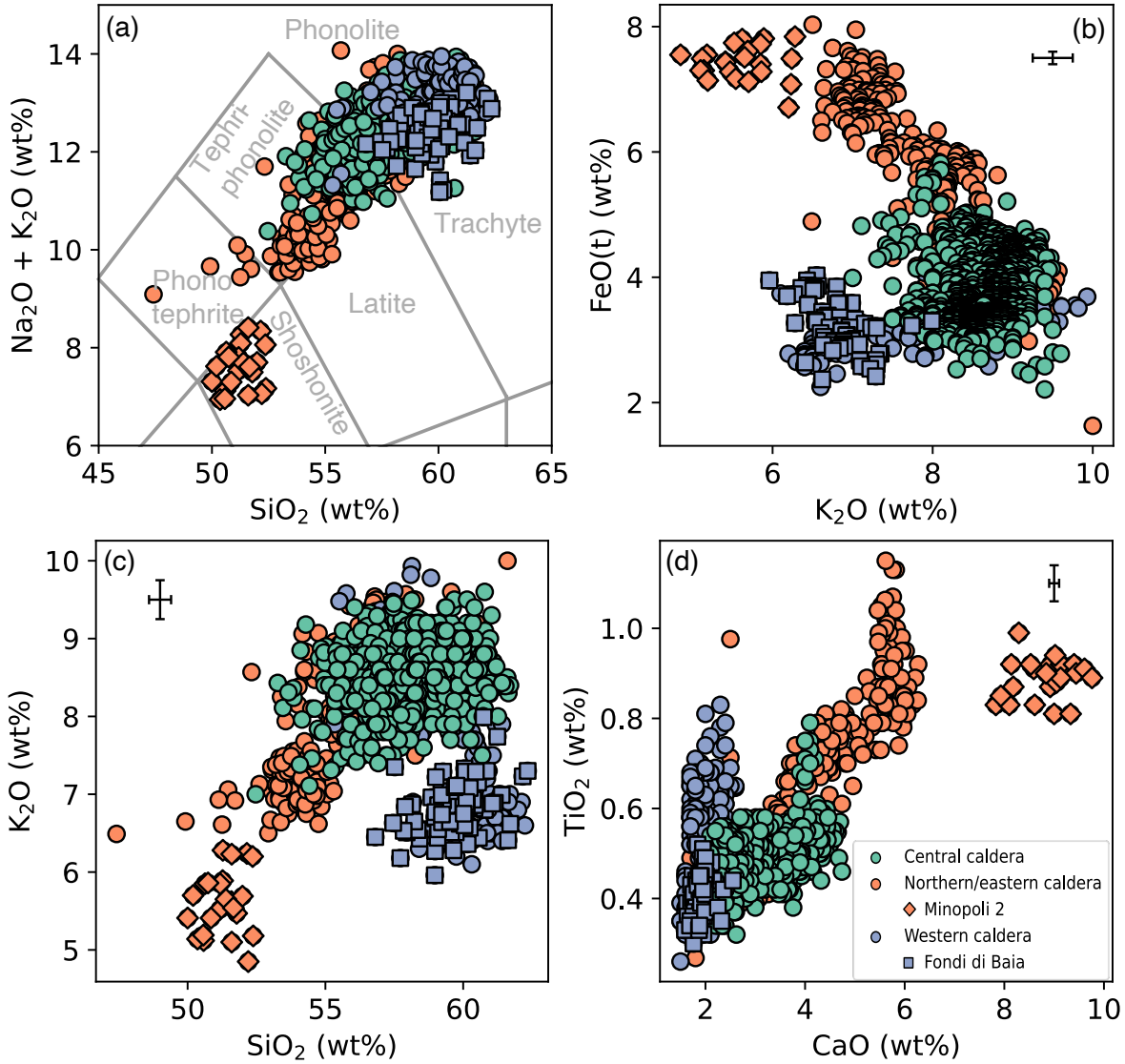
(a)
Phonolite
Tephri-phonolite
Trachyte
Phono-tephrite
Latite
Shoshonite
$Na_2O + K_2O$ (wt%)
SiO_2 (wt%)
(b)
FeO(t) (wt%)
K_2O (wt%)
(c)
K_2O (wt%)
SiO_2 (wt%)
(d)
TiO_2 (wt%)
CaO (wt%)
Central caldera
Northern/eastern caldera
Minopoli 2
Western caldera
Fondi di Baia

Figure 3

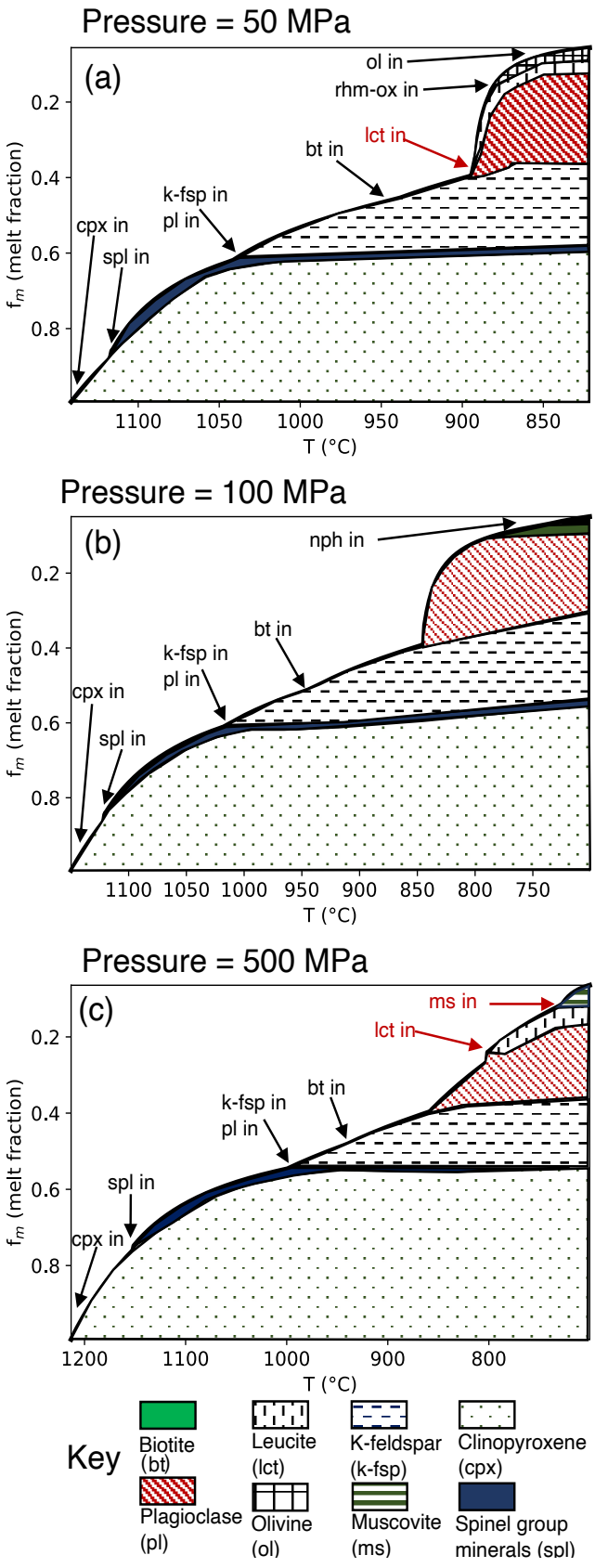
Pressure = 50 MPa
(a)
ol in
rhm-ox in
lct in
bt in
k-fsp in
pl in
cpx in
spl in
0.2
0.4
0.6
0.8
f_m (melt fraction)
1100 1050 1000 950 900 850
T (°C)
Pressure = 100 MPa
(b)
nph in
bt in
k-fsp in
pl in
cpx in
spl in
0.2
0.4
0.6
0.8
f_m (melt fraction)
1100 1050 1000 950 900 850 800 750
T (°C)
Pressure = 500 MPa
(c)
ms in
lct in
bt in
k-fsp in
pl in
spl in
cpx in
0.2
0.4
0.6
0.8
f_m (melt fraction)
1200 1100 1000 900 800
T (°C)
Key
Biotite (bt)
Leucite (lct)
K-feldspar (k-fsp)
Clinopyroxene (cpx)
Plagioclase (pl)
Olivine (ol)
Muscovite (ms)
Spinel group minerals (spl)

Figure 4

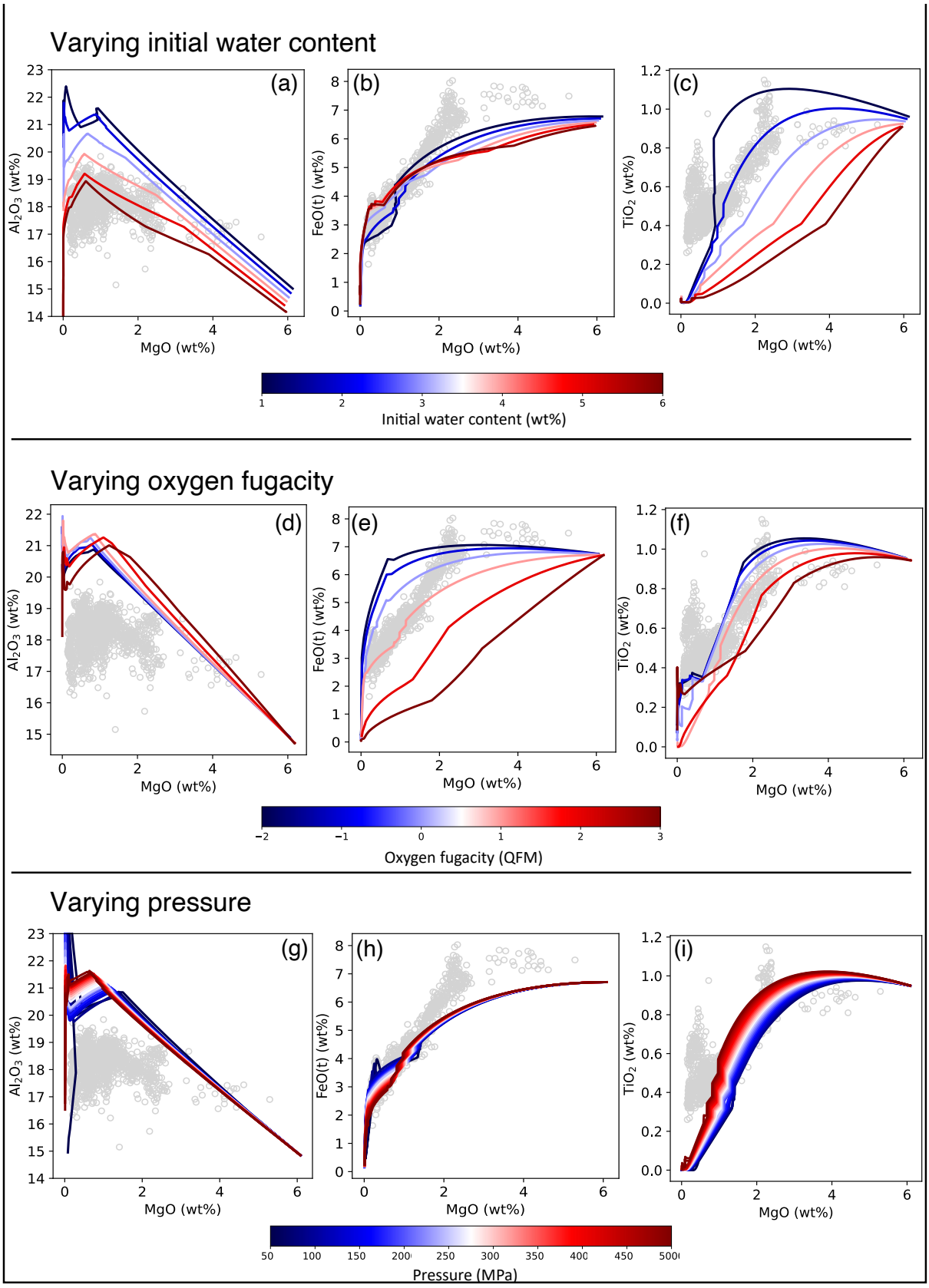
Varying initial water content
(a)
(b)
(c)
Al2O3 (wt%)
FeO(t) (wt%)
TiO2 (wt%)
MgO (wt%)
Initial water content (wt%)
Varying oxygen fugacity
(d)
(e)
(f)
Oxygen fugacity (QFM)
Varying pressure
(g)
(h)
(i)
Pressure (MPa)

Figure 5

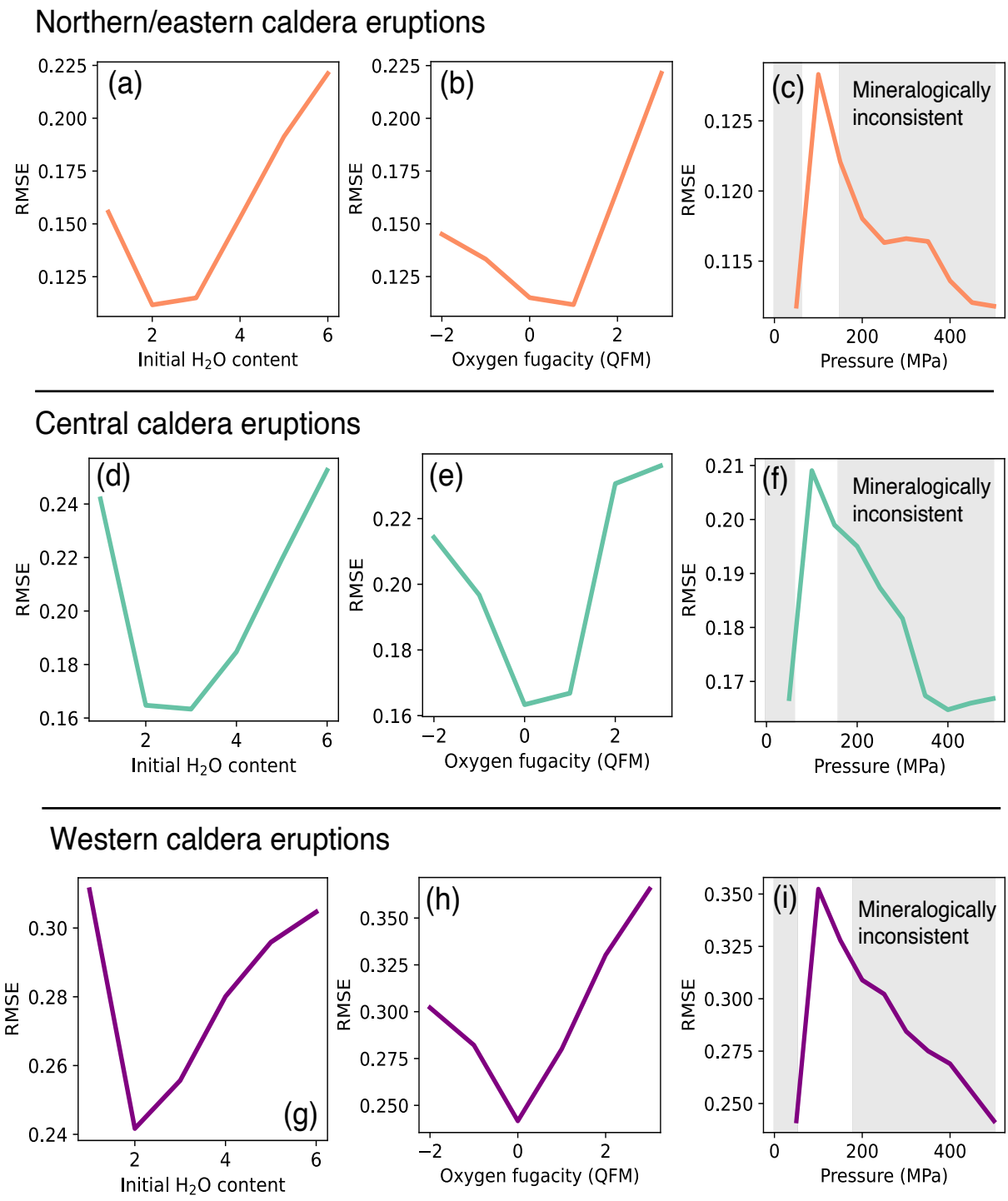
Northern/eastern caldera eruptions
(a)
(b)
(c)
Mineralogically inconsistent
RMSE
Initial H_2O content
Oxygen fugacity (QFM)
Pressure (MPa)
Central caldera eruptions
(d)
(e)
(f)
Mineralogically inconsistent
Western caldera eruptions
(g)
(h)
(i)
Mineralogically inconsistent

Figure 6

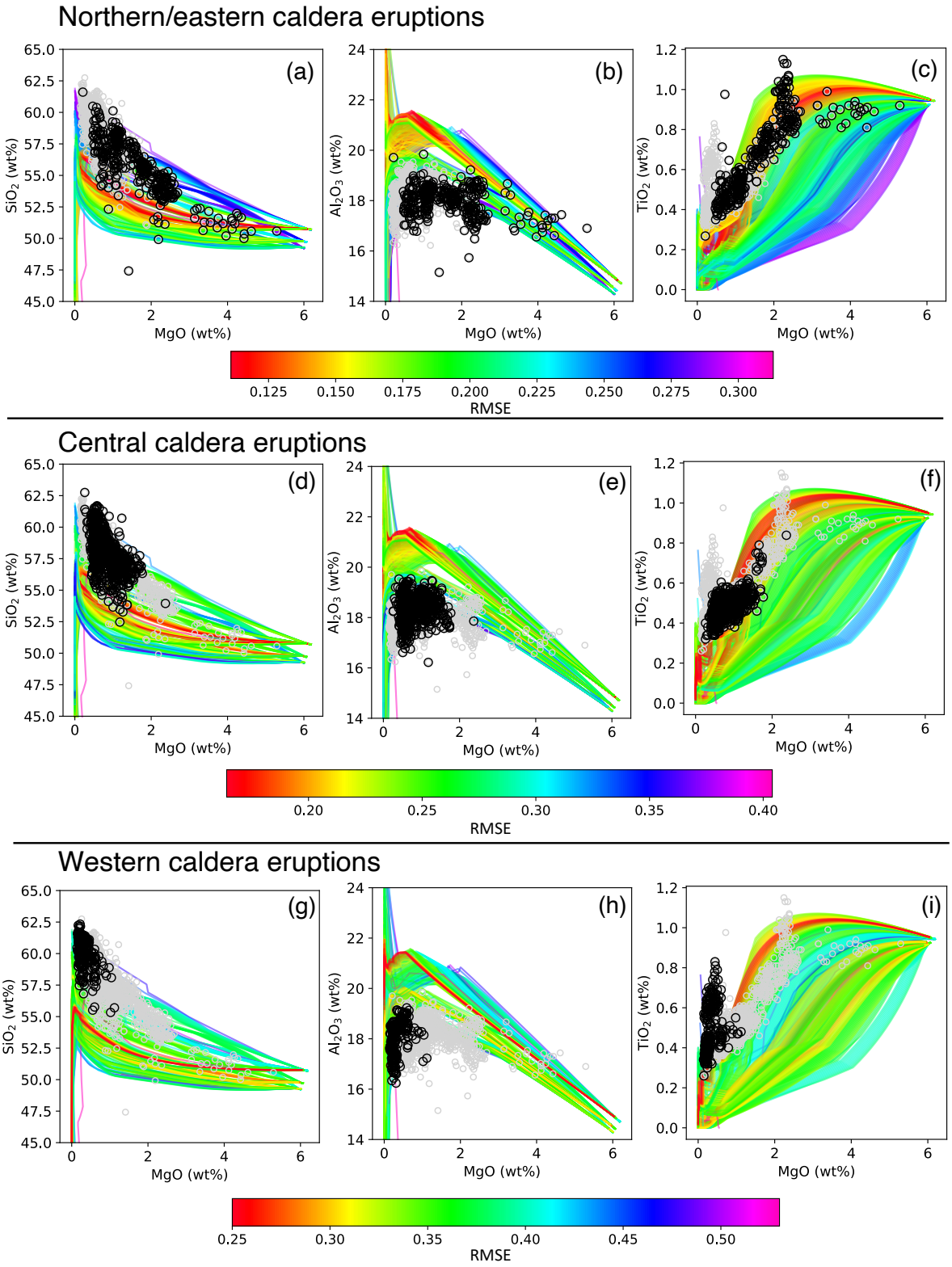
Northern/eastern caldera eruptions
(a)
(b)
(c)
SiO2 (wt%)
Al2O3 (wt%)
TiO2 (wt%)
MgO (wt%)
0.125 0.150 0.175 0.200 0.225 0.250 0.275 0.300
RMSE
Central caldera eruptions
(d)
(e)
(f)
0.20 0.25 0.30 0.35 0.40
RMSE
Western caldera eruptions
(g)
(h)
(i)
0.25 0.30 0.35 0.40 0.45 0.50
RMSE

Figure 7

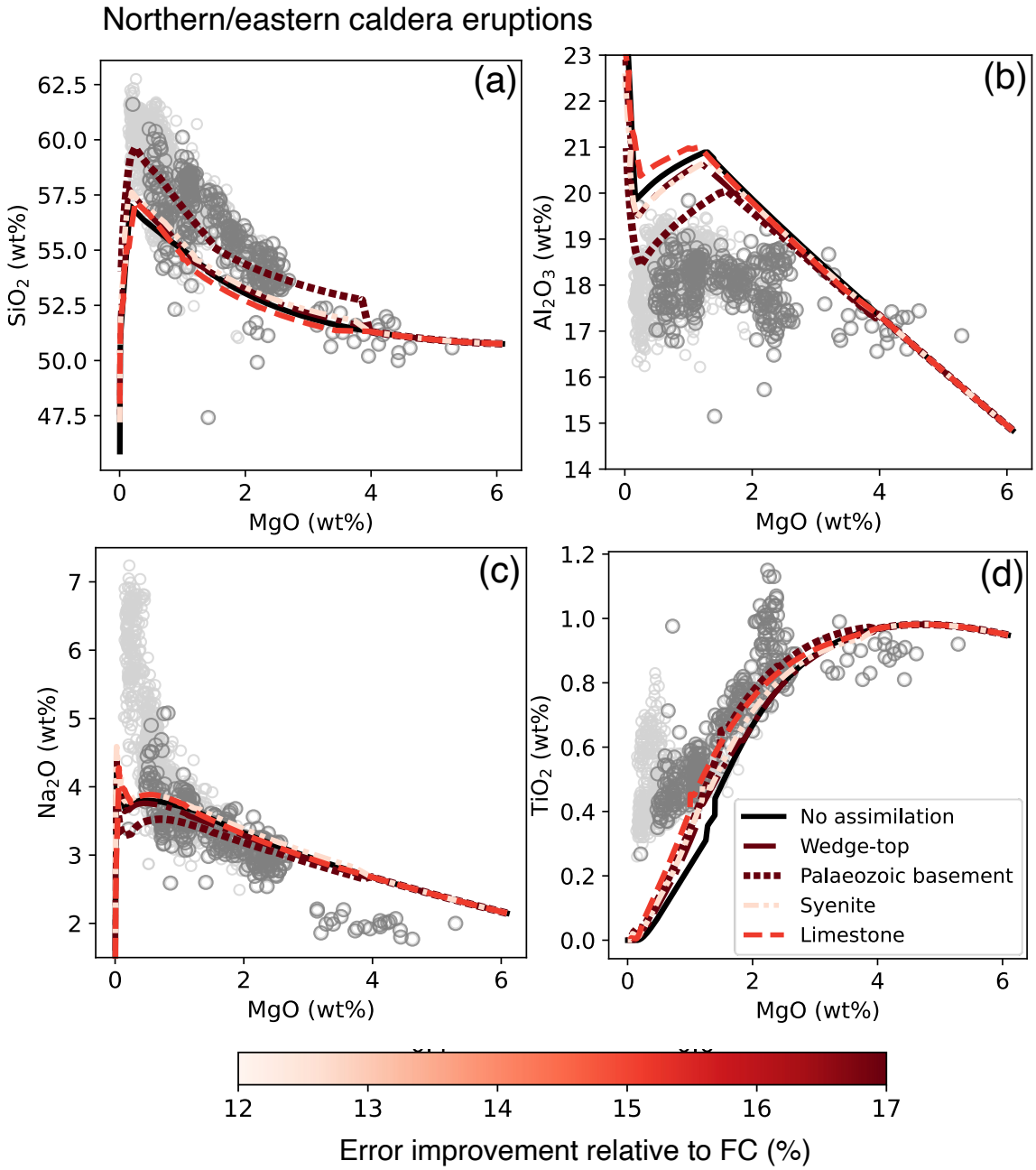
Northern/eastern caldera eruptions
(a)
(b)
(c)
(d)
SiO2 (wt%)
Al2O3 (wt%)
Na2O (wt%)
TiO2 (wt%)
MgO (wt%)
No assimilation
Wedge-top
Palaeozoic basement
Syenite
Limestone
12
13
14
15
16
17
Error improvement relative to FC (%)

Figure 8

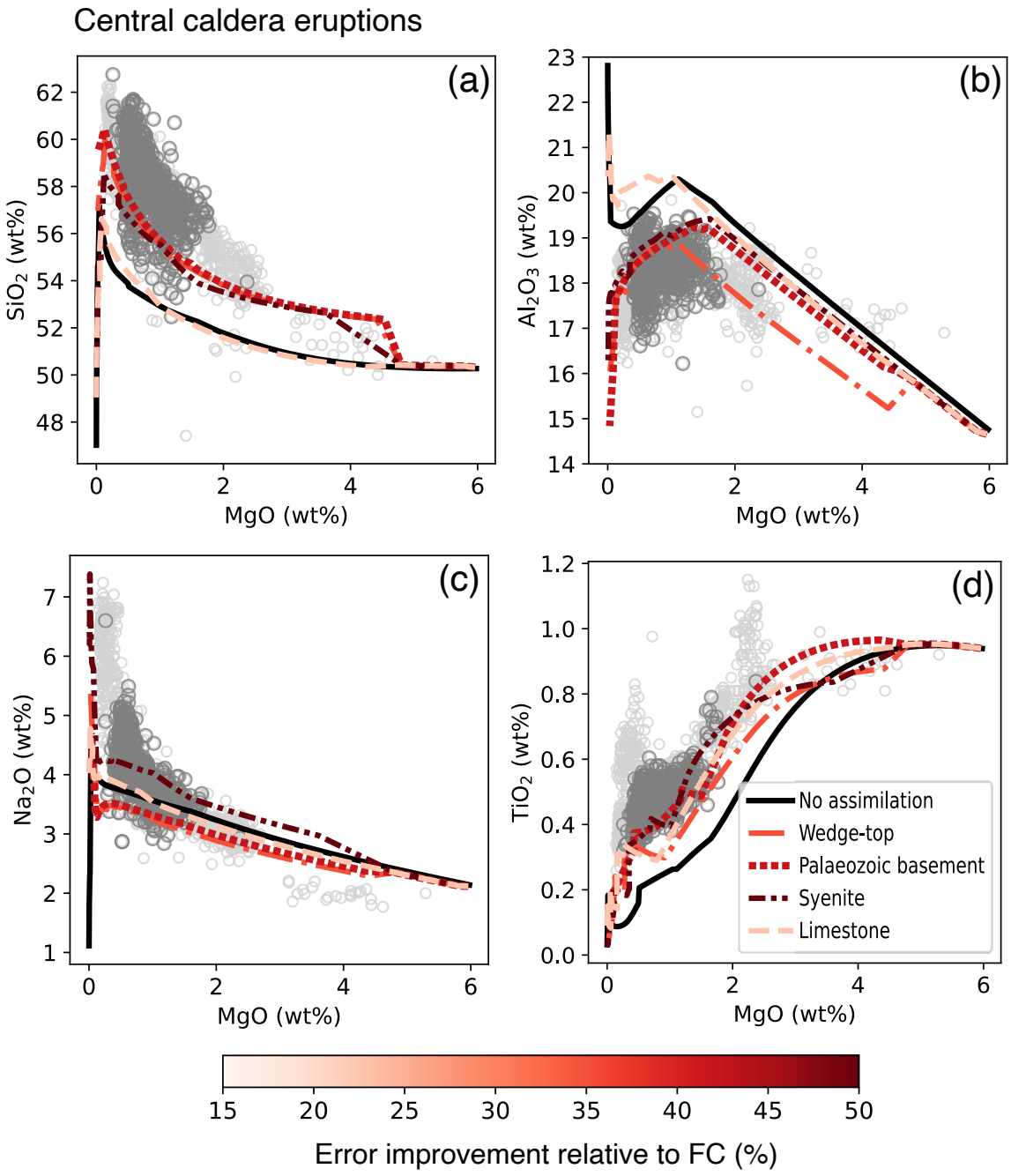
Central caldera eruptions
(a)
(b)
(c)
(d)
SiO2 (wt%)
Al2O3 (wt%)
Na2O (wt%)
TiO2 (wt%)
MgO (wt%)
No assimilation
Wedge-top
Palaeozoic basement
Syenite
Limestone
15
20
25
30
35
40
45
50
Error improvement relative to FC (%)

Figure 9

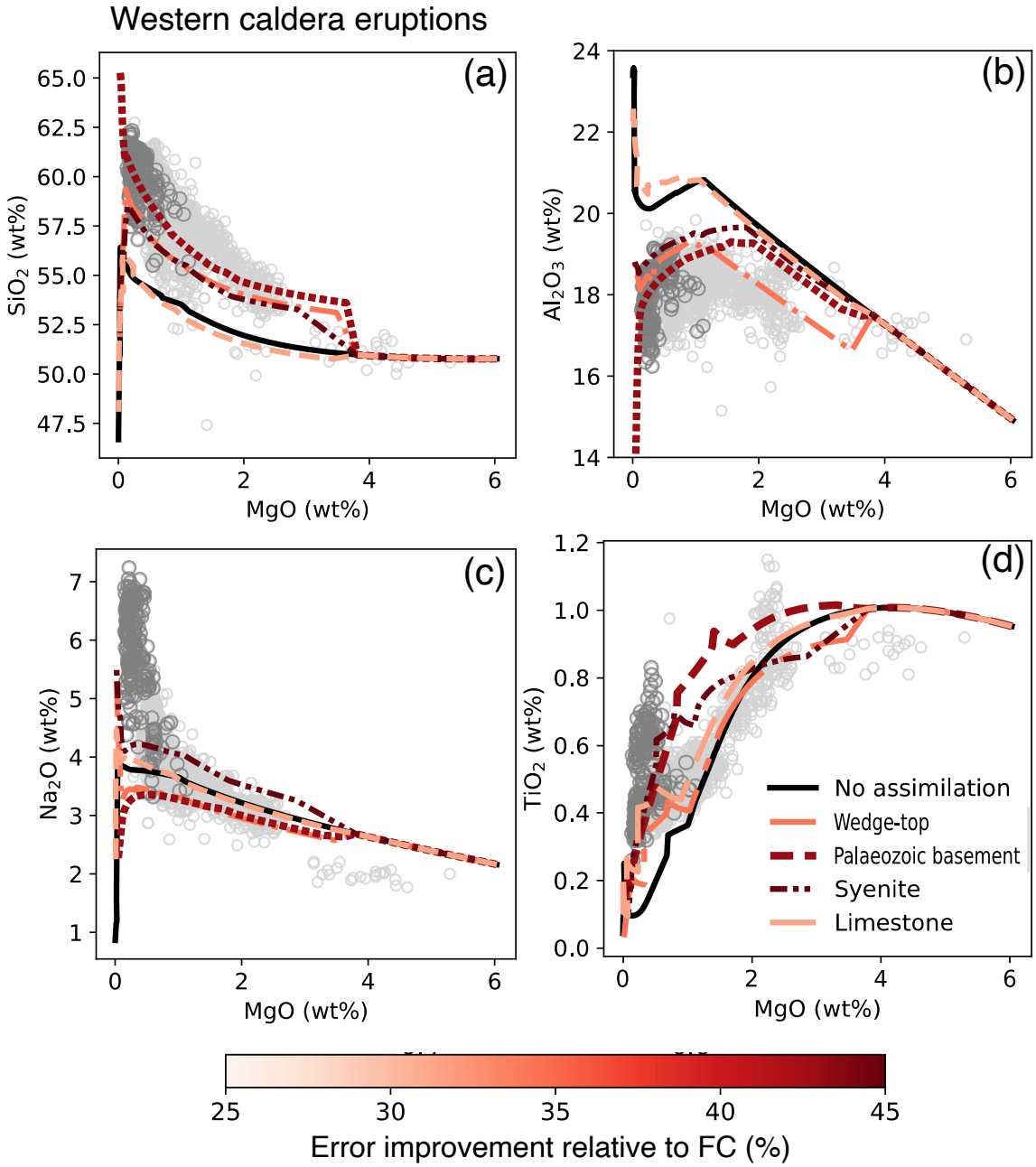
Western caldera eruptions
(a)
(b)
(c)
(d)
SiO2 (wt%)
Al2O3 (wt%)
Na2O (wt%)
TiO2 (wt%)
MgO (wt%)
No assimilation
Wedge-top
Palaeozoic basement
Syenite
Limestone
25
30
35
40
45
Error improvement relative to FC (%)

Figure 10

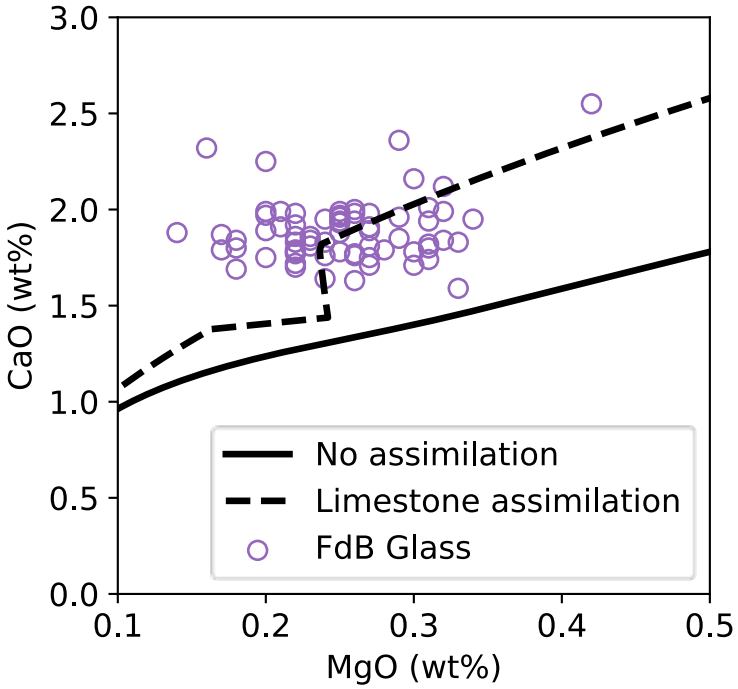

Figure 11

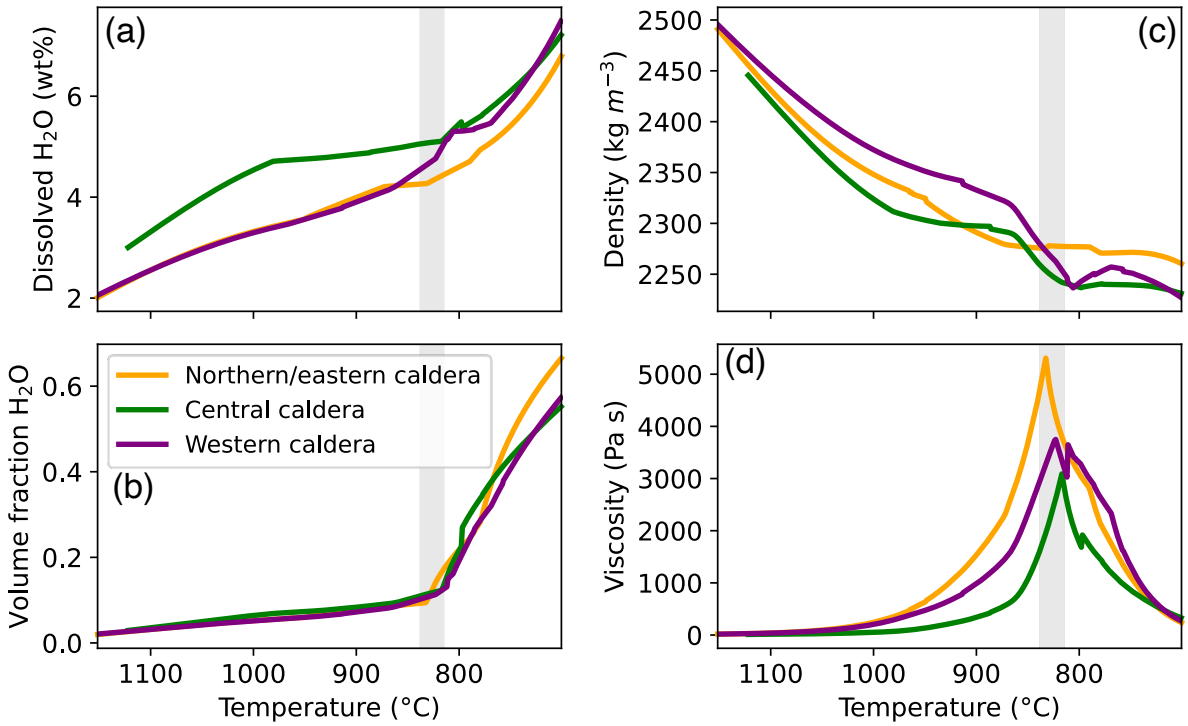

Table 1: Magma storage conditions investigated in Rhyolite-MELTS models and the ranges over which they were varied. The ranges chosen were constrained based on previous studies of Campi Flegrei.

Intensive parameter	Range tested	Intervals	References
Pressure (MPa)	50 to 500	50	Arienzo et al., 2016; Bohrson et al., 2006; Cannatelli, 2007; Fowler et al., 2007; Zollo et al., 2008.
Initial water content (wt%)	0.5, 1 to 6	1	Arienzo et al., 2016; Forni et al., 2018; Mangiacapra et al., 2008; Stock et al., 2016.
Oxygen fugacity (log units relative to the Quartz-Fayalite-Magnetite buffer)	-2 to +3	1	Cannatelli et al., 2012; Fowler et al., 2007; Stock et al., 2016.

Table 2: Best-fit FC storage conditions and assimilant compositions and quantities for each tectonic setting as defined by the lowest RMSE between Rhyolite-MELTS models and the literature glass data.

Best-fit	Northern/eastern caldera eruptions	Central caldera eruptions	Western caldera eruptions
Pressure (MPa)	110	140	160
Initial water content (wt%)	2	3	2
Oxygen fugacity (log units relative to the Quartz-Fayalite-Magnetite buffer)	1	0	0
Assimilant composition	Palaeozoic basement	Syenite	Syenite
Amount (% of total mass of magma)	10	30	30
Normalised RMSE (FC)	0.142	0.227	0.377
Normalised RMSE (AFC)	0.118	0.114	0.206

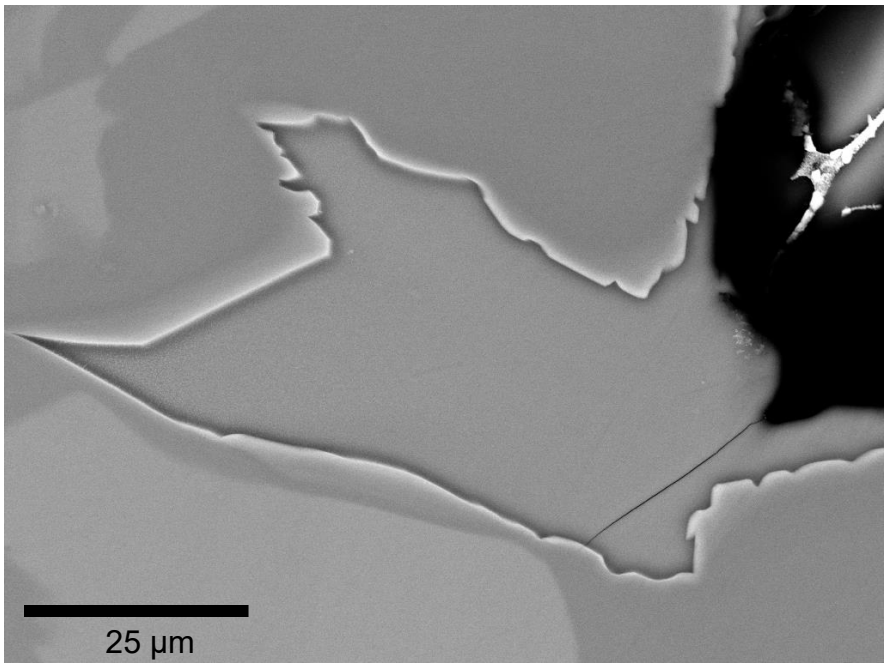

Supplementary Figure 1: Back-scattered electron image of the clinopyroxene-hosted melt inclusion used as the starting composition in the models in this study. The melt inclusion is CF410_cpx12_MI18 from Fondo Riccio, sample CF410. Image was obtained at the iCRAG labs at Trinity College Dublin, Ireland, using a Tescan S8000 MIRA 4 FEG-SEM.

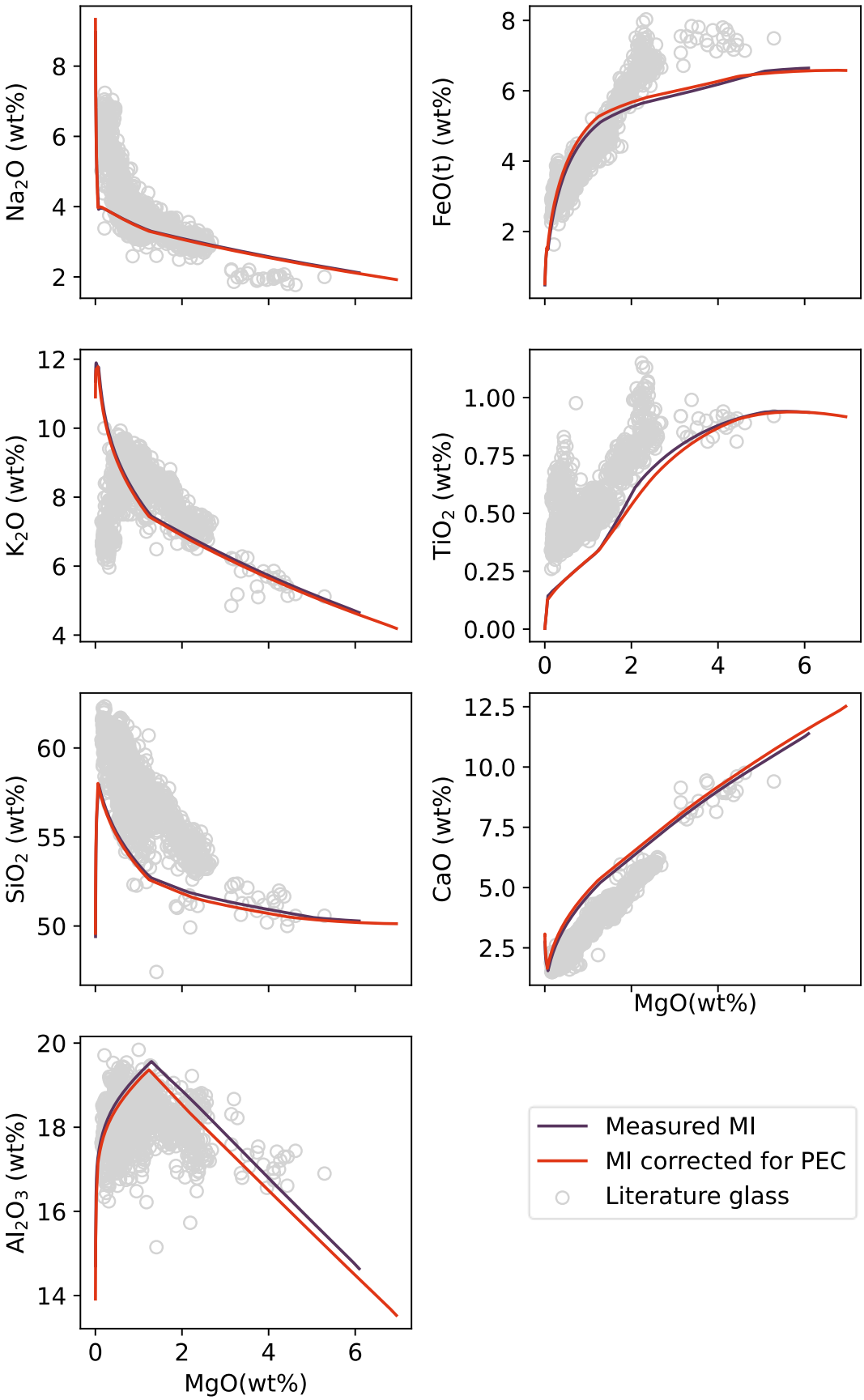

Supplementary Figure 2: Comparison of Rhyolite-MELTS models run with different starting compositions. Both models are run with the same intensive parameters of P=140 MPa, L_{fO2}=QFM and L_{H2O} = 2 wt%. The purple line uses the composition of the most mafic melt inclusion measured in this study, CF410_cpx12_MI18, which is the starting composition used throughout the rest of this study. The red line shows a model run using a starting composition recalculated from CF410_cpx12_MI18 using the post-entrapment crystallisation correction detailed in Fowler et al. (2007).

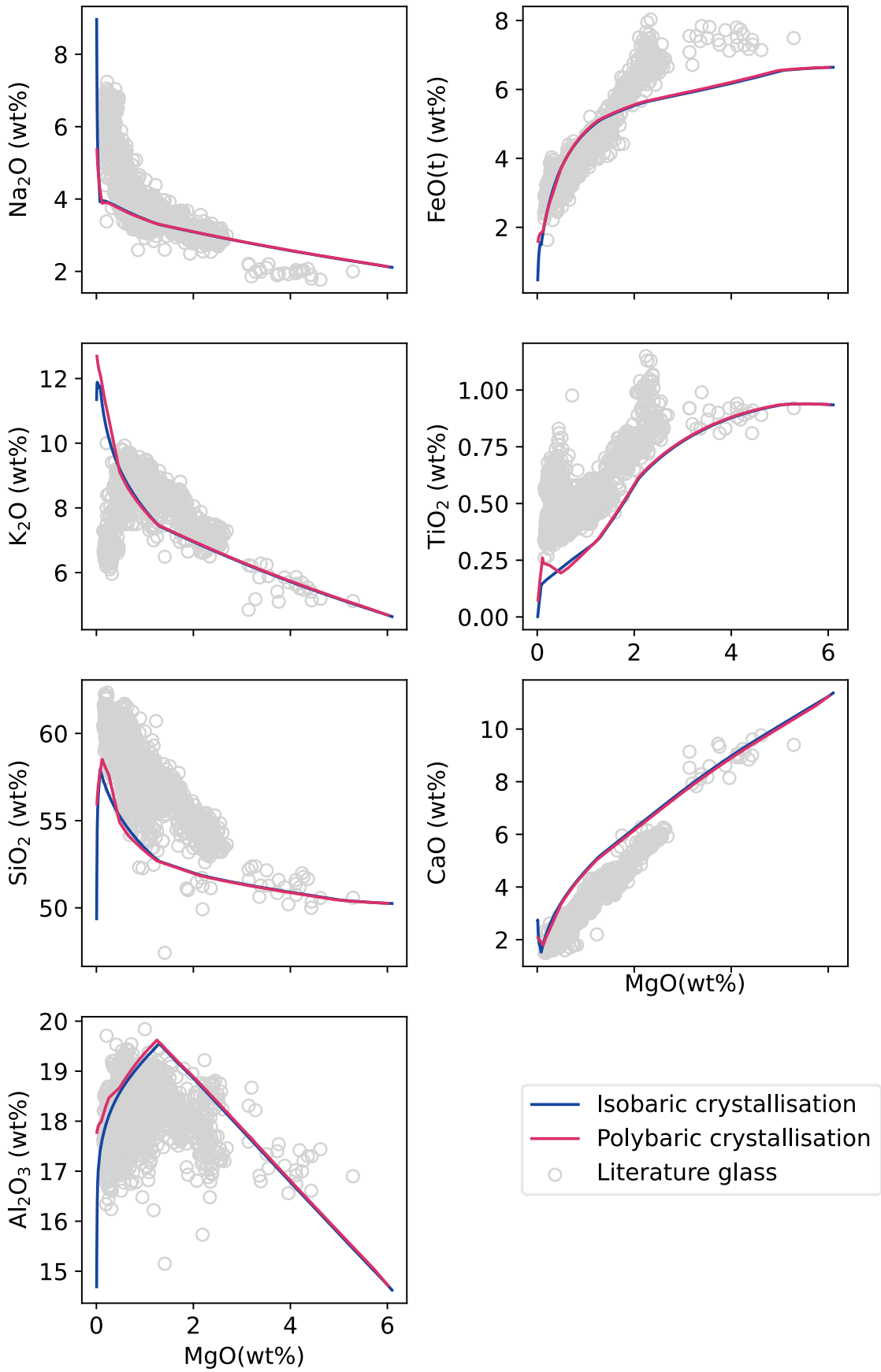

Supplementary Figure 3: Results of Rhyolite-MELTS models run under isobaric and polybaric conditions. Both models were run with L_{fO2}=QFM and L_{H2O} = 2 wt%. The blue line shows isobaric crystallisation at 160 MPa, which corresponds to a depth of ~7km assuming an average crustal density of 2300 kg cm^{-3} after Rosi and Sbrana (1987). The red line shows polybaric crystallisation; the model starts at a pressure of 160 MPa and after ~50% crystallisation the pressure is reduced to 70 MPa, equivalent to depths of ~7km and ~3km respectively. These depths were chosen to represent the main magma storage regions at Campi Flegrei identified by previous studies (e.g. Stock et al., 2018, Petrelli et al., 2023). The polybaric model fails to converge at low temperatures (~800°C, with ~15% liquid remaining). Grey circles show literature glass data.

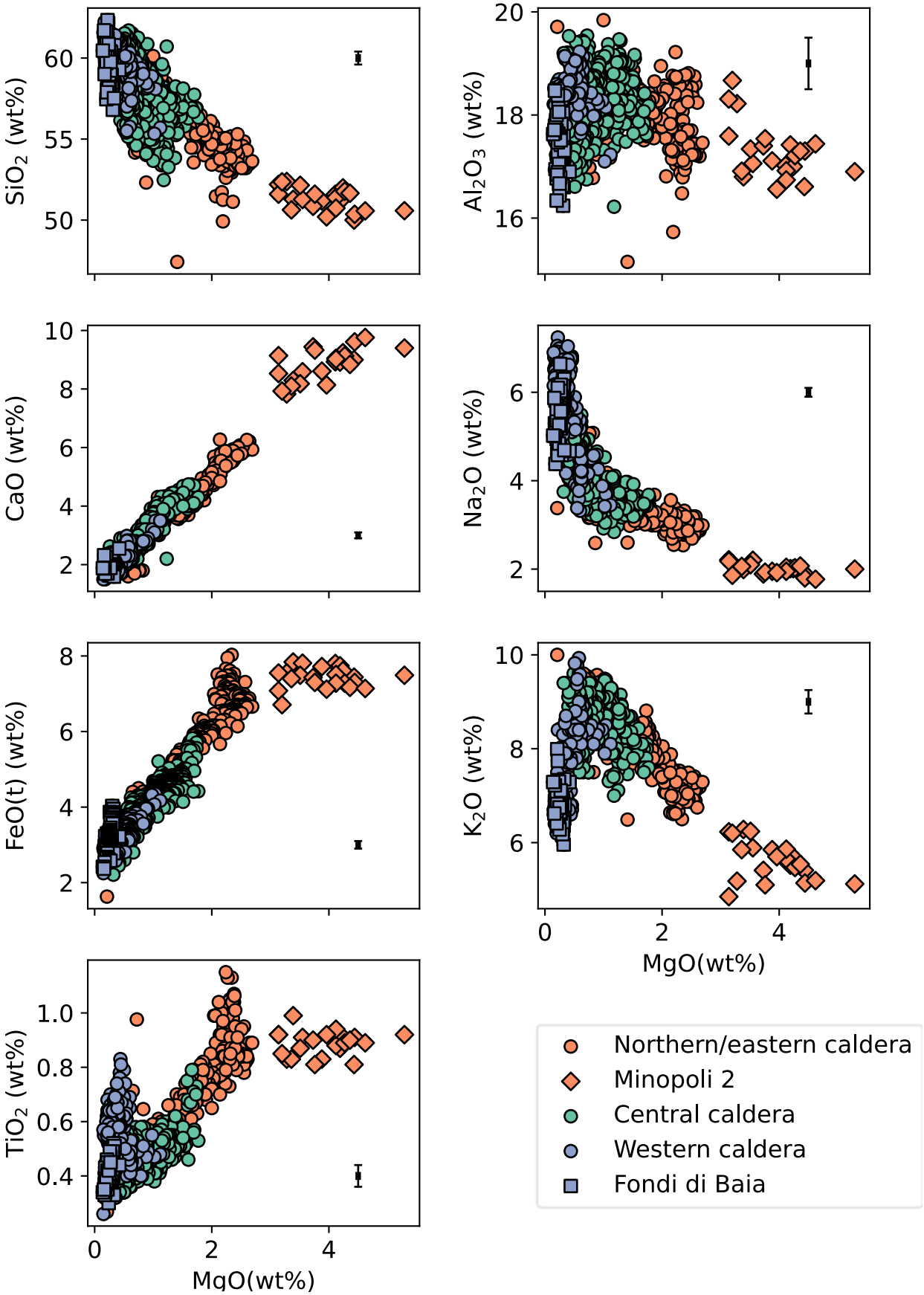

Supplementary Figure 4: Harker diagrams of literature glass data for Campi Flegrei eruptions in the last 15 kyr. Points are coloured by tectonic group as illustrated in Figure 1. Error bars show representative 2 s.d. error from EPMA analysis from Smith et al. (2011). Glass data was compiled from GEOROC and studies are referenced in *Literature data*. Minopoli 2 eruption, which forms a distinct high-MgO group, are shown with diamond markers and data from the Fondi di Baia eruption, which is discussed in the Assimilation at Fondi di Baia section, are shown with square markers.

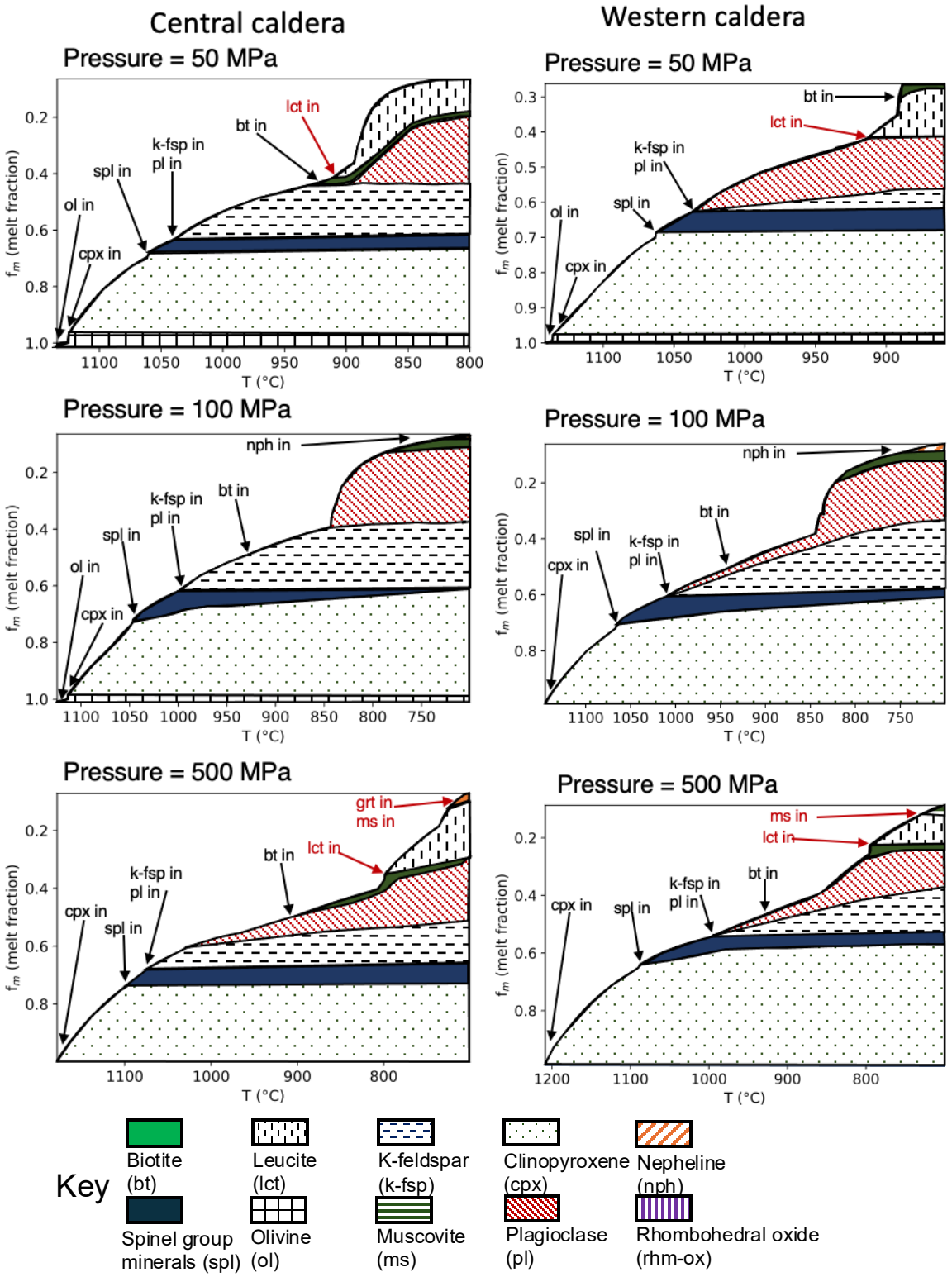

Supplementary Figure 5: Phase proportions as a function of magma temperature for fractional crystallisation MELTS models at different pressures. Central caldera models are run at L_{fO2} = QFM and initial L_{H2O} = 3 wt%. Western caldera models are run at L_{fO2} = QFM and initial H_2O = 2 wt%. Cpx, clinopyroxene; spl, spinel group minerals; k-fsp, alkali feldspar; pl, plagioclase feldspar; bt, biotite; lct, leucite; ms, muscovite; ol, olivine; nph, nepheline; rhm-ox, rhombohedral oxide. Phases highlighted in red are not observed in natural Campi Flegrei samples in the major crystallising assemblage.

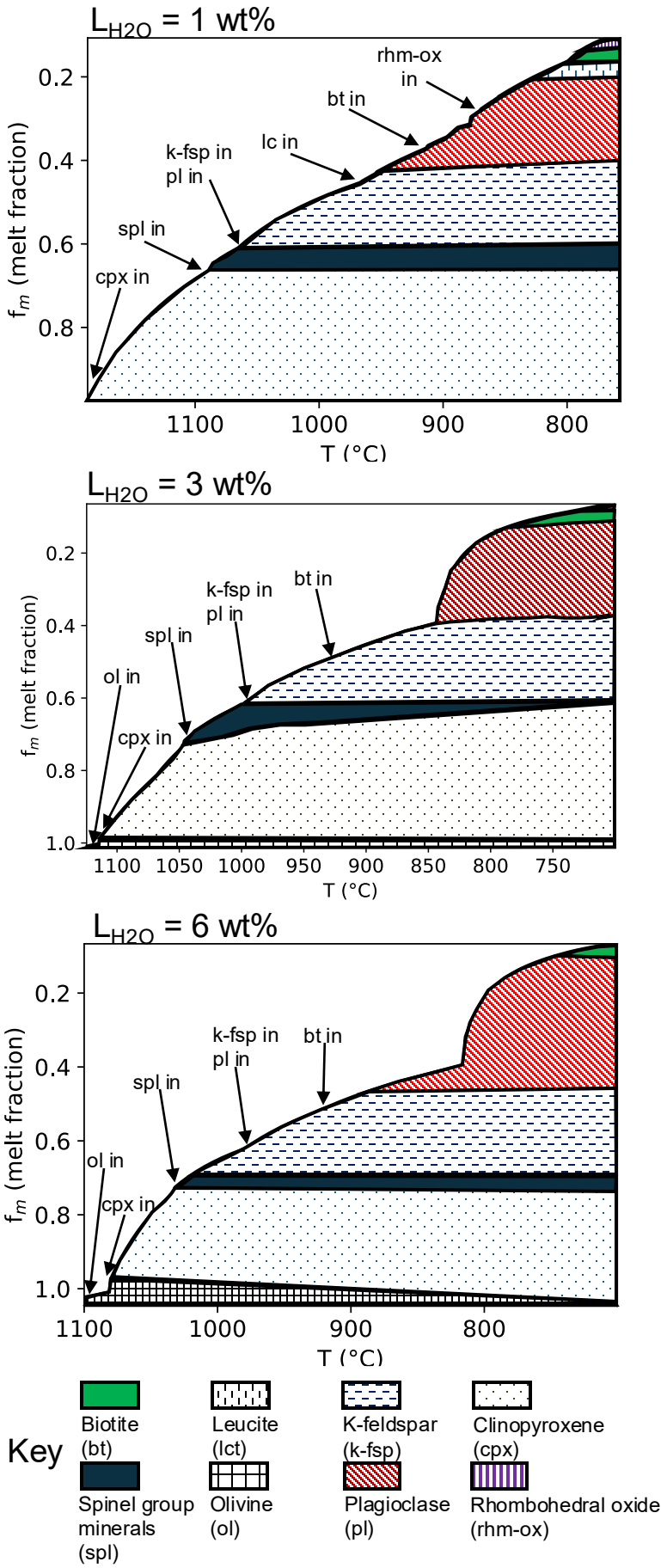

Supplementary Figure 6: Phase proportions as a function of magma temperature for fractional crystallisation Rhyolite-MELTS models at different initial L_{H2O}. Models are run at L_{fO2} = QFM and initial pressure = 140 MPa. Cpx, clinopyroxene; spl, spinel group minerals; k-fsp, alkali feldspar; pl, plagioclase feldspar; bt, biotite; lct, leucite; ms, muscovite; ol, olivine; nph, nepheline; rhm-ox, rhombohedral oxide.

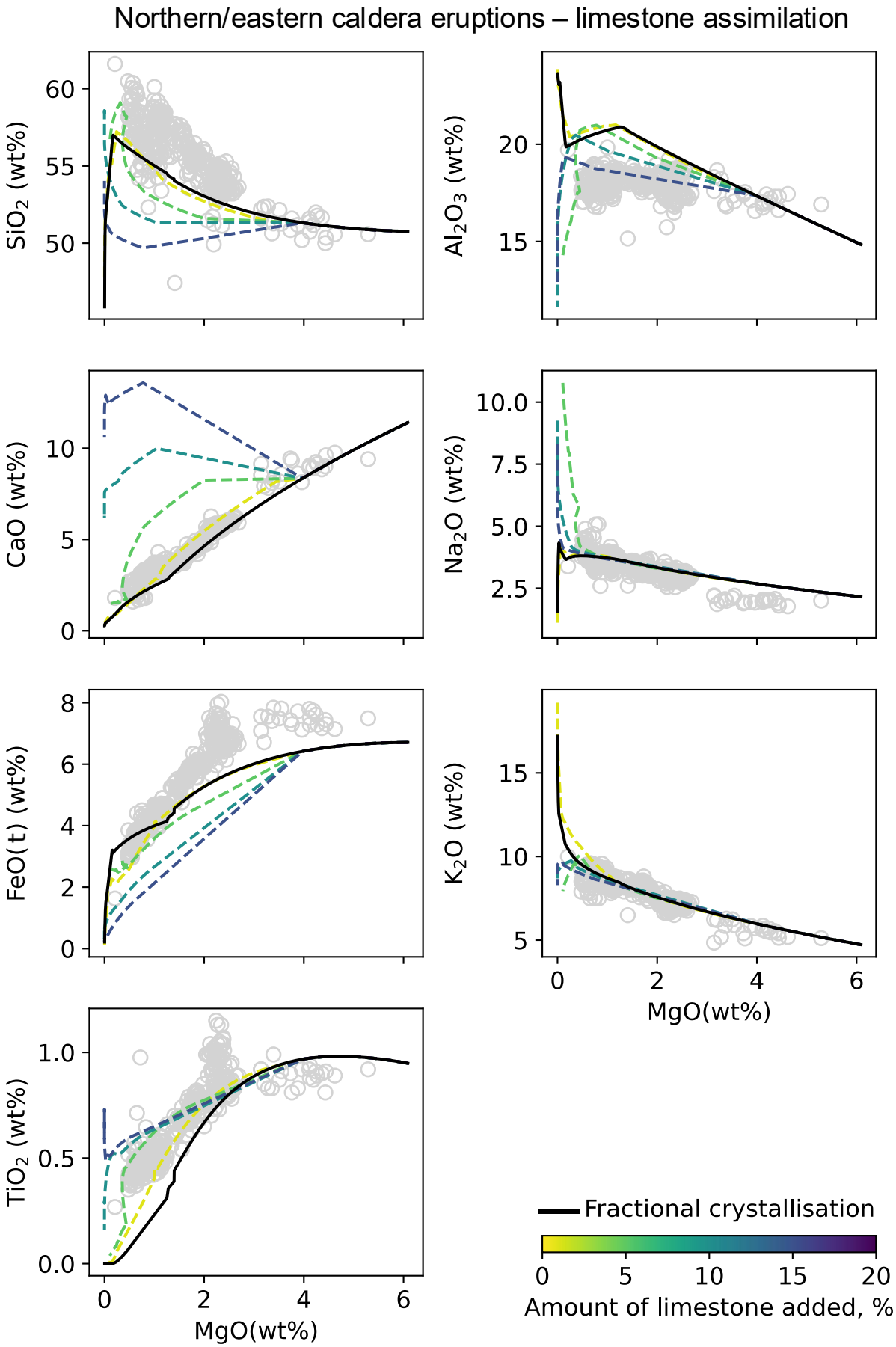

Supplementary Figure 7: Results of assimilation-fractional crystallisation models of limestone assimilation for northern/eastern caldera group eruptions. Grey circles show northern/eastern caldera group eruption glass data. Assimilant was added en masse at 1100°C. Each line represents a Rhyolite-MELTS model run at the best-fit fractional crystallisation conditions (L_{fO2}=QFM+1, L_{H2O} = 2 wt%, pressure=110 MPa) and addition of a specified amount of assimilant. The amount of assimilant added is indicated by the colour of the line from yellow to blue, with yellow indicating 1% assimilant added relative to 100% melt (equivalent to M_a/M_m=0.01 where Ma/Mm is the ratio of assimilant to melt) and dark blue indicating 20-30%. The black line shows the best-fit FC Rhyolite-MELTS model.

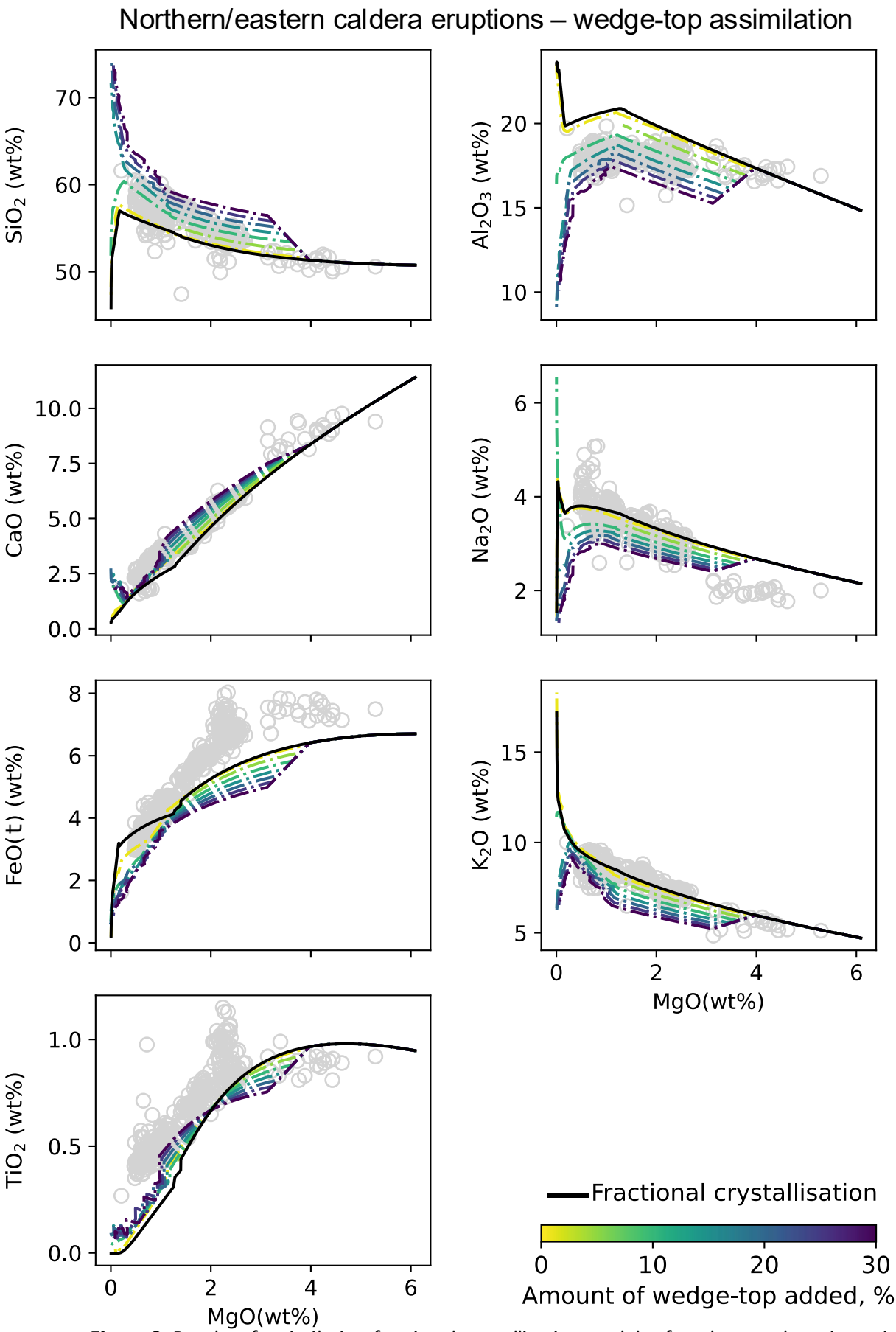

Supplementary Figure 8: Results of assimilation-fractional crystallisation models of wedge-top deposits assimilation for northern/eastern caldera group eruptions. Grey circles show northern/eastern caldera group eruption glass data. Assimilant was added en masse at 1100°C. Each line represents a Rhyolite-MELTS model run at the best-fit fractional crystallisation conditions (L_{fO2}=QFM+1, L_{H2O} = 2 wt%, pressure=110 MPa) and addition of a specified amount of assimilant. The amount of assimilant added is indicated by the colour of the line from yellow to blue, with yellow indicating 1% assimilant added relative to 100% melt (equivalent to M_a/M_m=0.01 where Ma/Mm is the ratio of assimilant to melt) and dark blue indicating 20-30%. The black line shows the best-fit FC Rhyolite-MELTS model.

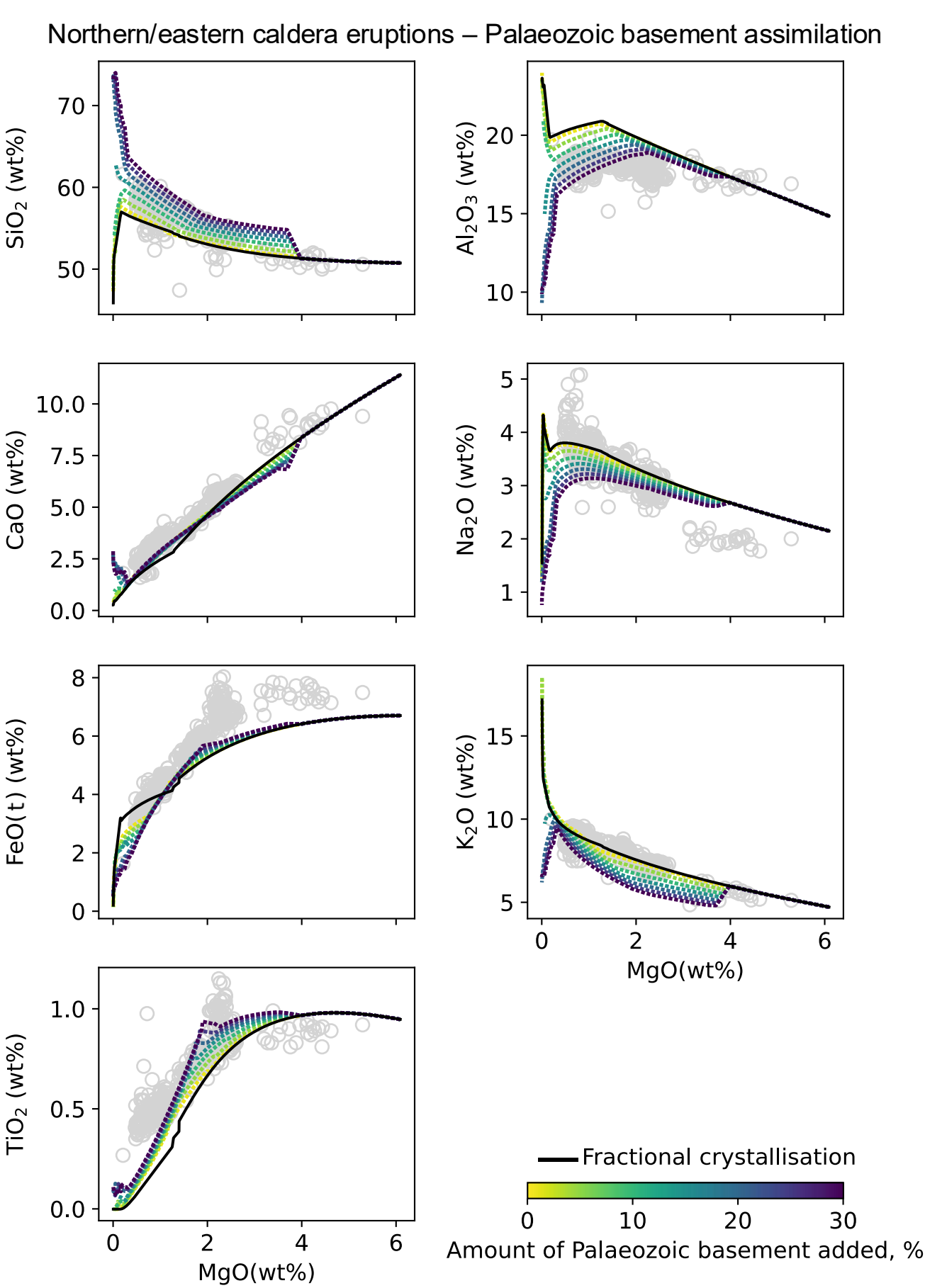

Supplementary Figure 9: Results of assimilation-fractional crystallisation models of Palaeozoic metamorphic basement assimilation for northern/eastern caldera group eruptions. Grey circles show northern/eastern caldera group eruption glass data. Assimilant was added en masse at 1100°C. Each line represents a Rhyolite-MELTS model run at the best-fit fractional crystallisation conditions (L_{fO2}=QFM+1, L_{H2O} = 2 wt%, pressure=110 MPa) and addition of a specified amount of assimilant. The amount of assimilant added is indicated by the colour of the line from yellow to blue, with yellow indicating 1% assimilant added relative to 100% melt (equivalent to M_a/M_m=0.01 where Ma/Mm is the ratio of assimilant to melt) and dark blue indicating 20-30%. The black line shows the best-fit FC Rhyolite-MELTS model.

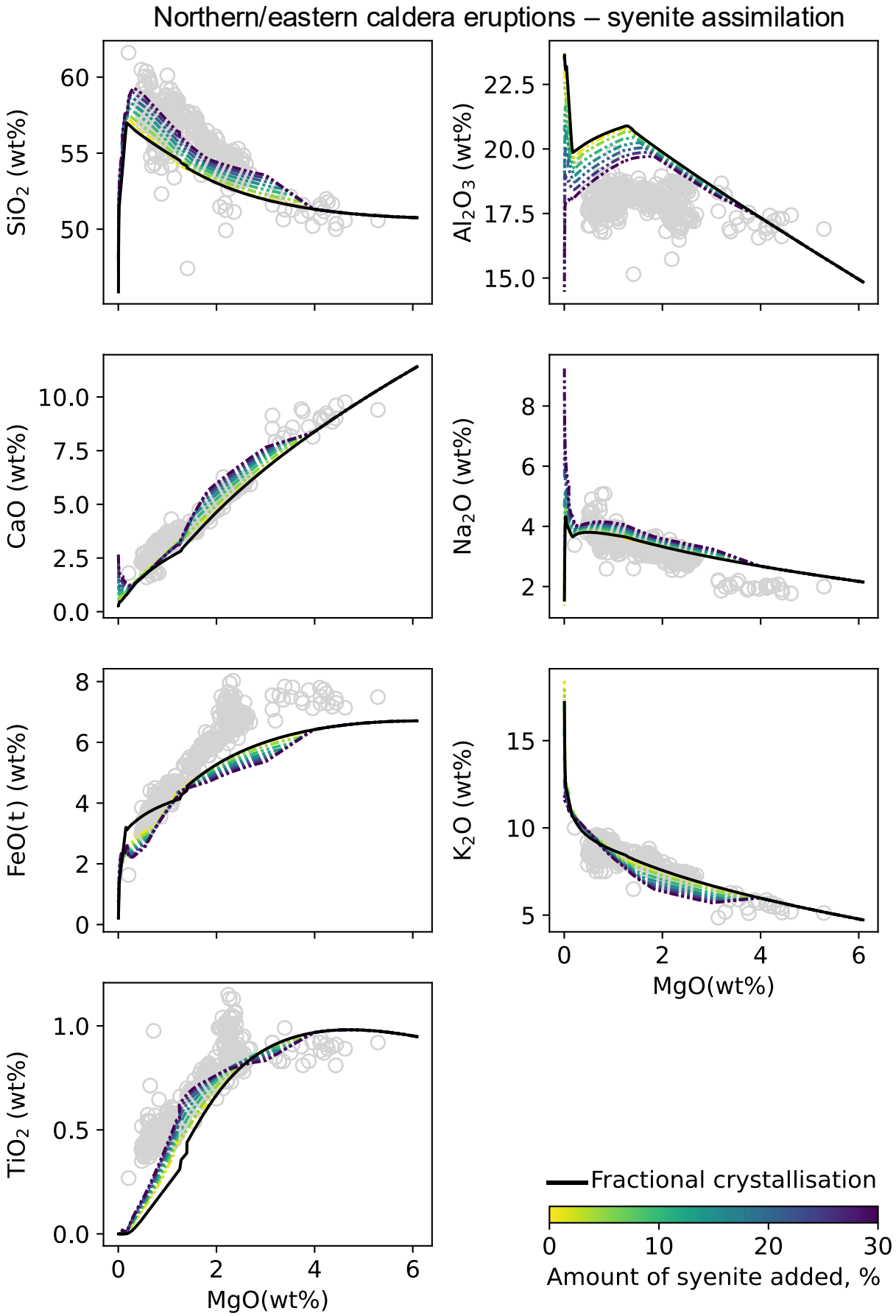

Supplementary Figure 10: Results of assimilation-fractional crystallisation models of syenite assimilation for northern/eastern caldera group eruptions. Grey circles show northern/eastern caldera group eruption glass data. Assimilant was added en masse at 1100°C. Each line represents a Rhyolite-MELTS model run at the best-fit fractional crystallisation conditions (L_{fO2}=QFM+1, L_{H2O} = 2 wt%, pressure=110 MPa) and addition of a specified amount of assimilant. The amount of assimilant added is indicated by the colour of the line from yellow to blue, with yellow indicating 1% assimilant added relative to 100% melt (equivalent to M_a/M_m=0.01 where Ma/Mm is the ratio of assimilant to melt) and dark blue indicating 20-30%. The black line shows the best-fit FC Rhyolite-MELTS model.

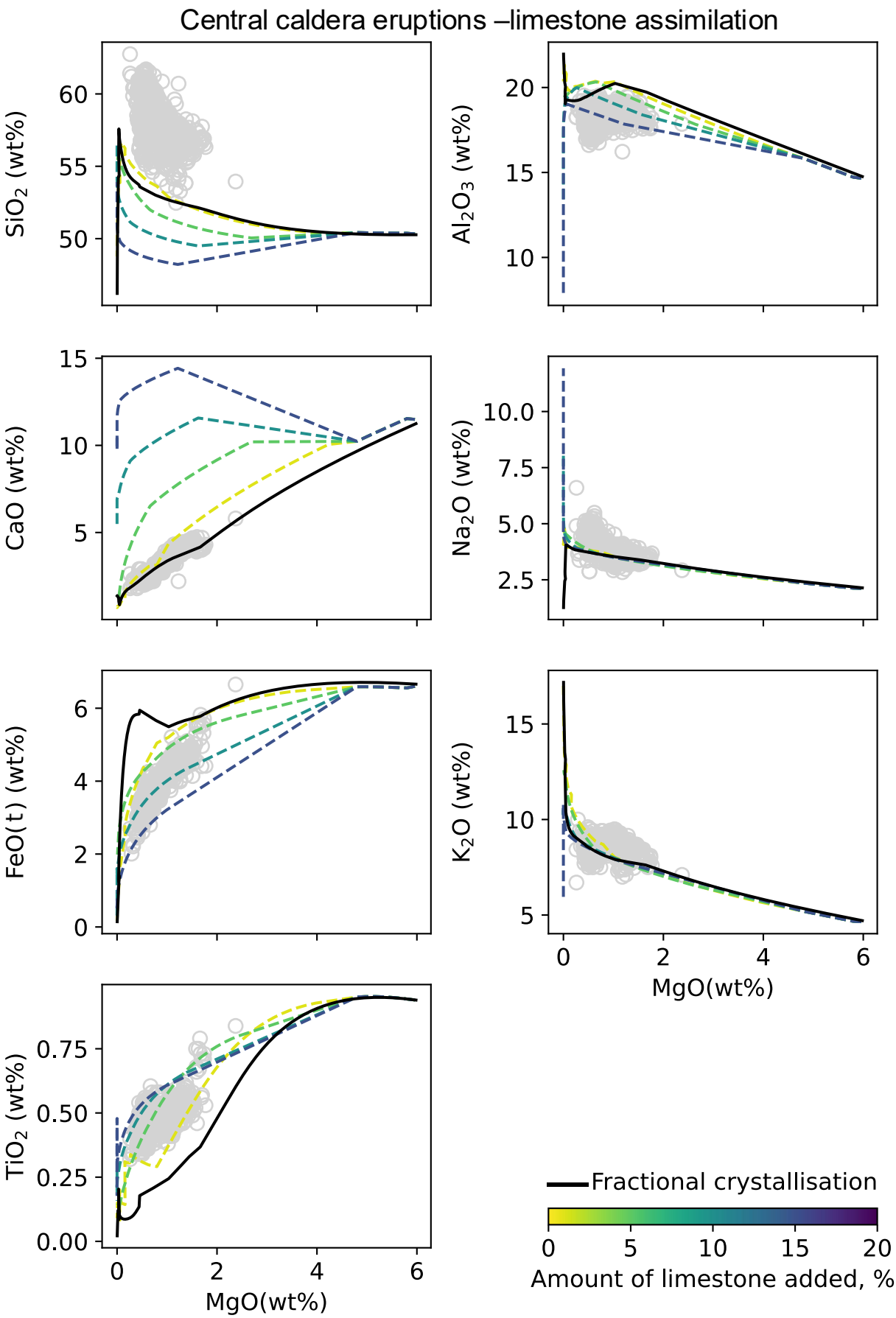

Supplementary Figure 11: Results of assimilation-fractional crystallisation models of limestone assimilation for central caldera group eruptions. Grey circles show central caldera group eruption glass data. Assimilant was addeden masse at 1100°C. Each line represents a Rhyolite-MELTS model run at the best-fit fractional crystallisation conditions (L_{fO2}=QFM, L_{H2O} = 3 wt%, pressure=140 MPa) and addition of a specified amount of assimilant. The amount of assimilant added is indicated by the colour of the line from yellow to blue, with yellow indicating 1% assimilant added relative to 100% melt (equivalent to M_a/M_m=0.01 where Ma/Mm is the ratio of assimilant to melt) and dark blue indicating 20-30%. The black line shows the best-fit FC Rhyolite-MELTS model.

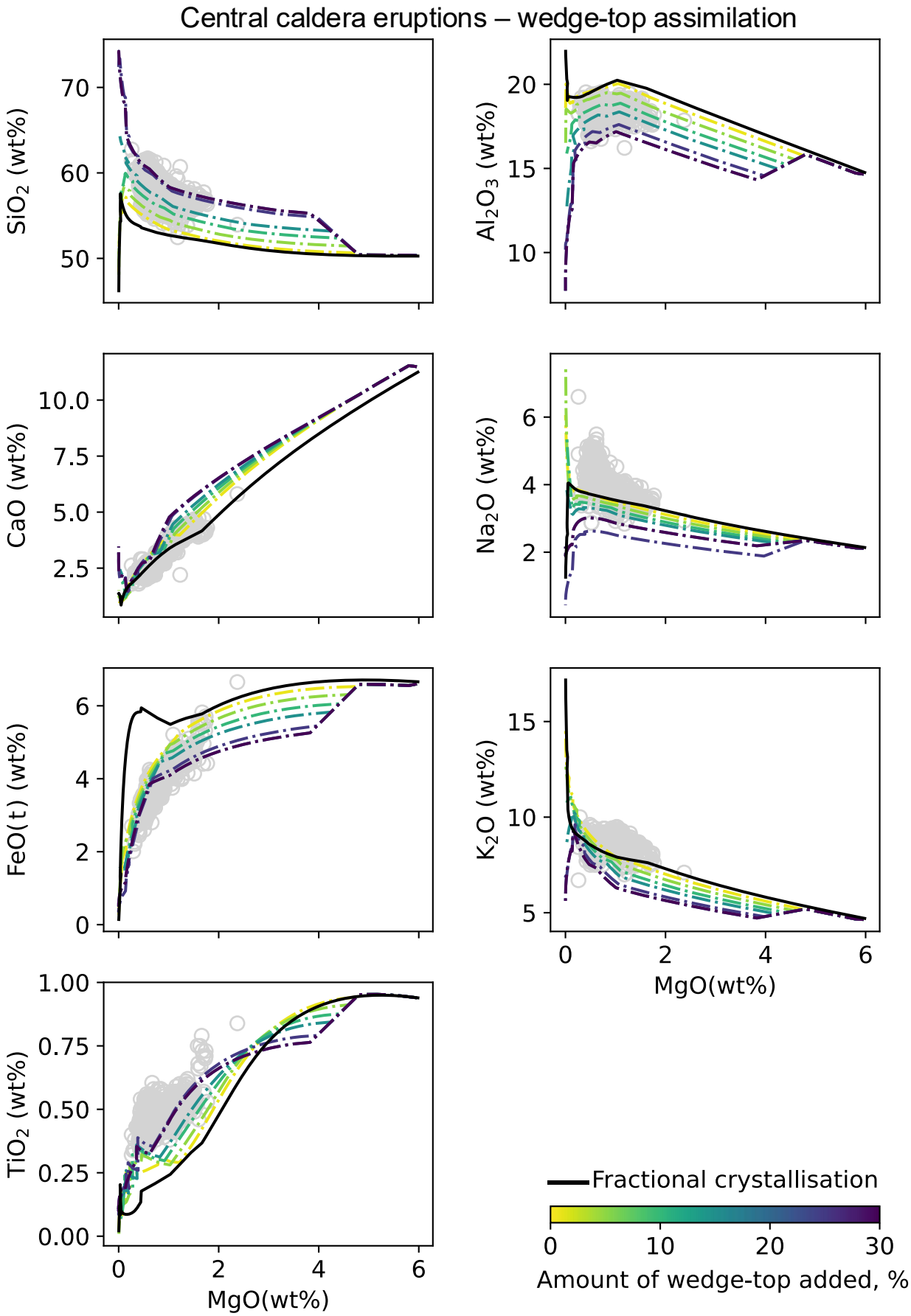

Supplementary Figure 12: Results of assimilation-fractional crystallisation models of wedge-top deposits assimilation for central caldera group eruptions. Grey circles show central caldera group eruption glass data. Assimilant was added en masse at 1100°C. Each line represents a Rhyolite-MELTS model run at the best-fit fractional crystallisation conditions (L_{fO2}=QFM, L_{H2O} = 3 wt%, pressure=140 MPa) and addition of a specified amount of assimilant. The amount of assimilant added is indicated by the colour of the line from yellow to blue, with yellow indicating 1% assimilant added relative to 100% melt (equivalent to M_a/M_m=0.01 where Ma/Mm is the ratio of assimilant to melt) and dark blue indicating 20-30%. The black line shows the best-fit FC Rhyolite-MELTS model.

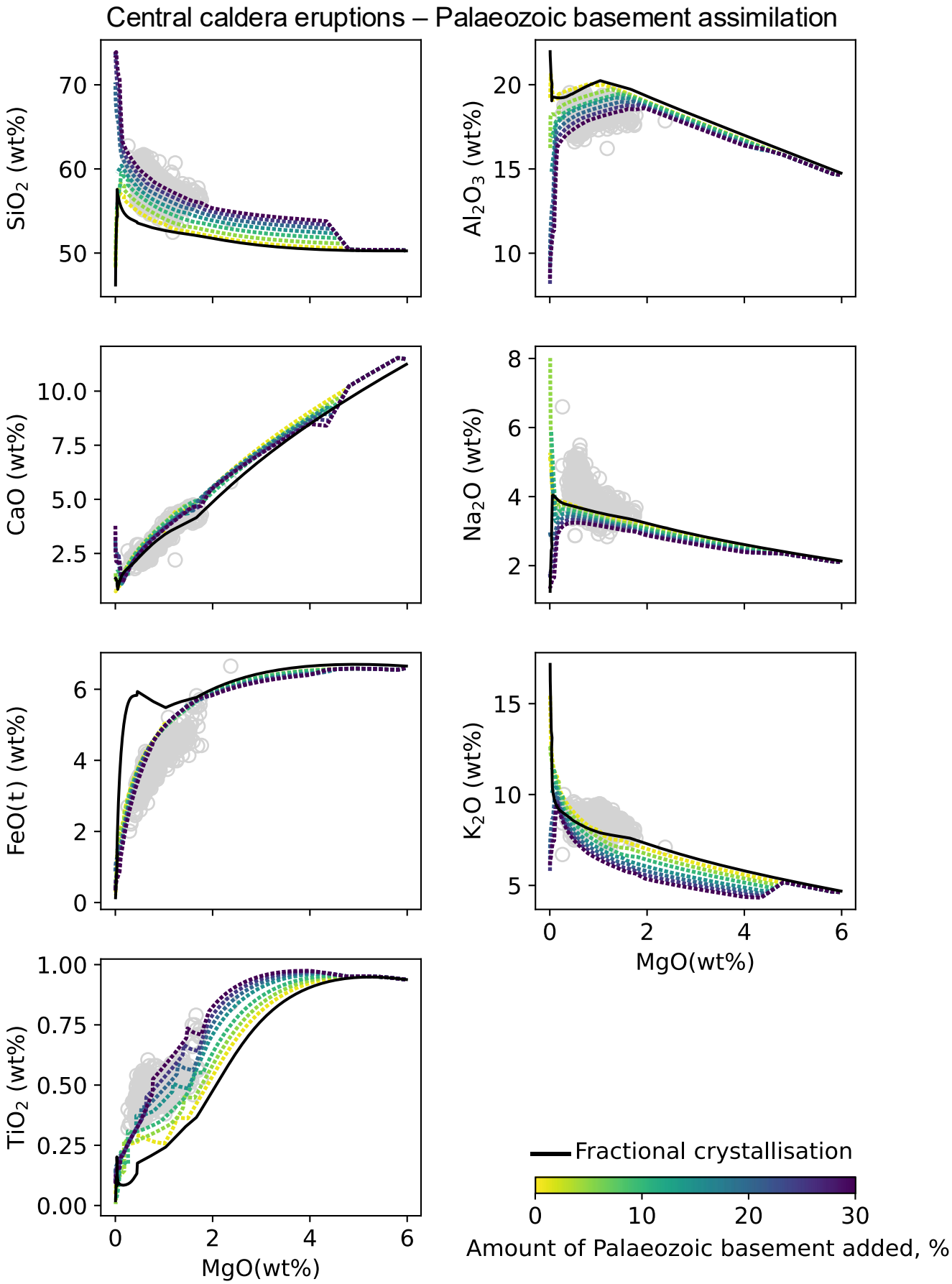

Supplementary Figure 13: Results of assimilation-fractional crystallisation models of Palaeozoic metamorphic basement assimilation for central caldera group eruptions. Grey circles show central caldera group eruption glass data. Assimilant was added en masse at 1100°C. Each line represents a Rhyolite-MELTS model run at the best-fit fractional crystallisation conditions (L_{fO2}=QFM, L_{H2O} = 3 wt%, pressure=140 MPa) and addition of a specified amount of assimilant. The amount of assimilant added is indicated by the colour of the line from yellow to blue, with yellow indicating 1% assimilant added relative to 100% melt (equivalent to M_a/M_m=0.01 where Ma/Mm is the ratio of assimilant to melt) and dark blue indicating 20-30%. The black line shows the best-fit FC Rhyolite-MELTS model.

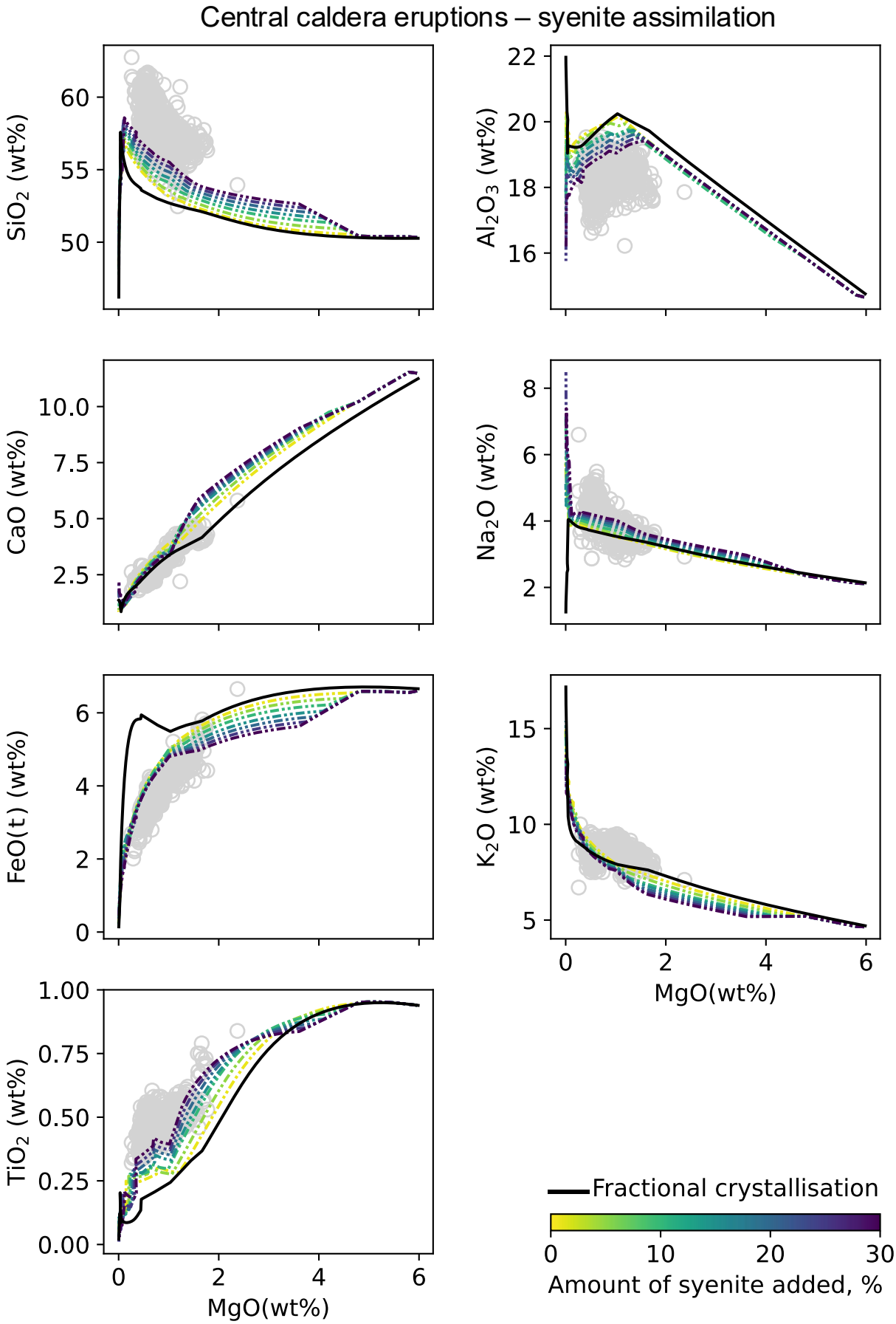

Supplementary Figure 14: Results of assimilation-fractional crystallisation models of syenite assimilation for central caldera group eruptions. Grey circles show central caldera group eruption glass data. Assimilant was added en masse at 1100°C. Each line represents a Rhyolite-MELTS model run at the best-fit fractional crystallisation conditions (L_{fO2}=QFM, L_{H2O} = 3 wt%, pressure=140 MPa) and addition of a specified amount of assimilant. The amount of assimilant added is indicated by the colour of the line from yellow to blue, with yellow indicating 1% assimilant added relative to 100% melt (equivalent to M_a/M_m=0.01 where Ma/Mm is the ratio of assimilant to melt) and dark blue indicating 20-30%. The black line shows the best-fit FC Rhyolite-MELTS model.

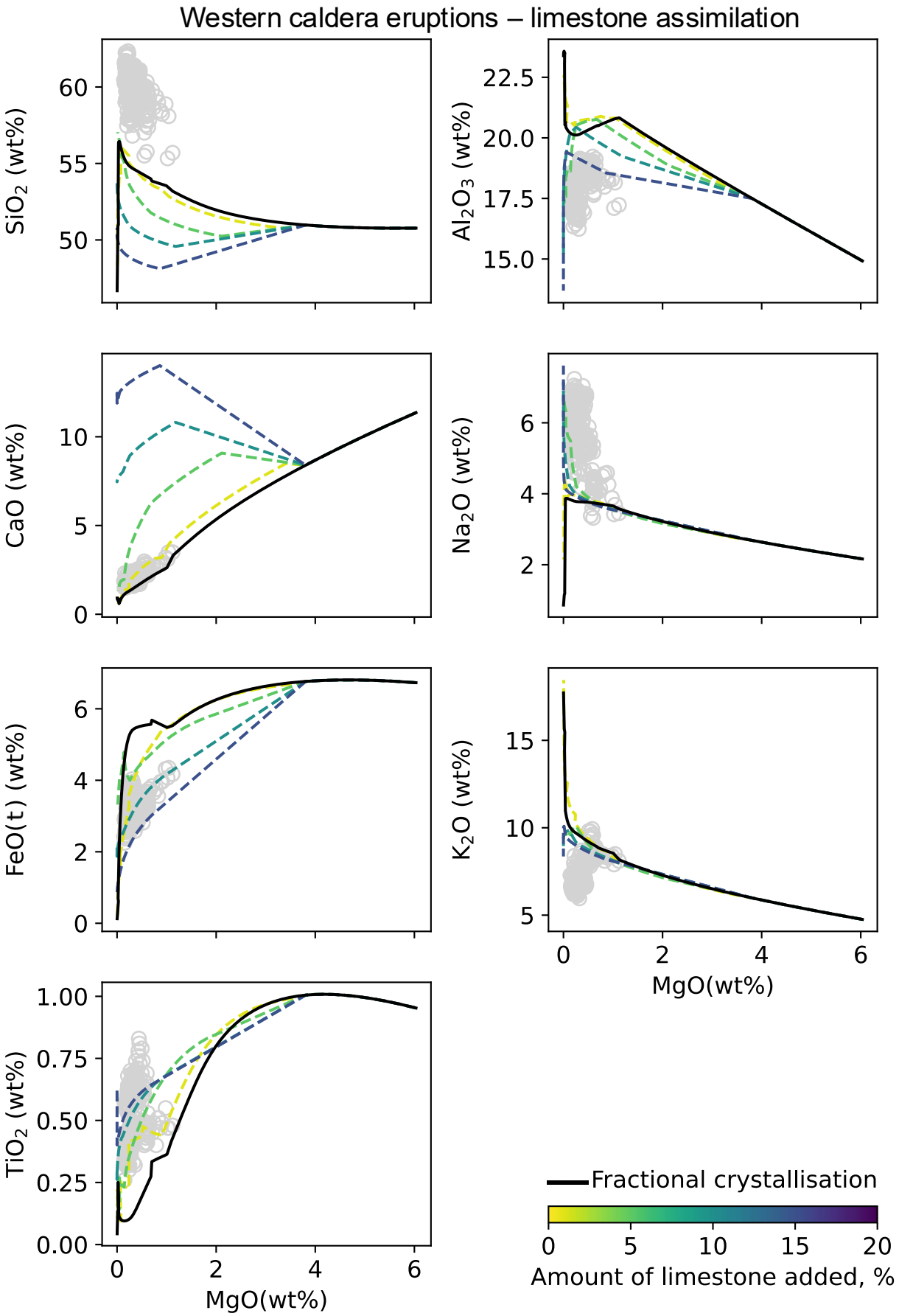

Supplementary Figure 15: Results of assimilation-fractional crystallisation models for limestone assimilation for western caldera group eruptions. Grey circles show western caldera eruption glass data. Assimilant was added en masse at 1100°C. Each line represents a Rhyolite-MELTS model run at the best-fit fractional crystallisation conditions (L_{fO2}=QFM, L_{H2O} = 2 wt%, pressure=160 MPa) and addition of a specified amount of assimilant. The amount of assimilant added is indicated by the colour of the line from yellow to blue, with yellow indicating 1% assimilant added relative to 100% melt (equivalent to M_a/M_m=0.01 where Ma/Mm is the ratio of assimilant to melt) and dark blue indicating 20-30%. The black line shows the best-fit FC Rhyolite-MELTS model.

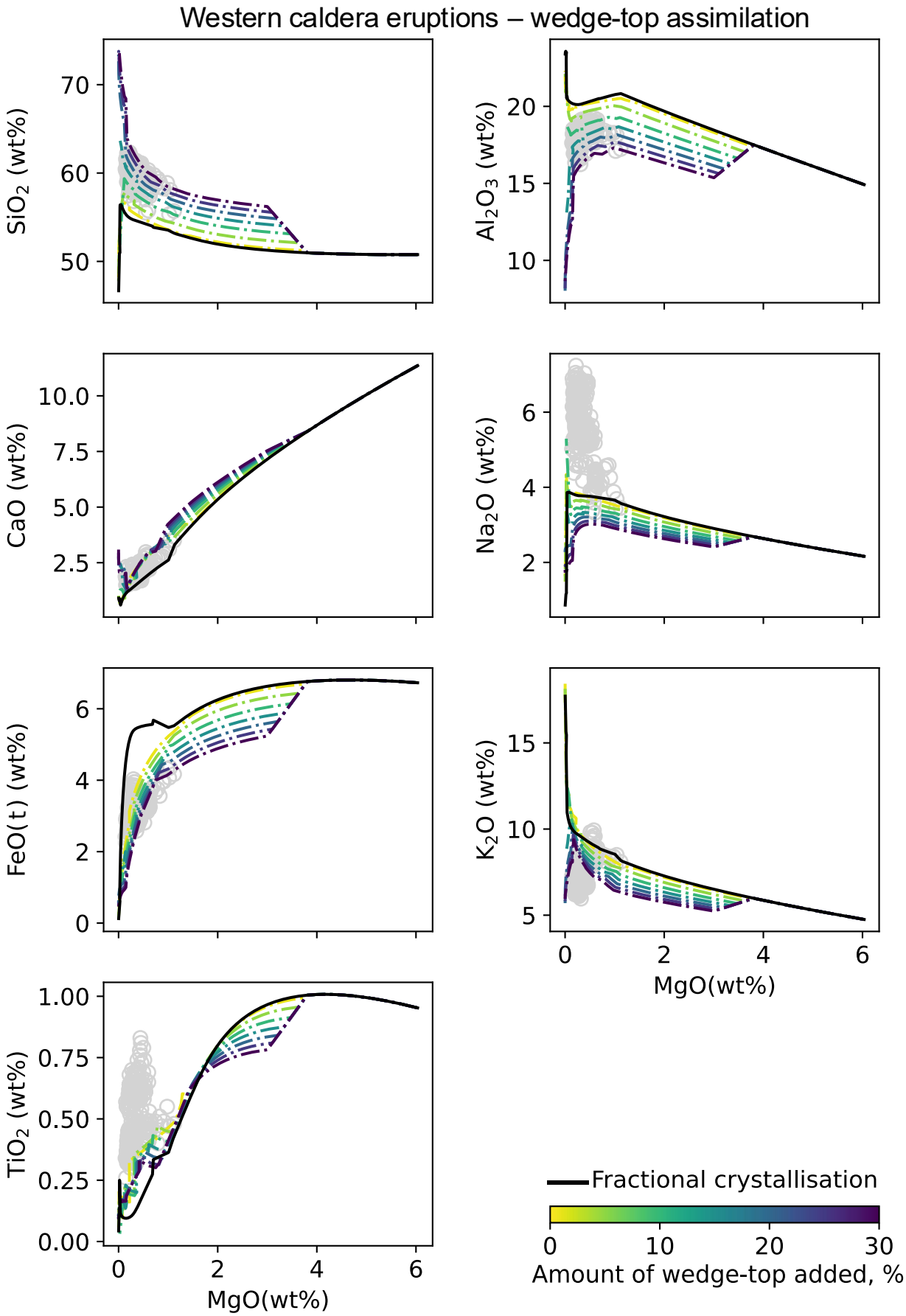

Supplementary Figure 16: Results of assimilation-fractional crystallisation models for wedge-top deposits assimilation for western caldera group eruptions. Grey circles show western caldera eruption glass data. Assimilant was addeden masse at 1100°C. Each line represents a Rhyolite-MELTS model run at the best-fit fractional crystallisation conditions (L_{fO2}=QFM, L_{H2O} = 2 wt%, pressure=160 MPa) and addition of a specified amount of assimilant. The amount of assimilant added is indicated by the colour of the line from yellow to blue, with yellow indicating 1% assimilant added relative to 100% melt (equivalent to M_a/M_m=0.01 where Ma/Mm is the ratio of assimilant to melt) and dark blue indicating 20-30%. The black line shows the best-fit FC Rhyolite-MELTS model.

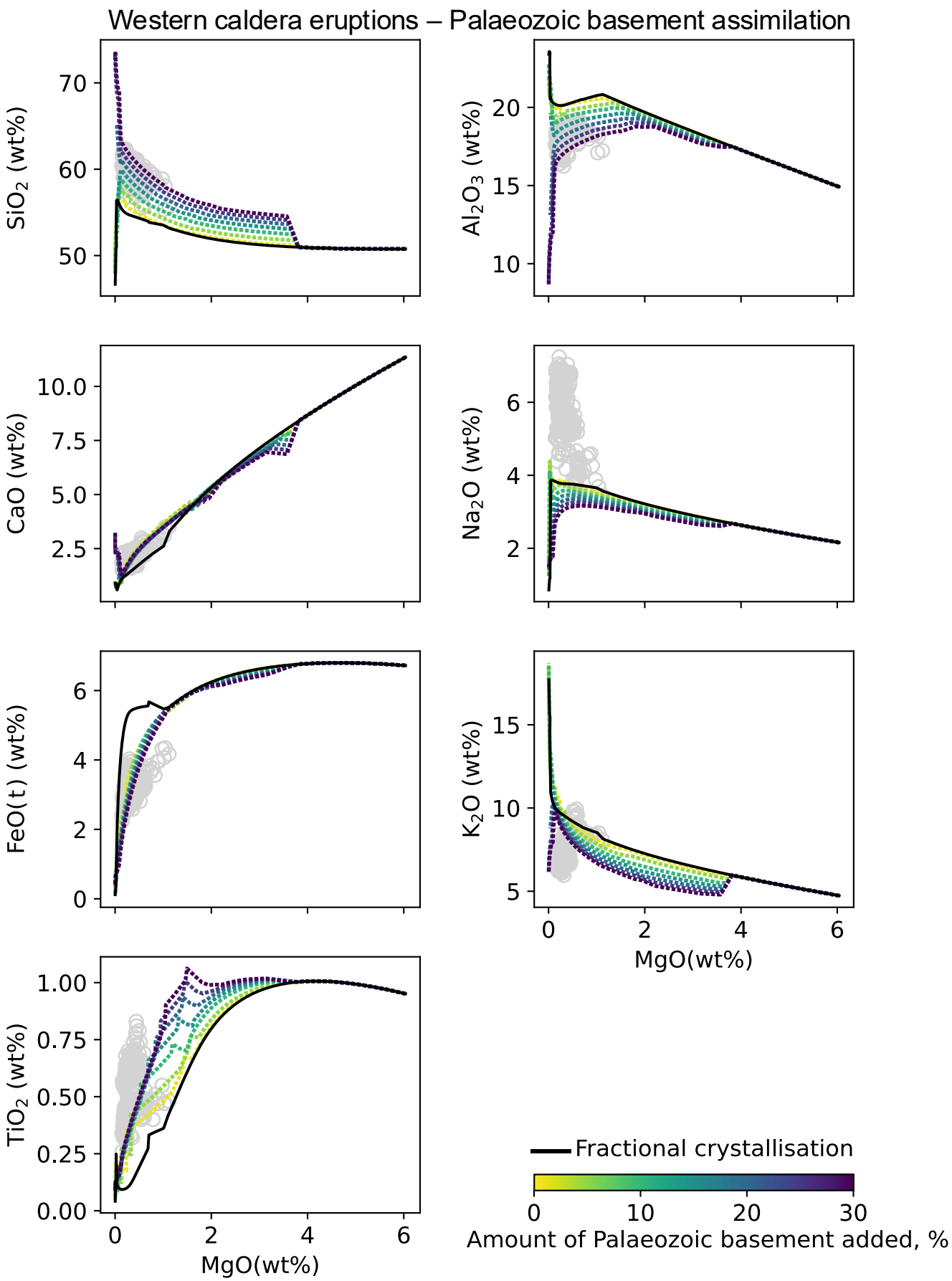

Supplementary Figure 17: Results of assimilation-fractional crystallisation models for Palaeozoic metamorphic basement assimilation for western caldera group eruptions. Grey circles show western caldera eruption glass data. Assimilant was added en masse at 1100°C. Each line represents a Rhyolite-MELTS model run at the best-fit fractional crystallisation conditions (L_{fO2}=QFM, L_{H2O} = 2 wt%, pressure=160 MPa) and addition of a specified amount of assimilant. The amount of assimilant added is indicated by the colour of the line from yellow to blue, with yellow indicating 1% assimilant added relative to 100% melt (equivalent to M_a/M_m=0.01 where Ma/Mm is the ratio of assimilant to melt) and dark blue indicating 20-30%. The black line shows the best-fit FC Rhyolite-MELTS model.

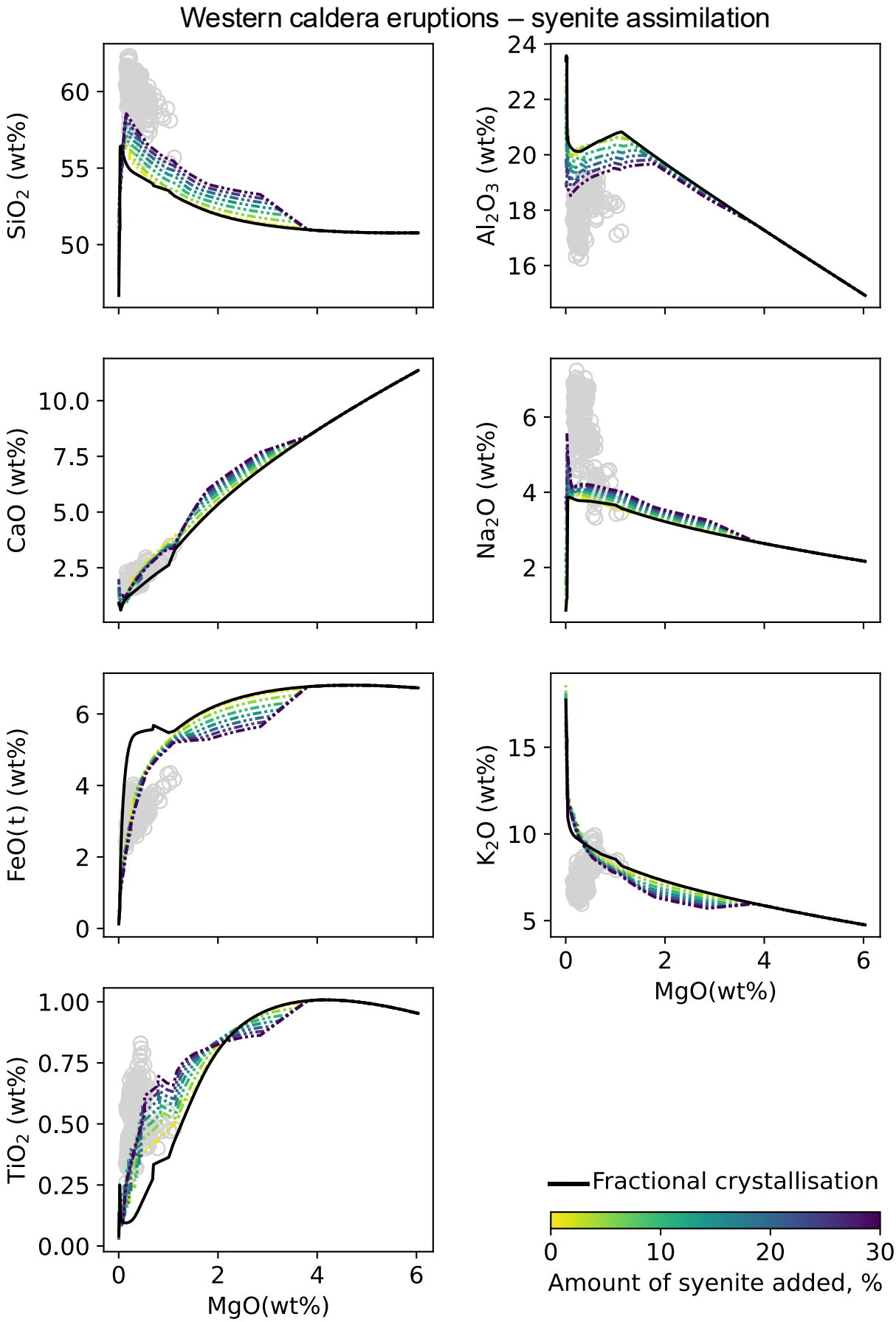

Supplementary Figure 18: Results of assimilation-fractional crystallisation models for syenite assimilation for western caldera group eruptions. Grey circles show western caldera eruption glass data. Assimilant was added en masse at 1100°C. Each line represents a Rhyolite-MELTS model run at the best-fit fractional crystallisation conditions (L_{fO2}=QFM, L_{H2O} = 2 wt%, pressure=160 MPa) and addition of a specified amount of assimilant. The amount of assimilant added is indicated by the colour of the line from yellow to blue, with yellow indicating 1% assimilant added relative to 100% melt (equivalent to M_a/M_m=0.01 where Ma/Mm is the ratio of assimilant to melt) and dark blue indicating 20-30%. The black line shows the best-fit FC Rhyolite-MELTS model.

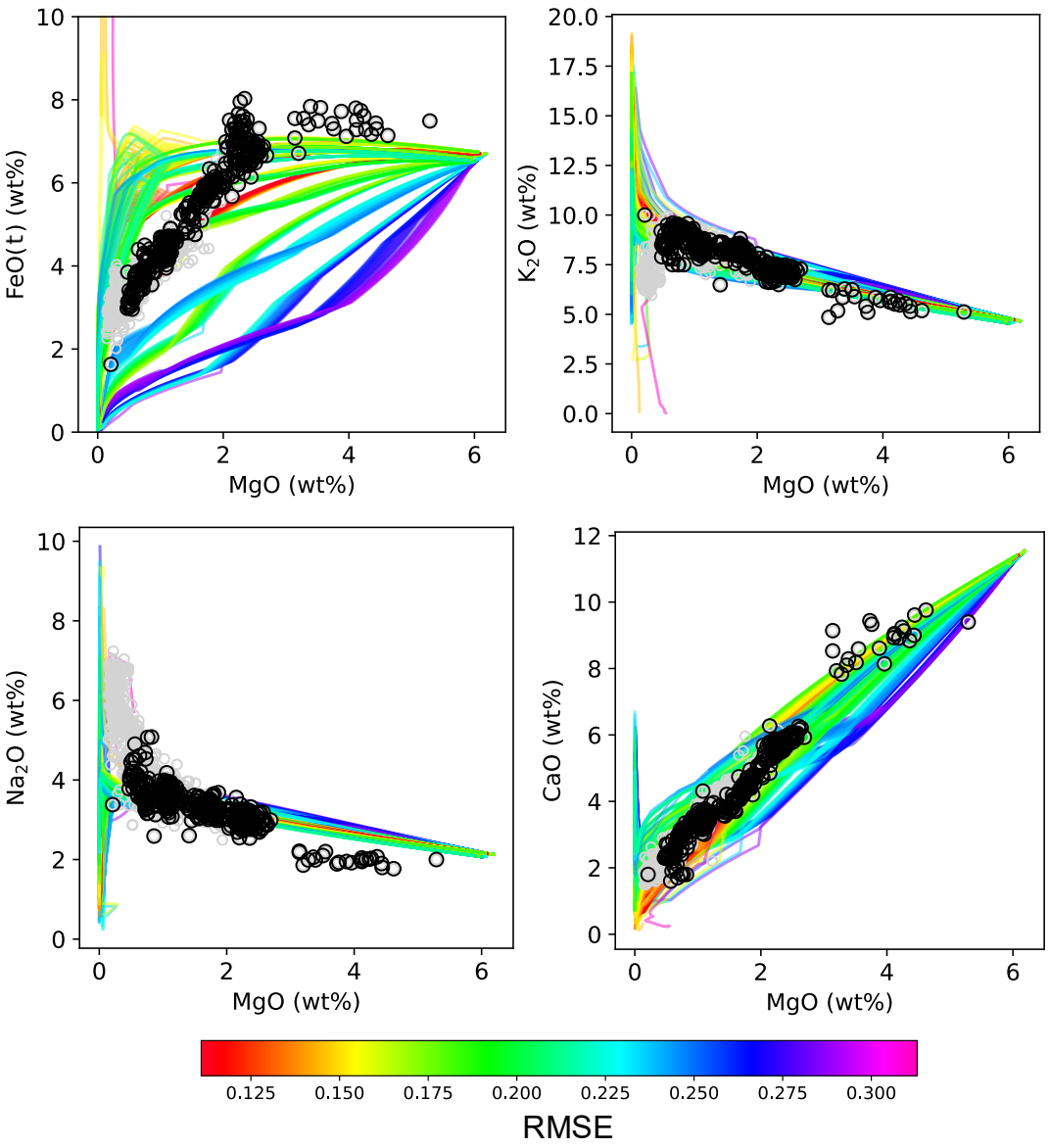

Supplementary Figure 19: Results of all Rhyolite-MELTS models of fractional crystallisation for northern/eastern caldera eruptions. Grey points represent all literature glass data for eruptions in the last 15 kyr, black points are literature glass data for the eastern caldera group eruptions. Each line represents the liquid line of descent predicted by Rhyolite-MELTS for a parental magma cooling and crystallising under a given pressure, L_{H2O} and L_{fO2}. Each model is coloured according to the RMSE value indicating the goodness-of-fit between the model and natural data; red indicates a better fit, blue/purple indicates a worse fit.

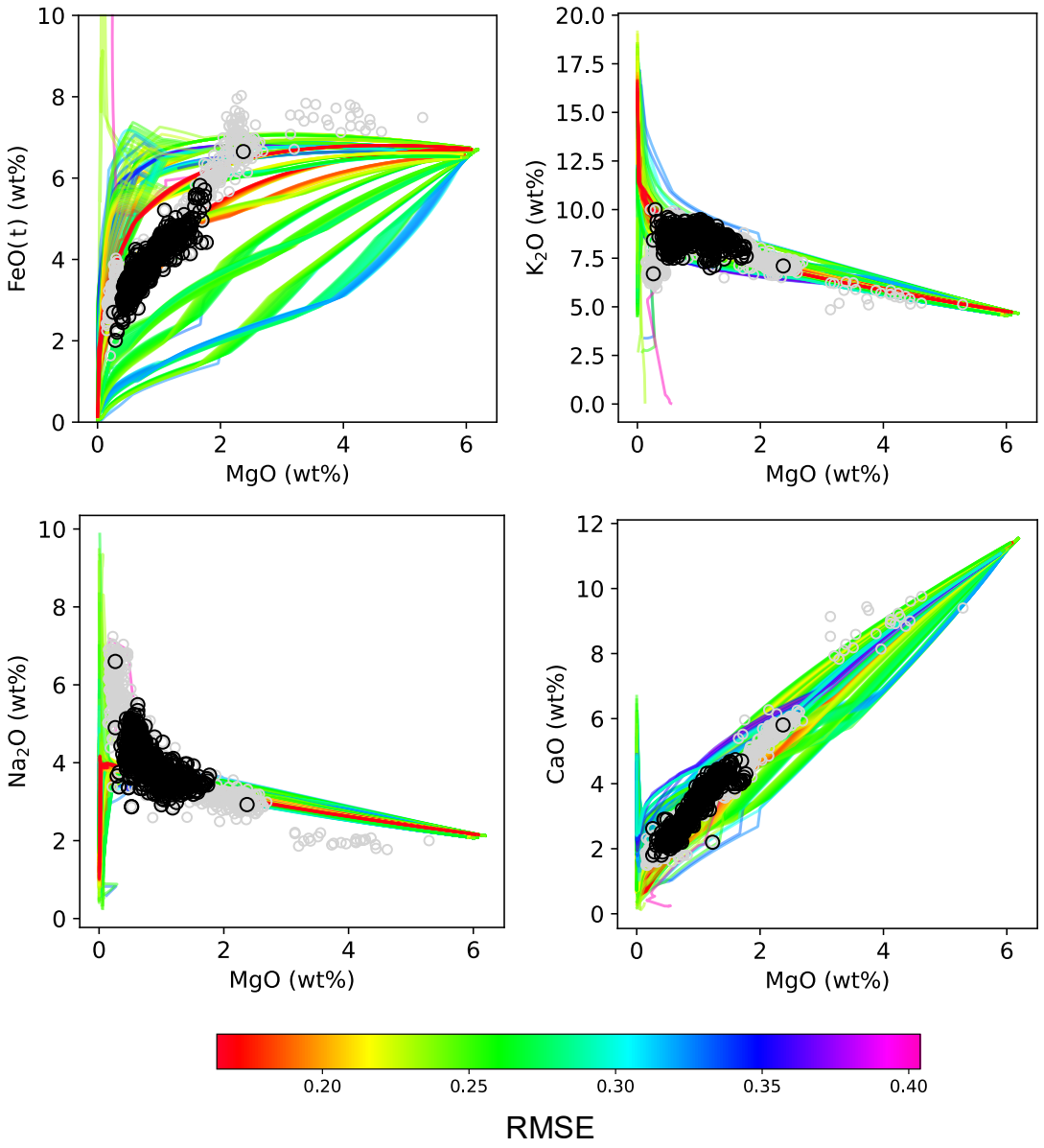

Supplementary Figure 20: Results of all Rhyolite-MELTS models of fractional crystallisation for central caldera eruptions. Grey points represent all literature glass data for eruptions in the last 15 kyr, black points are literature glass data for the central caldera group eruptions. Each line represents the liquid line of descent predicted by Rhyolite-MELTS for a parental magma cooling and crystallising under a given pressure, L_{H2O} and L_{fO2}. Each model is coloured according to the RMSE value indicating the goodness-of-fit between the model and natural data; red indicates a better fit, blue/purple indicates a worse fit.

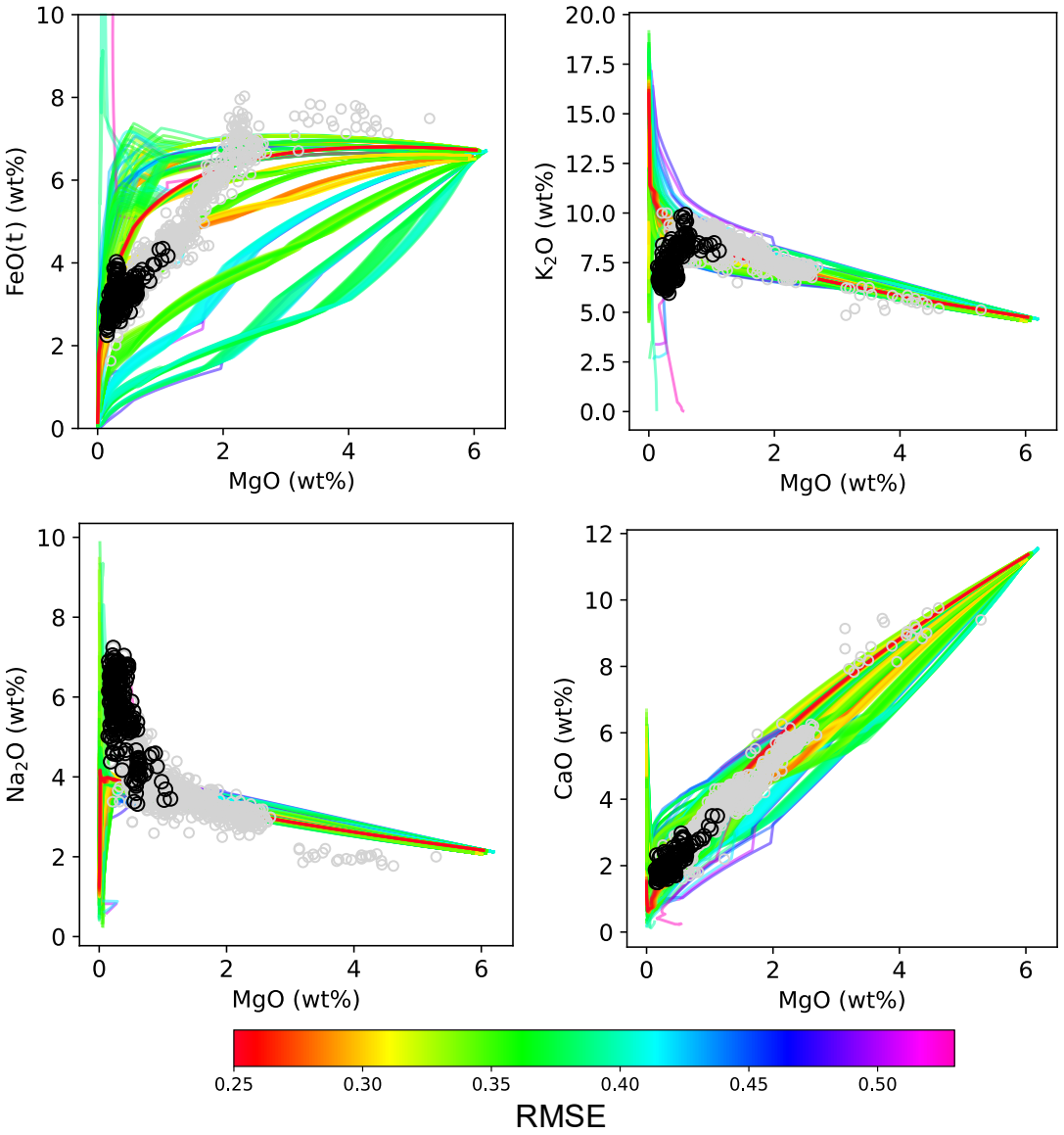

Supplementary Figure 21: Results of all Rhyolite-MELTS models of fractional crystallisation for western caldera eruptions. Grey points represent all literature glass data for eruptions in the last 15 kyr, black points are literature glass data for the western caldera group eruptions. Each line represents the liquid line of descent predicted by Rhyolite-MELTS for a parental magma cooling and crystallising under a given pressure, L_{H2O} and L_{fO2}. Each model is coloured according to the RMSE value indicating the goodness-of-fit between the model and natural data; red indicates a better fit, blue/purple indicates a worse fit.

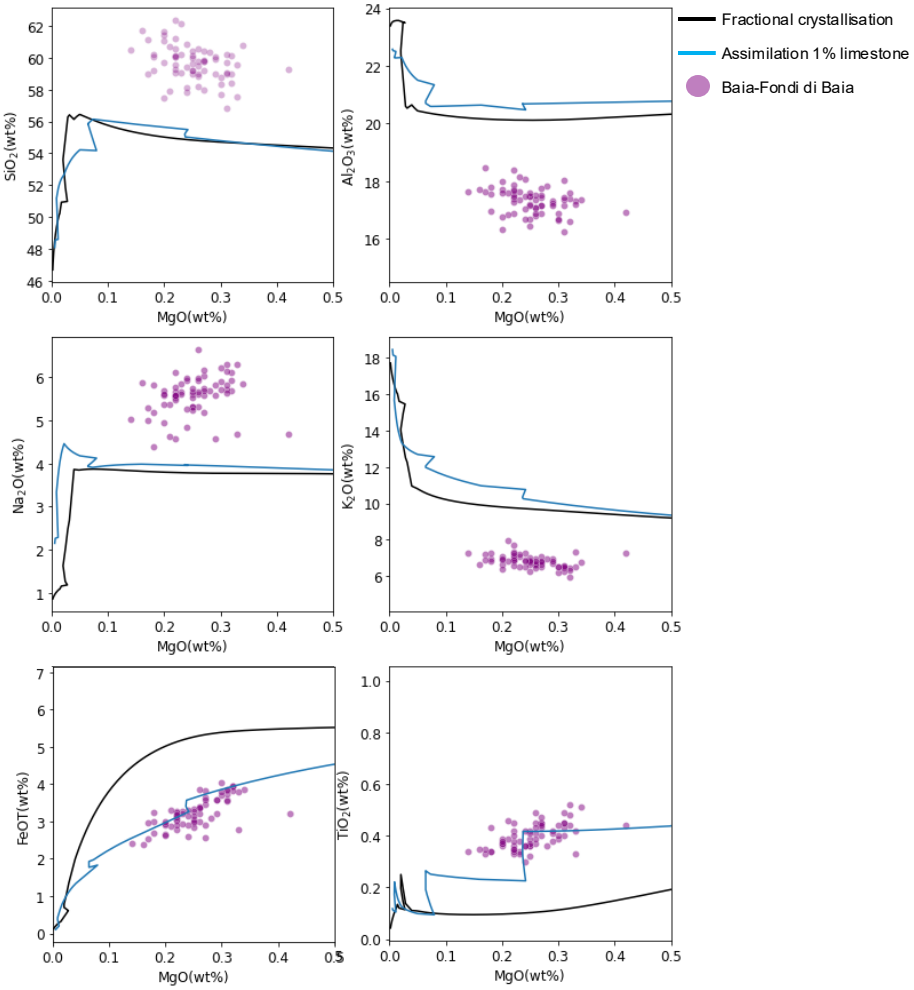

Supplementary Figure 22: : Results of assimilation-fractional crystallisation models for limestone assimilation for Baia-Fondi di Baia eruption. Purple circles show Baia-Fondi di Baia eruption glass data. Assimilant was added en masse at 1100°C. The blue line represents a Rhyolite-MELTS model run at the best-fit fractional crystallisation conditions (L_{fO2}=QFM, L_{H2O} = 2 wt%, pressure=160 MPa) and addition of 1% of limestone relative to 100% melt. The black line shows the best-fit FC Rhyolite-MELTS model.